# Synchrotron X-ray Diffraction Studies on Oxide Surfaces and Interfaces

by

Yongsoo Yang

A dissertation submitted in partial fulfillment
of the requirements for the degree of
Doctor of Philosophy
(Physics)
in The University of Michigan
2014

Doctoral Committee:

Professor Roy Clarke, Chair
Professor Çagliyan Kurdak
Christian M. Schlepütz, Argonne National Laboratory
Associate Professor Max Shtein
Professor Ctirad Uher

To my family

# ACKNOWLEDGEMENTS

Firstly, I would like to thank my family: my parents, Yongjoon, and Yongjae. Their love, trust, and consistent emotional support throughout the entire course of my study served as a solid foundation on which I could solely concentrate on building up my skills and knowledge in physics. I also appreciate Annette for her enormous material and spiritual support.

My deepest thanks surely go to my advisor, Professor Roy Clarke. His scientific knowledge and insight always have guided me to the right directions, and he has strongly encouraged any research plans and ideas I came up with, providing firm support for every project I have participated in. Especially, whenever we encountered challenging situations during research, he has willingly and enthusiastically approached the issues. His passion helped me successfully overcome any hardships I faced, and I hope to follow his passion in the future.

I am especially indebted to Dr. Christian Schlepütz at Argonne National Laboratory for his strong support and help. He started guiding me as a Post-Doc when I just started my graduate study, and he has continuously supported me as a beamline scientist at the synchrotron. He provided tremendous help as a dissertation committee member even during the final stages of my study. Almost all of my technical skills and knowledge in crystallography and x-ray diffraction came from his friendly guidance. He generously provided all the data analysis tools he developed, and I also appreciate his personal friendship; all the beamtimes and conferences with him have been very fun and successful.

Collaborations with Professor Max Shtein and his group members, Dr. Shaurjo Biswas and Olga Shalev, have been a very enjoyable experience. I have been able to obtain invaluable new knowledge, skills and experiences during this collaboration. I also appreciate Professor Shtein for all the guidance he provided as a dissertation committee member.

I also thank Professor Çaglian Kurdak and Professor Ctirad Uher for their insight and suggestions for this dissertation.

There are many collaborators who kindly provided all the samples for this study.

Professor Steven Durbin at Western Michigan University and Dr. Martin Allen at University of Canterbury and their group members, Dr. Robert Heinhold and Dr. David Kim, provided very high quality ZnO wafers and Schottky contacts. Dr. Carolina Adamo and Professor Darrell Schlom at Cornell University provided the excellent $BiFeO_3$ films on $SrTiO_3$ substrates, and Dr. Christianne Beekman, Dr. Wolter Siemons and Dr. Hans Christen at Oak Ridge National Laboratory prepared the $BiFeO_3$ films on $LaAlO_3$ substrates in great quality. I would like to thank all of them for their efforts in preparing high-quality samples, and also for all the other collaborative works, which has always been very pleasant.

I appreciate excellent support from the beamline staff at the synchrotrons I visited: Dr. Peter Eng and Dr. Joanne Stubbs (APS 13-BM-C, 13-ID-C), Dr. Christian Schlepütz, Dr. Zhan Zhang, Evguenia Karapetrova (APS 33-BM-C, 33-ID-D), and Dr. Philip Willmott (SLS X04SA). All the data presented in this dissertation were obtained through their superb support.

There have been many other collaborations besides those mentioned in my dissertation, and I would like to thank Professor Yizhak Yacoby and Professor Yossi Paltiel at Hebrew University of Jerusalem, Professor Randall Headrick and Dr. Ishviene Cour at University of Vermont, Dr. Ron Pindak and Dr. Christie Nelson at the National Synchrotron Light Source, and Nathaniel Feldberg at University at Buffalo. It has been my pleasure to collaborate with all these nice people, and I look forward to continuing collaborations.

I also appreciate Professor Kee Hoon Kim, my undergraduate thesis advisor. His enthusiasm and insights in experimental research provided a strong motivation for me to continue my graduate studies in condensed matter experiments.

Thanks to Dr. Naji Husseini and Dr. Vladimir Stoica, with whom I had several successful beamtimes and helpful discussions, and Nancy Senabulya, who will continue working on this synchrotron studies, and all other current and former officemates and Clarke group members: Abe Oraiqat, Yuwei Li, James Mathis, Christina Jones, Renee Harton, and Dr. Codrin Cionca.

I also thank my U-M physics colleagues, Jieun Lee, Dr. Sunghoon Jung, Yun Suk Eo, and Mijin Yoon, for many helpful discussions and fun outings, and our afternoon coffee members, including Dennis Allen and Ramon Torres-Isea, for refreshing coffee breaks, and other friends I met in Michigan: my former roommate Dr. Beom-Chan Lee, Soojeong Kim, Janghyun Lee, Dr. Young-Jae Shin, and many others, especially those from the Ann Arbor catholic student group and St. Andrew Kim catholic church.

I should mention Junhyun Lee, my old physics friend, who is also staying in the condensed matter field. I appreciate his pleasant friendship as well as many helpful physics discussions and motivations from him.

I also thank all other relatives, friends, and colleagues. Although I could not acknowledge all of them here, it would not have been possible for me to finish my thesis without their relations and influences.

I thank Dr. Matts Björck for supporting GenX and making it freely available.

All the works presented here were supported by the U.S. Department of Energy (contract no. DE-FG02-06ER46273, PI: Roy Clarke). The experiments were performed in part at the X04SA beamline at the Swiss Light Source, Paul Scherrer Institut, Villigen, Switzerland, and at Sector 13-BM-C, 13-ID-C (GeoSoilEnviroCARS) and Sector 33-BM-C, 33-ID-D at the Advanced Photon Source (APS). GeoSoilEnviroCARS is supported by the National Science Foundation - Earth Sciences (EAR-0622171) and the Department of Energy - Geosciences (DE-FG02-94ER14466). The use of the APS was supported by the U.S. Department of Energy, Office of Science, Office of Basic Energy Sciences, under contract no. DE-AC02-06CH11357.

# TABLE OF CONTENTS

# LIST OF FIGURES

**Figure**

# LIST OF TABLES

**Table**

# LIST OF APPENDICES

**Appendix**

# LIST OF ABBREVIATIONS

**AFM** atomic force microscopy

**BM** bending magnet

**CTR** crystal truncation rod

**DFT** density functional theory

**DL** double layer

**EPLD** eclipse pulsed laser deposition

**FOM** figure of merit

**FWHM** full width at half maximum

**ID** insertion device

**ML** monolayer

**RF** radio frequency

**r. l. u.** reciprocal lattice units

**ROI** region of interest

**RSM** reciprocal space map

**RT** room temperature

**SXRD** surface x-ray diffraction

**TMO** transition metal oxide

**UC** unit cell

**UHV** ultra-high vacuum

**XPS** x-ray photoemission spectroscopy

# ABSTRACT

Surfaces and interfaces of oxide crystals have gained a burst of attention in recent years due to their importance in technological applications as well as fundamental interest in their exotic behavior. Zinc oxide (ZnO) is one of the oxide materials which has been intensively studied especially for its transport behavior at the Schottky interface, which leads to many electronic device applications. Bismuth ferrite ($BiFeO_3$) is a unique material that exhibits stable magnetoelectric multiferroicity at room temperature, yielding new paradigms in the design of novel electromagnetic devices. Both the Schottky property of ZnO and the multiferroic behavior of $BiFeO_3$ depend critically on the atomic structure of their surfaces and interfaces. Therefore, the accurate determination of their structure is a prerequisite for controlling and optimizing their properties for applications.

The atomic surface and interface structures of uncoated and metal-coated ZnO (0001) Zn-polar and $(000\overline{1})$ O-polar wafers are measured with surface x-ray diffraction. All Zn-polar surfaces and Schottky interfaces show the presence of a fully occupied $(1\times1)$ overlayer of oxygen atoms on top of the terminating Zn layer, and no significant atomic relaxations are observed. O-polar surfaces are significantly rougher than Zn-polar surfaces, exhibiting Gaussian-shaped roughness profiles with a width of about 1.5 unit cells. They show a decreased layer distance between the topmost oxygen and zinc layers. These findings are important because they are the first results on ZnO Schottky interfaces prepared under typical ambient device processing conditions.

The unit-cell symmetry of $BiFeO_3$ thin films is determined via 3-dimensional reciprocal space mapping. The maps clearly show a phase transition from monoclinic to tetragonal symmetry when the film thickness decreases below a critical thickness, both for highly strained and moderately strained films. In the case of moderately strained films, this transition is accompanied by a change in the half-order diffraction peak pattern, which reflects an untilting of the oxygen octahedra. This establishes a definitive connection between the octahedral tilting and the symmetry changes occur-

ring at the structural transition. These results are essential for device applications, since the ferroelectric and magnetic properties are strongly related to the unit-cell symmetry and oxygen octahedral structure.

# CHAPTER I

# Introduction

## 1.1 X-ray Diffraction

X-rays are electromagnetic radiation whose wavelength range from 0.1 to 100 Å (1 Å= $10^{-10}$ m). Since their first discovery in 1895 by W. C. Röntgen [1, 2], x-rays have served as an essential tool in various research fields, such as physics, materials science, medicine, chemistry, biology, and mineralogy [3, 4]. In his first x-ray paper [1, 2], Röntgen showed a radiographic image of human hand, demonstrating that x-rays can be used as a powerful imaging tool for investigating the internal structure of an object. As can be seen in Figure 1.1, bones of the human hand could be clearly photographed with x-rays. Needless to say, x-ray imaging techniques now play a vital role in our daily lives: in medical diagnostics and for security checks at the airport.

X-ray diffraction, another very important x-ray technique, may not be as familiar as x-ray imaging to a general audience, because it is not so directly related to our everyday life. X-ray diffraction was discovered by Friedrich, Knipping, and Laue [5, 6] in April 1912 [4]. Figure 1.2 shows the first reported diffraction pattern from a copper sulfate crystal. Right after this discovery, W. L. Bragg established Bragg's law, which relates crystal lattice parameters and x-ray wavelength with the diffraction peak angles [7]. These great achievements confirmed the crystal structure theory, namely *the crystal space lattice hypothesis*, formulated by Bravais, Schönflies, Fedorov and Barlow [4]. Moreover, it allowed to determine the structure of solid materials with 10,000 times better resolution compared to the optical microscope, which was the best-resolution apparatus at that time. This discovery also spawned several other diffraction techniques, including electron diffraction and neutron diffraction, which have also been essential tools in structural studies of condensed matter. Not only inorganic materials, but also organic, and even biological materials, have been successfully investigated at the atomic or molecular levels using these techniques. The

Figure 1.1: Photograph of the bones in the fingers of a living human hand. The third finger has a ring upon it. Reprinted from Röntgen's first x-ray paper [2] with permission (© 1946, Macmillan Publishers Ltd).

well-known discovery of the double-helix structure of deoxyribose nucleic acid (DNA) by F. H. C. Crick, J. D. Watson, and R. Franklin is a very good example [8].

Having detailed information about the atomic structure of solid materials, scientists and engineers have developed various materials with marvelous properties, such as semiconductors, superconductors, super magnets, and super alloys. These materials became the building blocks of modern electronic and optical devices [personal computers, televisions, cellphones, lasers, light emitting diodes (LEDs), etc]. Moreover, the development of new drugs and biotechnology also strongly relies on structural studies based on x-ray diffraction. In this sense, x-ray diffraction has significantly influenced our daily life [4].

Significant progress has been made in X-ray diffraction and crystallography since their discovery, and measurement and analysis of powder diffraction and single crystal diffraction were well established by the late 1960s. Moreover, after development of modern computers, all analysis tools for these diffraction data have been included in computer programs, and bulk crystal structures can be precisely determined by just running the program without having a detailed knowledge of x-ray diffraction and crystallography [9]. Nevertheless, sufficient motivation still exists for studying x-ray diffraction and crystallography in the following two senses:

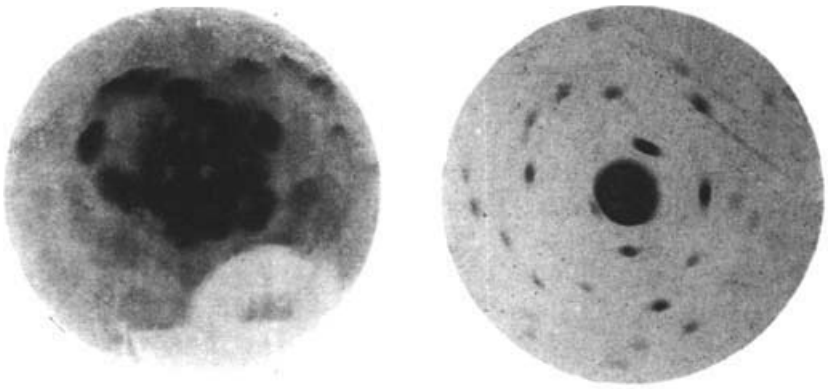

Figure 1.2: *Left*: The first reported diffraction pattern of a copper sulfate crystal, *Right*: Diffraction pattern obtained with narrower slits [4]. Reprinted from [6] with permission (© 1913, WILEY-VCH Verlag GmbH & Co. KGaA, Weinheim).

1. New techniques developed with the advancements in synchrotron x-ray sources

Since the first synchrotron radiation experiment in 1947, synchrotron technology has advanced significantly. The development of efficient electron storage rings enabled the continuous, long-term operation of accelerator-based x-ray sources, leading to second generation synchrotron sources in the 1980s. Nowadays, most synchrotron facilities are so-called third-generation light sources, which utilize insertion devices for generating radiation. By wiggling the motion of electrons in straight sections of the storage ring with the insertion devices, highly coherent and less divergent x-ray beams can be obtained with excellent brilliance [3]. As can be seen in Figure 1.3, these sources cover a wide range of accessible photon energies, and also provide almost 10 orders of magnitude brighter beams compared to conventional laboratory sources.

These brilliant and highly coherent x-ray sources enabled x-ray diffraction measurements with mono-layer sensitivity [11], which can detect very weak diffraction intensity in the form of crystal truncation rods (CTRs), which arise only from sharp boundary layers of a crystal, such as cleaved or polished crystal surfaces and heteroepitaxial interfaces. The existence of CTRs was originally predicted by M. von Laue [12, 13], and experimentally shown in 1985 by S. R. Andrews and R. A. Cowley [14]. In 1986, I. K. Robinson showed that the atomic structure of crystal surfaces can be determined by analyzing the CTR intensity [15], introducing a new technique called surface x-ray diffraction (SXRD). For a conventional powder diffraction or a single crystal diffraction, which involve only Bragg peak intensities, the measured data are modeled with a single unit cell. For SXRD, however, the CTR intensities significantly depend on the phase relation between the surface or interface domains

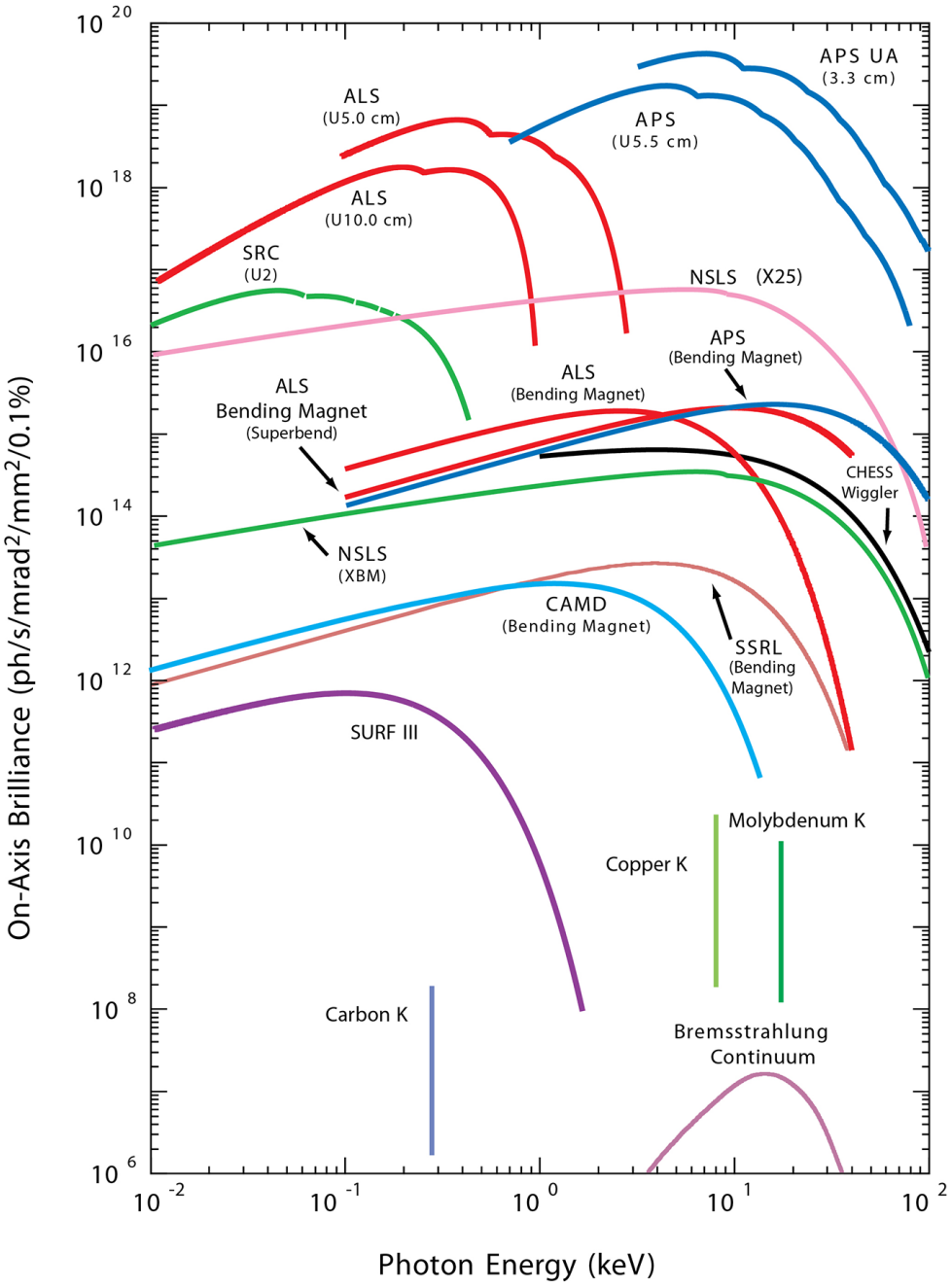


Figure 1.3: A chart comparing a variety of x-ray sources in the United States. Figure courtesy of Argonne National Laboratory, reprinted from [10] with permission.

due to the surface roughness (terraced domains) or surface reconstructions. Therefore, the CTR intensities cannot be easily modeled by just running a pre-developed software without a deeper knowledge of x-ray diffraction, and a significant effort is needed to correctly simulate the diffraction intensity and obtain a surface structure from SXRD data.

2. Epitaxial thin films: a new form of crystal

In modern technologies, thin film science plays a very important role in diverse disciplines, such as electronics, optics, aerospace and other industries. Thin films are being widely used in the forms of active devices and passive components, piezoelectric devices, sensor elements, solar energy conversion, memory devices, and many others. Thin films are more compact, reliable, cost effective, lighter, and better in performance compared to their bulk counterparts, and therefore have been preferred for device or component applications [16]. From the point of view of x-ray structural studies, however, it is usually more challenging to determine the atomic structure of thin film crystals. Bulk crystals are typically prepared in the form of a single crystal for which all the unit cells are oriented in the same direction, or as a poly-crystal or powder that consists of numerous randomly oriented crystallites. In these cases, the atomic structure of the crystal can be obtained by simply following the well-established conventional procedure of diffraction data analysis, which can be easily done by running a pre-developed computer software. Thin film crystals, however, generally fall in between the two extremes of a perfectly ordered single crystal (unit cell orientation is confined in all three dimension) and a randomly oriented poly-crystal (no confinement in unit cell orientation). Because the substrate restricts the orientation of the film only in the in-plane direction during the growth, several domains with different out-of-plane orientations can co-exist in the film, depending on the crystallographic symmetry of the film and substrate. Therefore, each structural domain contributes to the diffraction intensity differently, and they will overlap each other, typically resulting in peak splitting in the diffraction pattern. To properly deconvolute the split peak pattern to determine the unit-cell structure of the film, a rigorous knowledge of x-ray diffraction and crystallography is essential.

## 1.2 Oxide Surfaces and Interfaces

Studying the surface or interface structure of crystals and crystalline heterostructures is important both from a fundamental science point of view as well as for tech-

nical applications. In particular, oxide surfaces and interfaces have gained a burst of attention in recent years due to their interesting physical properties in magnetic, ferroic, thermal, optical, and (super)conducting properties. Oxygen atoms can induce electric fields in their compounds, which are strong enough to correlate the electrons between neighboring atoms and make them actively interact with each other. This strong correlation between electrons in oxide materials leads to many interesting physical properties and introduces a variety of potential applications such as batteries, fuel cells, transparent electronics, and low-energy information storage [17–20].

As one of the most promising oxides, zinc oxide (ZnO) has recently gained increased attention for its potential in a large variety of technological applications. With significant progress in the oxide crystal growth technologies, recently grown ZnO thin films can have 1,000 times higher electron mobility compared to the values from only three years ago, and nowadays, even the fractional quantum Hall effect can be observed in high-quality ZnO crystals [19, 21, 22]. Being itself a transparent semiconductor, ZnO has many important potential applications in fields as diverse as catalysis, gas sensing, corrosion prevention, and optoelectronics.

Needless to say, a precise knowledge of the ZnO surface and interface structures is critical to control and tailor their properties for these and other applications. In particular, details of the interface structure buried beneath metal contact layers are important in determining electronic properties such as the Schottky barrier height, which in turn governs the performance of devices such as Schottky barrier diodes (SBDs), metal-semiconductor-metal (MSM) photodetectors, and metal semiconductor field effect transistors (MESFETs) [23, 24].

Transition metal oxides (TMOs) are another heavily investigated class of oxide materials in recent years. They show very intriguing properties in bulk form, such as superconducting behavior at high temperature [25] (even significantly above liquid nitrogen temperature [26]), ferroelectricity, ferromagnetism, and multiferroicity. Moreover, at interfaces in TMO heterostructures, such as a boundary between a thin film and a substrate, very interesting phenomena can be observed; for instance, the formation of a 2D-electron gas between two insulating perovskites $LaAlO_3$ and $SrTiO_3$ [27] or a non-bulk-like crystallographic structure causing a larger spontaneous polarization of multiferroic $BiFeO_3$ thin films compared to its bulk value [28]. Depending on the interface boundary conditions, including the epitaxial strain and the tilting pattern of shared oxygen atoms, the TMO heterointerfaces in thin films show vastly different structural behavior. This results in significant changes in ferroicity, spontaneous polarization, magnetization, or conductivity, which are important

properties for many device applications. Again, a correct determination and deeper understanding of the interface structures are critical for a precise control of their physical properties, which can lead to many innovative applications of TMOs.

For investigating the surface and interface structures of these systems, SXRD and three-dimensional reciprocal space maps (3D-RSMs) play crucial roles. They provide (1) resolution at the atomic scale, (2) a large penetration depth, which is essential to investigate buried film-substrate interfaces, and (3) the capability of obtaining the global surface structure of the sample. These qualities are pre-requisites for surface and interface studies and can only partially be provided by other complementary techniques, such as Atomic Force Microscopy (AFM), Scanning Tunneling Microscopy (STM), Transmission Electron Microscopy (TEM), and Low-Energy Electron-Diffraction (LEED) [29].

## 1.3 Dissertation Outline

This dissertation will continue with Chapter II, where basic principles and concepts of x-ray scattering and SXRD will be introduced, followed by the presentation of a quantitative proper modeling scheme for SXRD intensities from rough surfaces. In Chapter III, two important oxide materials, ZnO and $BiFeO_3$, which are the main objective materials throughout this study, will be described from the fundamental origins of their physical properties to potential applications utilizing those properties. Recent research activities and open questions relating atomic structures and physical properties will also be introduced. Chapter IV will be focused on experimental facilities and data analysis methods for synchrotron x-ray diffraction experiments. Two major techniques used in this study, SXRD and 3D-RSM, will be described from experimental data acquisition to actual structure determinations. Chapter V will concentrate on the results and discussions from structural investigations on ZnO Zn-polar (0001) and O-polar ($000\bar{1}$) surfaces and Schottky interfaces. In Chapter VI, results and discussions from systematic studies on the thickness- and temperature-induced structural phase transition of ultra-thin $BiFeO_3$ films grown on (001) $SrTiO_3$ and (001) $LaAlO_3$ substrates will be shown. Finally, important results from this dissertation will be summarized in Chapter VII, with some outlooks and future directions for continuing this work.

# Bibliography


[1] W. C. Röntgen, "Über eine neue Art von Strahlen," *Sitzungsber. Der. Würzburger Physik-Medic. Gesellsch.* **137**, 132 (1895).

[2] W. C. Röntgen, "On a new kind of rays," *Nature* **53**, 274 (1896), [translated by A. Stanton].

[3] P. Willmott, *An Introduction to Synchrotron Radiation: Techniques and Applications* (John Wiley & Sons, Ltd., 2011).

[4] A. Authier, *Early days of X-ray crystallography* (Oxford, U.K : Oxford University Press, 2013).

[5] W. Friedrich, P. Knipping, and M. von Laue, "Interferenz-Erscheinungen bei Röntgenstrahlen," *Sitzungsberichte der Kgl. Bayer. Akad. der Wiss.* , 303 (1912).

[6] W. Friedrich, P. Knipping, and M. von Laue, "Interferenz-Erscheinungen bei Röntgenstrahlen," *Ann. Phys.* **346**, 971 (1913).

[7] W. L. Bragg, "The diffraction of short Electromagnetic Waves by a Crystal," *Proc. Cambridge Phil. Soc. A* **17**, 43 (1913).

[8] J. D. Watson and F. H. C. Crick, "Molecular Structure of Nucleic Acids: A Structure for Deoxyribose Nucleic Acid," *Nature* **171**, 737 (1953).

[9] G. H. Stout and L. H. Jensen, *X-ray structure determination: a practical guide, 2nd ed.* (John Wiley & Sons, Ltd., 1989).

[10] Advanced Photon Source at Argonne National Laboratory, "Insertion devices and brilliance," `http://www.aps.anl.gov/About/APS_Overview/insertion_devices.html`.

[11] I. K. Robinson, "Direct Determination of the Au(110) Reconstructed Surface by X-Ray Diffraction," *Phys. Rev. Lett.* **50**, 1145 (1983).

[12] M. von Laue, "Die äußere Form der Kristalle in ihrem Einfluß auf die Interferenzerscheinungen an Raumgittern," *Ann. Phys., Lpz.* **26**, 55 (1936).

[13] I. K. Robinson and D. J. Tweet, "Surface X-ray diffraction," *Rep. Prog. Phys.* **55**, 599 (1992).

[14] S. R. Andrews and R. A. Cowley, "Scattering of X-rays from crystal surfaces," *J. Phys. C: Solid State Phys.* **18**, 6427 (1985).

[15] I. K. Robinson, "Crystal truncation rods and surface roughness," *Phys. Rev. B* **33**, 3830 (1986).

[16] A. Goswami, *Thin Film Fundamentals* (New Age International (P) Ltd., 1996).

[17] J. Mannhart, D. H. A. Blank, H. Y. Hwang, A. J. Millis, and J.-M. Triscone, "Two-Dimensional Electron Gases at Oxide Interfaces," *MRS Bulletin* **33**, 1027 (2008).

[18] J. Chakhalian, A. J. Millis, and J. Rondinelli, "Whither the oxide interface," *Nat. Mater.* **11**, 92 (2012).

[19] J. Heber, "Materials science: Enter the oxides," *Nature* **459**, 28 (2009).

[20] H. Y. Hwang, Y. Iwasa, M. Kawasaki, B. Keimer, N. Nagaosa, and Y. Tokura, "Emergent phenomena at oxide interfaces," *Nat. Mater.* **11**, 103 (2012).

[21] "The interface is still the device [Editorial]," *Nat. Mater.* **11**, 91 (2012).

[22] Y. Kozuka, A. Tsukazaki, D. Maryenko, J. Falson, S. Akasaka, K. Nakahara, S. Nakamura, S. Awaji, K. Ueno, and M. Kawasaki, "Insulating phase of a two-dimensional electron gas in $Mg_xZn_{1-x}O$/ZnO heterostructures below $\nu = 1/3$," *Phys. Rev. B* **84**, 033304 (2011).

[23] B. J. Coppa, C. C. Fulton, S. M. Kiesel, R. F. Davis, C. Pandarinath, J. E. Burnette, R. J. Nemanich, and D. J. Smith, "Structural, microstructural, and electrical properties of gold films and Schottky contacts on remote plasma-cleaned, n-type ZnO (0001) surfaces," *J. Appl. Phys.* **97**, 103517 (2005).

[24] M. W. Allen, R. J. Mendelsberg, R. J. Reeves, and S. M. Durbin, "Oxidized noble metal Schottky contacts to n-type ZnO," *Appl. Phys. Lett.* **94**, 103508 (2009).

[25] J. Bednorz and K. Müller, "Possible high Tc superconductivity in the Ba-La-Cu-O system," *Z. Phys. B - Condens. Matter* **64**, 189 (1986).

[26] M. K. Wu, J. R. Ashburn, C. J. Torng, P. H. Hor, R. L. Meng, L. Gao, Z. J. Huang, Y. Q. Wang, and C. W. Chu, "Superconductivity at 93 K in a new mixed-phase Y-Ba-Cu-O compound system at ambient pressure," *Phys. Rev. Lett.* **58**, 908 (1987).

[27] A. Ohtomo and H. Y. Hwang, "A high-mobility electron gas at the $LaAlO_3/SrTiO_3$ heterointerface," *Nature* **427**, 423 (2004).

[28] J. Wang, J. B. Neaton, H. Zheng, V. Nagarajan, S. B. Ogale, B. Liu, D. Viehland, V. Vaithyanathan, D. G. Schlom, U. V. Waghmare, N. A. Spaldin, K. M. Rabe, M. Wuttig, and R. Ramesh, "Epitaxial $BiFeO_3$ Multiferroic Thin Film Heterostructures," *Science* **299**, 1719 (2003).

[29] C. M. Schlepütz, *Systematic Structure Investigation of YBCO Thin Films with Direct Methods and Surface X-ray Diffraction*, Ph.D. thesis, Mathematisch-naturwissenschaftliche Fakultät, Universität Zürich (2009), doi: 10.6084/m9.figshare.942424.

# CHAPTER II

# X-ray Scattering Theory

## 2.1 Introduction

The goal of this chapter is to describe how to calculate the x-ray diffraction intensity from a rough surface. In particular, we will be interested in the case of several symmetrically inequivalent surface terminations co-existing within the x-ray coherence length due to the roughness. Surface roughness can be introduced as a natural extension of the diffraction theory for smooth crystal surfaces, which is developed from the well-established kinematic approximation for bulk crystal diffraction theory.

X-ray diffraction data from bulk crystals has been a fundamental cornerstone for the success of various disciplines in science, engineering and industry. Several publications, including the well-known condensed matter physics books by C. Kittel [1] and N. Ashcroft and N. D. Mermin [2], as well as many x-ray crystallography texts [3–9] describe the underlying theory in detail. The more specific theory describing the scattering of X-rays from crystal surfaces has been developed much more recently compared to its bulk counterpart, but can be found in several articles or books nowadays [9–13].

One challenge for the novice x-ray crystallographer is the lack of a clear consensus between various textbooks regarding the definitions and mathematical notations used to describe scattering. For example, there is a factor of $2\pi$ difference between typical physics and crystallography textbooks for defining the x-ray wave vector $\mathbf{k}$, and several different notations and definitions can be found for describing the effect of thermal fluctuations on diffraction intensities (Debye-Waller factor, thermal factor, etc.). To minimize any confusion arising from these different notations, and also to present this chapter as a self-contained and easily readable account of the basic diffraction fundamentals used in this thesis without the need to extensively reference external literature, the diffraction theory for bulk crystals and for ideal and atomically

flat crystal surfaces will be briefly covered in Sections 2.2 and 2.3. The definitions and notations given in these sections will be consistently used in Section 2.4, where the x-ray diffraction from rough surfaces will be discussed. Note that most of the descriptions in Sections 2.2 and 2.3 are based on the information given in [9].

## 2.2 X-ray Diffraction from Bulk Crystals

### 2.2.1 X-ray Scattering from a Charged Particle

In classical electrodynamics theory, a charged particle will be accelerated when it is excited by a plane wave of electromagnetic radiation, and consequently it will emit radiation in directions other than that of the incident wave. This process can be understood as scattering of the electromagnetic wave by the charged particle [14].

In case of the accelerated particle moving non-relativistically, the emitted radiation has the same wavelength as the incident ray. In other words, the energy of the photon will be conserved in this scattering process, and therefore this process is called *elastic scattering* or *Thomson scattering*. For relativistic particles, part of the energy of the incident electromagnetic radiation can be transferred to the scattering particle, and therefore the scattered wave will have a longer wavelength (less energy). This process is called *inelastic scattering* or *Compton scattering*. Because no fixed phase relation between the incident and the scattered wave can be established for Compton scattering, the interference (or diffraction) pattern for the scattered wave cannot be predicted [8]. The Compton scattering cross section, however, is negligible compared to that for Thomson scattering for the wavelength range of most x-ray sources used for diffraction experiments [15]. Therefore, for practical purposes here, we only consider elastic scattering processes in the following discussion. Note however, that inelastic x-ray scattering is now widely used for studying electronic, vibrational and magnetic excitations in solids [16–18].

Let us consider the electric field of an incident plane wave with propagation vector $\mathbf{k}_0$, polarization vector $\boldsymbol{\epsilon}_0$, and amplitude $E_0$, as described in Figure 2.1. This field can be written as

$$\mathbf{E}_0(\mathbf{x}) = \boldsymbol{\epsilon}_0 E_0 e^{i\mathbf{k}_0\cdot\mathbf{x}}. \tag{2.1}$$

The charged particle at position $\mathbf{r}$ with charge $e$ and mass $m$ will feel the force $e\mathbf{E}_0$ due to the incident wave, and therefore the acceleration is

$$\dot{\mathbf{v}} = \boldsymbol{\epsilon}_0 \frac{e}{m} E_0 e^{i\mathbf{k}_0\cdot\mathbf{r}}. \tag{2.2}$$

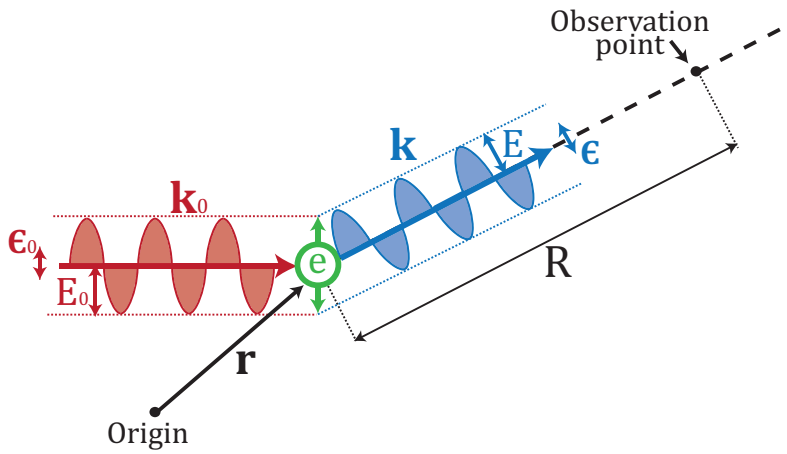


Figure 2.1: Electromagnetic radiation scattered by a charged particle.

The accelerated particle will emit radiation, and the electric field of the radiated wave propagating in the $\hat{k}$ direction at a distance R from the scatterer can be obtained in SI units [14]:

$$\begin{aligned} \mathbf{E} &= \frac{1}{4\pi\varepsilon_0}\frac{e}{c^2}\frac{\hat{k}\times(\hat{k}\times\dot{\mathbf{v}})}{R} \\ &= \frac{1}{4\pi\varepsilon_0}\frac{e^2}{mc^2}\frac{1}{R}E_0 e^{i\mathbf{k}_0\cdot\mathbf{r}}\hat{k}\times(\hat{k}\times\boldsymbol{\epsilon}_0). \end{aligned} \tag{2.3}$$

This can be re-written in the form of $\boldsymbol{\epsilon}Ee^{i\mathbf{k}\cdot\mathbf{r}}$ as

$$\mathbf{E} = \boldsymbol{\epsilon}\frac{p}{4\pi\varepsilon_0}\frac{e^2}{mc^2}\frac{1}{R}E_0 e^{i(\mathbf{k}_0-\mathbf{k})\cdot\mathbf{r}}e^{i\mathbf{k}\cdot\mathbf{r}} = \boldsymbol{\epsilon}Ee^{i\mathbf{k}\cdot\mathbf{r}}, \tag{2.4}$$

$$E = \frac{p}{4\pi\varepsilon_0}\frac{e^2}{mc^2}\frac{1}{R}E_0 e^{i(\mathbf{k}_0-\mathbf{k})\cdot\mathbf{r}}, \tag{2.5}$$

where $\boldsymbol{\epsilon} = \frac{\hat{k}\times(\hat{k}\times\boldsymbol{\epsilon}_0)}{|\hat{k}\times(\hat{k}\times\boldsymbol{\epsilon}_0)|}$ is the polarization vector and $p = |\hat{k}\times\boldsymbol{\epsilon}_0|$ is the polarization factor, which varies between 0 and 1 depending on the polarization vector of the incident wave and the propagating direction of the scattered wave.

Equation (2.4) shows that the electric field amplitude of the scattered wave is inversely proportional to the mass of the scatterer. There are two different types of charged particles in atoms: protons and electrons. The contribution of protons, however, is negligible compared to that of electrons, because protons are about 2,000 times more massive than electrons, which will result in a contribution to the scattering intensity (which is proportional to the squared magnitude of the electric field) that is about 4,000,000 times weaker than that of the electrons. Therefore, only scattering

from electrons will be considered in this treatment of x-ray diffraction. Let us define the scattering momentum transfer $\mathbf{q} \equiv \mathbf{k} - \mathbf{k}_0$. Then, using the theoretical electron radius $r_e \equiv \frac{1}{4\pi\varepsilon_0}\frac{e^2}{mc^2}$, the scattering amplitude [Equation (2.5)] can be simplified as

$$E = E_0 \frac{r_e}{R}\, p\, e^{i\mathbf{q}\cdot\mathbf{r}}. \tag{2.6}$$

### 2.2.2 X-ray Scattering from an Isolated Atom

Let us consider the electromagnetic radiation being scattered from multiple isolated charged particles. In principle, a scattered wave from one particle can be scattered again by another particle. In the case of grazing incidence angle reflectometry or when measuring the Bragg peaks of nearly perfect crystals, multiple scattering becomes significant, and the scattering should be described using the so-called *dynamical diffraction theory*, which takes the multiple scattering into account [9, 15]. In most diffraction experiments, however, the effect of multiple scattering is negligible because the x-rays interact only weakly with the electrons and therefore penetrate deeply into solid materials. For this reason, many diffraction theories are constructed using the *kinematical scattering approximation*, or *first Born approximation*, which assumes that the incident wave interacts with the charged particle only once, and ignores the effects of secondary scattering. This assumption is well-justified especially in the case of diffraction from small crystals or crystals with significant mosaicity [7]. In this dissertation, we are mainly interested in the diffraction from thin surface layers of crystals or ultra-thin films ($<$ 20 nm) with several structural domains, and therefore the kinematical scattering approximation can be safely employed for describing the x-ray scattering.

Within the kinematical approximation, the total scattering amplitude $E_{tot}$ from $n$ isolated particles at positions $\mathbf{r}_i$ ($i$=1, 2, ..., $n$) measured from a reference point $\mathbf{r}$ is the coherent sum of the scattering amplitudes from each particle:

$$E_{tot} = E_0 \frac{r_e}{R}\, p\, e^{i\mathbf{q}\cdot\mathbf{r}} \sum_{i=1}^{n} e^{i\mathbf{q}\cdot\mathbf{r}_i}. \tag{2.7}$$

This can be naturally extended to the case of a continuous distribution of charge $\rho(\mathbf{r}')$ by replacing the summation with an integral as follows:

$$E_{tot} = E_0 \frac{r_e}{R}\, p\, e^{i\mathbf{q}\cdot\mathbf{r}} \int e^{i\mathbf{q}\cdot\mathbf{r}'} \rho(\mathbf{r}') d^3\mathbf{r}'. \tag{2.8}$$

Now, consider an atom whose electrons are distributed around its nucleus with a

charge density $\rho_a(\mathbf{r}')$. Then, the scattering amplitude from the atom $E_a$ can be calculated as

$$E_a = E_0 \frac{r_e}{R}\, p\, e^{i\mathbf{q}\cdot\mathbf{r}} \int e^{i\mathbf{q}\cdot\mathbf{r}'} \rho_a(\mathbf{r}') d^3\mathbf{r}'. \tag{2.9}$$

Here, we define the *atomic form factor* $f_a(\mathbf{q})$ as

$$f_a(\mathbf{q}) = \int e^{i\mathbf{q}\cdot\mathbf{r}'} \rho_a(\mathbf{r}') d^3\mathbf{r}'. \tag{2.10}$$

Note that this form factor depends only on the scattering momentum transfer $\mathbf{q}$ and the atomic number, which determines the electron density distribution. The atomic form factor can usually be calculated as

$$f_a = f_0(\theta) + f'(w) + if''(w), \tag{2.11}$$

where $\theta$ is the scattering angle (the angle between $\mathbf{k}_0$ and $\mathbf{k}$), and $w$ is the angular frequency of the x-ray photons. The values of $f_0$, $f'$, and $f''$ for each atom are tabulated in [19]. The $f'$ and $f''$ terms represent dispersion and absorption corrections, which become significant in the vicinity of an absorption edge of the atom, but they can be approximated by zero if the x-ray energy is far away from the absorption edge.

Finally, the scattering amplitude from an isolated atom can be expressed with the atomic form factor as

$$E_a = E_0 \frac{r_e}{R}\, p\, e^{i\mathbf{q}\cdot\mathbf{r}} f_a(\mathbf{q}). \tag{2.12}$$

### 2.2.3 X-ray Scattering from Bulk Crystals

Now we are ready to describe the x-ray diffraction from a crystal. A crystal can be constructed by repeatedly attaching a periodic unit, the so-called *unit cell*. A unit cell is a parallelogram made of three unit cell vectors $\mathbf{a_1}$, $\mathbf{a_2}$, and $\mathbf{a_3}$. Translations by integral multiples of these vectors form a crystal lattice, and the crystal can be built by attaching unit cells at each lattice point. These crystal lattice points, which are the positions of each unit cell $\mathbf{r}_{uc}$, can be represented as

$$\mathbf{r}_{uc} = j_1\mathbf{a_1} + j_2\mathbf{a_2} + j_3\mathbf{a_3} \tag{2.13}$$

for $j_1$, $j_2$, and $j_3$ integers. Arbitrary numbers of atoms can be placed inside the unit cell, and the position of $j$th atom within a unit cell can be written as

$$\mathbf{r}_j = x_j\mathbf{a_1} + y_j\mathbf{a_2} + z_j\mathbf{a_3} \quad (0 \le x_j, y_j, z_j < 1). \tag{2.14}$$

Let us consider a unit cell at position $\mathbf{r}_{uc}$, which consists of $N$ atoms. For the $j^{\text{th}}$ atom located at $\mathbf{r}_j$ in the unit cell, let $f_j(\mathbf{q})$ be the atomic form factor for the momentum transfer vector $\mathbf{q}$. As described in the previous section, the total scattering amplitude from a unit cell, $E_{uc}$, can be obtained as a coherent sum of the scattering amplitudes from every atom in the unit cell as

$$E_{uc} = E_0 \frac{r_e}{R}\, p\, e^{i\mathbf{q}\cdot(\mathbf{r}+\mathbf{r}_{uc})} \sum_{j=1}^{N} e^{i\mathbf{q}\cdot\mathbf{r}_j} f_j(\mathbf{q}). \tag{2.15}$$

Here, we can define the *structure factor* $F(\mathbf{q})$ of a unit cell as

$$F(\mathbf{q}) = \sum_{j=1}^{N} f_j(\mathbf{q}) e^{i\mathbf{q}\cdot\mathbf{r}_j}, \tag{2.16}$$

and Equation (2.15) can be simplified:

$$E_{uc} = E_0 \frac{r_e}{R}\, p\, e^{i\mathbf{q}\cdot(\mathbf{r}+\mathbf{r}_{uc})} F(\mathbf{q}). \tag{2.17}$$

Note that the structure factor $F(\mathbf{q})$ contains all the information about the internal atomic structure of the unit cell, but it does not depend on the position of the unit cell $\mathbf{r}_{uc}$. Now, let us build an actual 3D crystal by stacking $N_1$, $N_2$, and $N_3$ unit cells along the $\mathbf{a_1}$, $\mathbf{a_2}$, and $\mathbf{a_3}$ directions, respectively, therefore producing a total of $N_1 \cdot N_2 \cdot N_3$ unit cells in the crystal. Then, the scattering amplitude from this crystal can be obtained as the coherent addition of the scattering amplitudes from each unit cell, which is located at $\mathbf{r}_{uc} = j_1\mathbf{a_1} + j_2\mathbf{a_2} + j_3\mathbf{a_3}$:

$$\begin{aligned} E_{crystal} &= E_0 \frac{r_e}{R}\, p\, e^{i\mathbf{q}\cdot\mathbf{r}} F(\mathbf{q}) \sum_{j_1=1}^{N_1}\sum_{j_2=1}^{N_2}\sum_{j_3=1}^{N_3} e^{i\mathbf{q}\cdot(j_1\mathbf{a_1}+j_2\mathbf{a_2}+j_3\mathbf{a_3})} \\ &= E_0 \frac{r_e}{R}\, p\, e^{i\mathbf{q}\cdot\mathbf{r}} F(\mathbf{q}) \sum_{j_1=1}^{N_1} e^{i\mathbf{q}\cdot j_1\mathbf{a_1}} \sum_{j_2=1}^{N_2} e^{i\mathbf{q}\cdot j_2\mathbf{a_2}} \sum_{j_3=1}^{N_3} e^{i\mathbf{q}\cdot j_3\mathbf{a_3}}. \end{aligned} \tag{2.18}$$

The term $\sum_{j_i=1}^{N_i} e^{i\mathbf{q}\cdot j_i\mathbf{a_i}}$ is a simple geometric series whose sum is

$$\begin{aligned} \sum_{j_i=1}^{N_i} e^{i\mathbf{q}\cdot j_i\mathbf{a_i}} &= \frac{e^{i\mathbf{q}\cdot\mathbf{a_i}}(1-e^{iN_i\mathbf{q}\cdot\mathbf{a_i}})}{1-e^{i\mathbf{q}\cdot\mathbf{a_i}}} \\ &= e^{i\mathbf{q}\cdot\mathbf{a}_i} \frac{e^{i\mathbf{q}\cdot\mathbf{a}_i N_i/2}(e^{iN_i\mathbf{q}\cdot\mathbf{a}_i/2} - e^{-iN_i\mathbf{q}\cdot\mathbf{a}_i/2})}{e^{i\mathbf{q}\cdot\mathbf{a}_i/2}(e^{i\mathbf{q}\cdot\mathbf{a}_i/2} - e^{-i\mathbf{q}\cdot\mathbf{a}_i/2})} \end{aligned}$$

$$= e^{i\mathbf{q}\cdot\mathbf{a}_i(N_i+1)/2}\frac{\sin(N_i\mathbf{q}\cdot\mathbf{a}_i/2)}{\sin(\mathbf{q}\cdot\mathbf{a}_i/2)}. \tag{2.19}$$

Finally, using the result of Equation (2.19), the total scattering amplitude from the bulk crystal, $E_{crystal}$, can be written as

$$E_{crystal} = E_0\frac{r_e}{R}\; p\; e^{i\mathbf{q}\cdot\mathbf{r}}F(\mathbf{q})e^{i\phi}\frac{\sin(N_1\mathbf{q}\cdot\mathbf{a}_1/2)}{\sin(\mathbf{q}\cdot\mathbf{a}_1/2)}\frac{\sin(N_2\mathbf{q}\cdot\mathbf{a}_2/2)}{\sin(\mathbf{q}\cdot\mathbf{a}_2/2)}\frac{\sin(N_3\mathbf{q}\cdot\mathbf{a}_3/2)}{\sin(\mathbf{q}\cdot\mathbf{a}_3/2)}, \tag{2.20}$$

where the phase factor $\phi = [(N_1+1)\mathbf{q}\cdot\mathbf{a_1} + (N_2+1)\mathbf{q}\cdot\mathbf{a_2} + (N_3+1)\mathbf{q}\cdot\mathbf{a_3}]/2$.

In real experiments, the complex scattering amplitude, $E$, cannot be directly measured. Typical photodetectors record only the scattering intensity, $I$, which is equal to the squared magnitude of the complex scattering amplitude:

$$I = |E|^2 = EE^*, \tag{2.21}$$

and therefore, the scattering intensity from the crystal, $I_{crystal}$, which is the measurable quantity of interest, can be obtained as

$$\begin{aligned} I_{crystal} &= |E_{crystal}|^2 \\ &= E_0^2\frac{r_e^2}{R^2}p^2|F(\mathbf{q})|^2|e^{i\mathbf{q}\cdot\mathbf{r}}e^{i\phi}|^2\left(\frac{\sin(N_1\mathbf{q}\cdot\mathbf{a}_1/2)}{\sin(\mathbf{q}\cdot\mathbf{a}_1/2)}\frac{\sin(N_2\mathbf{q}\cdot\mathbf{a}_2/2)}{\sin(\mathbf{q}\cdot\mathbf{a}_2/2)}\frac{\sin(N_3\mathbf{q}\cdot\mathbf{a}_3/2)}{\sin(\mathbf{q}\cdot\mathbf{a}_3/2)}\right)^2 \\ &= E_0^2\frac{r_e^2}{R^2}p^2|F(\mathbf{q})|^2\frac{\sin^2(N_1\mathbf{q}\cdot\mathbf{a_1}/2)}{\sin^2(\mathbf{q}\cdot\mathbf{a_1}/2)}\frac{\sin^2(N_2\mathbf{q}\cdot\mathbf{a_2}/2)}{\sin^2(\mathbf{q}\cdot\mathbf{a_2}/2)}\frac{\sin^2(N_3\mathbf{q}\cdot\mathbf{a_3}/2)}{\sin^2(\mathbf{q}\cdot\mathbf{a_3}/2)}. \end{aligned} \tag{2.22}$$

Now, let us define the so-called *reciprocal lattice vectors* $\mathbf{a_1^*}$, $\mathbf{a_2^*}$, and $\mathbf{a_3^*}$ from the crystal lattice vectors $\mathbf{a_1}$, $\mathbf{a_2}$, and $\mathbf{a_3}$ as follows:

$$\mathbf{a_1^*} = 2\pi\frac{\mathbf{a_2}\times\mathbf{a_3}}{\mathbf{a_1}\cdot(\mathbf{a_2}\times\mathbf{a_3})}, \quad \mathbf{a_2^*} = 2\pi\frac{\mathbf{a_3}\times\mathbf{a_1}}{\mathbf{a_1}\cdot(\mathbf{a_2}\times\mathbf{a_3})}, \quad \mathbf{a_3^*} = 2\pi\frac{\mathbf{a_1}\times\mathbf{a_2}}{\mathbf{a_1}\cdot(\mathbf{a_2}\times\mathbf{a_3})}. \tag{2.23}$$

It can be easily seen that these reciprocal lattice vectors have the property:

$$\mathbf{a_i}^*\cdot\mathbf{a_j} = 2\pi\delta_{ij}. \tag{2.24}$$

If we represent the momentum transfer vector $\mathbf{q}$ by using the reciprocal lattice vectors as its basis, $\mathbf{q}$ can be written as

$$\mathbf{q} = h\mathbf{a_1^*} + k\mathbf{a_2^*} + l\mathbf{a_3^*} \tag{2.25}$$

for some real numbers $h$, $k$, and $l$. Using the results from (2.24) and (2.25), Equa-

tion (2.22) can be simplified as

$$I_{crystal} = E_0^2 \frac{r_e^2}{R^2} p^2 |F(\mathbf{q})|^2 \frac{\sin^2(N_1 h\pi)}{\sin^2(h\pi)} \frac{\sin^2(N_2 k\pi)}{\sin^2(k\pi)} \frac{\sin^2(N_3 l\pi)}{\sin^2(l\pi)}. \tag{2.26}$$

Three squared sine functions exist in the denominator of the above expression. When all of them become zero simultaneously, the product diverges, and we expect to observe a very strong scattering intensity. This will be achieved when the following condition is met:

$$\begin{aligned} & \sin(h\pi) = \sin(k\pi) = \sin(l\pi) = 0 \\ \Leftrightarrow \quad & h,\ k,\ \text{and } l \text{ are all integers.} \end{aligned} \tag{2.27}$$

Therefore, by combining Equations (2.25) and (2.27), strong diffraction intensities are expected when $\mathbf{q}$ is equal to one of the reciprocal lattice points:

$$\mathbf{q} = H\mathbf{a}_\mathbf{1}^* + K\mathbf{a}_\mathbf{2}^* + L\mathbf{a}_\mathbf{1}^* \ \ (H,\ K,\ L:\ \text{integers}). \tag{2.28}$$

This is the so-called *Laue equation* for diffraction peaks.

Note that the diffraction condition given by the Laue equation is determined only by the lattice vectors; i.e., the overall shape of unit cell. As can be seen in Equation (2.26), another important factor exists that also affects the diffraction intensity: the *structure factor* $[F(\mathbf{q})]$. As mentioned earlier, this structure factor contains information about the internal atomic structure of the unit cell. Each diffraction peak satisfying the Laue condition may show an intensity which is significantly different from other peaks depending on its structure factor, and even zero intensity (extinction) may be observed when the structure factor becomes zero at the corresponding $\mathbf{q}$.

### 2.2.4 Diffraction Pattern and Fourier Transform

In typical x-ray scattering experiments, the distance between the detector and the scattering source is much longer than the x-ray wavelength, which is on the order of Å ($=10^{-10}$ m). Moreover, we have employed the kinematical approximation, such that multiple scattering effects can be neglected. In this case, the *Fraunhofer approximation* can be applied to obtain the diffraction pattern [20]. The diffraction amplitude can then be obtained by simply taking the Fourier transform of the electron density function of the scattering object [21].

A crystal can be represented as the convolution of crystal lattice points ($j_1\mathbf{a_1}+j_2\mathbf{a_2}+j_3\mathbf{a_3}$, $j_1$, $j_2$, $j_3$ integers) with the unit cell structure [22]. Therefore, the electron density of a crystal with $N_1$, $N_2$, and $N_3$ unit cells along each lattice vector, whose unit cell consists of $N$ atoms, can be represented as

$$\rho_{crystal}(\mathbf{r}) = \sum_{j_1=1}^{N_1}\sum_{j_2=1}^{N_2}\sum_{j_3=1}^{N_3}\delta(\mathbf{r}-\mathbf{r}_{uc}) \otimes \sum_{j=1}^{N}\rho_j(\mathbf{r}-\mathbf{r}_j) \tag{2.29}$$

for $\mathbf{r}_{uc} = j_1\mathbf{a_1} + j_2\mathbf{a_2} + j_3\mathbf{a_3}$, $\mathbf{r}_j = x_j\mathbf{a_1} + y_j\mathbf{a_2} + z_j\mathbf{a_3}$ $(0 \le x_j, y_j, z_j < 1)$, where $\rho_j$ represents the electron distribution function for the $j$th atom in the unit cell. $\otimes$ is the convolution operator, which is defined as

$$(f \otimes g)(\mathbf{x}) \equiv \int_{space} f(\mathbf{x}')g(\mathbf{x}-\mathbf{x}')d\mathbf{x}'. \tag{2.30}$$

Now, when taking the Fourier transform of the crystal's electron density, $\rho_{crystal}$, we can apply the *convolution theorem*, which states that

$$\mathscr{F}(f \cdot g) = \mathscr{F}(f) \otimes \mathscr{F}(g) \tag{2.31}$$

$$\mathscr{F}(f \otimes g) = \mathscr{F}(f) \cdot \mathscr{F}(g), \tag{2.32}$$

where $\mathscr{F}$ is a Fourier transform operator [23].

Then,

$$\begin{aligned}
\mathscr{F}\{\rho_{crystal}(\mathbf{r})\} &= \mathscr{F}\left(\sum_{j_1=1}^{N_1}\sum_{j_2=1}^{N_2}\sum_{j_3=1}^{N_3}\delta(\mathbf{r}-\mathbf{r}_{uc}) \otimes \sum_{j=1}^{N}\rho_j(\mathbf{r}-\mathbf{r}_j)\right) \\
&= \mathscr{F}\left(\sum_{j_1=1}^{N_1}\sum_{j_2=1}^{N_2}\sum_{j_3=1}^{N_3}\delta(\mathbf{r}-\mathbf{r}_{uc})\right) \cdot \mathscr{F}\left(\sum_{j=1}^{N}\rho_j(\mathbf{r}-\mathbf{r}_j)\right) \\
&\propto \sum_{j_1=1}^{N_1}\sum_{j_2=1}^{N_2}\sum_{j_3=1}^{N_3} e^{i\mathbf{q}\cdot\mathbf{r}_{uc}} \cdot \sum_{j=1}^{N} f_j(\mathbf{q})e^{i\mathbf{q}\cdot\mathbf{r}_j} \\
&= F(\mathbf{q})\sum_{j_1=1}^{N_1}\sum_{j_2=1}^{N_2}\sum_{j_3=1}^{N_3} e^{i\mathbf{q}\cdot(j_1\mathbf{a_1}+j_2\mathbf{a_2}+j_3\mathbf{a_3})},
\end{aligned} \tag{2.33}$$

where we used Equations (2.10) and (2.16). This result (2.33) is identical to that from Equation (2.18), except for some additional factors that depend on the scattering geometry and choice of the origin of the coordinate system. This confirms that, within the limits of the Fraunhofer approximation, the diffraction amplitude from a

crystal is just the Fourier transform of the electron density of the crystal. In case of a crystal with infinite extent ($N_1$, $N_2$, and $N_3 \rightarrow$ infinity), the Fourier transform (=diffraction pattern) of the crystal lattice is just its reciprocal space lattice [8].

### 2.2.5 Structure Factor of a Real Crystal

As discussed before, the structure factor [Equation (2.16)], which is given by the Fourier transform of the electron density distribution inside a unit cell, contains all the information about the atomic structure. In Equation (2.16), we assume that all the atomic sites within the unit cell are fully occupied with a single element for all unit cells. In real crystals, however, some unit cells may have vacancies at some atomic sites, depending on the crystal quality, or an atomic site might be occupied with two or more different elements in case of intermixed systems. Moreover, there can be disorder in the positions of atoms inside the unit cell due to thermal fluctuations or differing boundary conditions (for example, atoms in the unit cells near surfaces or grain boundaries can be displaced with respect to the atoms in the bulk unit cell). These effects can be included in the structure factor calculation by introducing an *atomic occupancy factor*, $\theta_j$, and a *Debye-Waller factor*, $u_j(\mathbf{q})$.

The atomic occupancy factor $\theta_j$ determines how occupied the $j$th atomic site is in the unit cell. Here, the $\theta_j$ can be simply understood as the probability of finding the $j^{\text{th}}$ atomic site being occupied with the $j^{\text{th}}$ atom. For example, if the $j^{\text{th}}$ atomic site exhibits 20% vacancies, the corresponding structure factor can be obtained by assigning $\theta_j = 0.8$. Note that the atomic vacancies in this case should be randomly distributed in space. In case of periodically ordered atomic vacancies, the structure factor should be modeled by using a larger periodic unit (unit cell). Intermixed systems, such as $La_xSr_{1-x}MnO_3$, can also be modeled with occupancy factors. In $La_xSr_{1-x}MnO_3$ crystals, the same atomic site in the unit cell can be randomly occupied either by a La atom with probability $x$, or by a Sr atom with probability $1 - x$. The structure factor in this case can be calculated by including both La and Sr atoms in the unit cell at the same position, with atomic occupancy factor $x$ and $1 - x$ for La and Sr, respectively. Again, this kind of modeling works only if the atoms of both elemental species are randomly distributed, and the case of long range periodic atomic ordering should be modeled with a larger unit cell.

The Debye-Waller factor, $u_j(\mathbf{q})$, describes the local disorder in the positions of the atoms due to imperfections in the crystallinity or thermal fluctuation. This positional disorder would be averaged over the x-ray coherence length in a real experiment, resulting in reduced diffraction intensities. In this dissertation, the Debye-Waller

factor will be defined as

$$u_j(\mathbf{q}) \equiv \exp(-\frac{1}{2}\mathbf{q}^\mathbf{t}\frac{\mathbf{B}_j}{8\pi^2}\mathbf{q}), \tag{2.34}$$

where $\mathbf{q}^\mathbf{t}$ represents the transpose of $\mathbf{q}$, and $\mathbf{B}_j$ is a symmetric dispersion matrix of the $j^{\text{th}}$ atom, which contains information about the degree of disorder in the atomic positions in each direction in space. Note that there is no consistent definition of the Debye-Waller factor within the scientific community, and several different definitions can be found in the literature [8, 9, 24, 25]. For example, the Debye-Waller factor can also be defined as $\frac{1}{2}\mathbf{q}^\mathbf{t}\frac{\mathbf{B}_j}{8\pi^2}\mathbf{q}$, which is the exponent of Equation (2.34).

After applying both the atomic occupancy factor and the Debye-Waller factor, the structure factor of a real crystal can be represented as

$$F(\mathbf{q}) = \sum_{j=1}^{N} \theta_j u_j(\mathbf{q}) f_j(\mathbf{q}) e^{i\mathbf{q}\cdot\mathbf{r}_j}, \tag{2.35}$$

and the diffraction intensity from a real crystal can be calculated by inserting this result into Equation (2.26).

## 2.3 X-ray Diffraction from Smooth Crystal Surfaces

### 2.3.1 Qualitative Picture

For a bulk crystal, which is periodic in all three lattice vector directions, the diffraction pattern consists of discrete peaks whose widths depend on the quality and the size of the crystal. Also, due to the finite-sized electron density distribution within the atoms, the diffraction intensity decays as a function of the distance from the origin of reciprocal space (Figure 2.2, left column). A crystal with a well-defined surface, however, is not infinitely periodic in all directions, because the periodicity in the surface normal direction is broken at the surface, and a different diffraction pattern is expected for surface diffraction.

A well-defined crystal surface can be constructed by multiplying the infinite crystal with a one-dimensional step function (Figure 2.2, upper row). For convenience, let the surface normal be along the $z$ direction. As discussed in Section 2.2.4, the diffraction pattern from this crystal surface can now be obtained by taking the Fourier transform of this product. The convolution theorem states that the Fourier transform of the product of two functions is equal to the convolution of the Fourier transforms of each function. Therefore, the diffraction pattern from a crystal with a well-defined surface can be represented as the convolution of the bulk diffraction pattern with a $1/q_z$

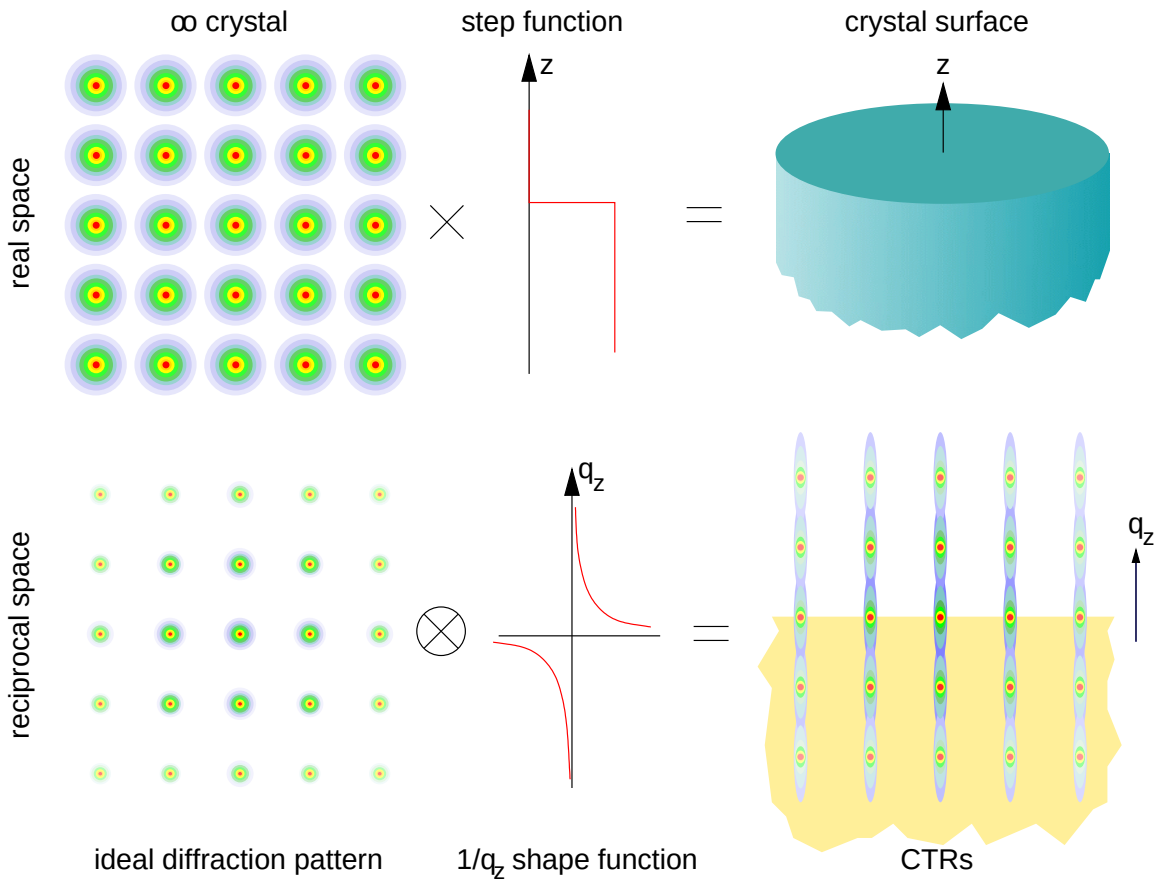


Figure 2.2: Qualitative schematics for how CTRs are formed due to the presence of a well-defined crystal surface. Reprinted from [9], with kind permission of the author.

($= 1/L$) shape function, which is the Fourier transform of the step function. Since the diffraction intensity is equal to the squared magnitude of the diffraction amplitude, the sign of the $1/q_z$ function has no effect on the intensity ($1/q_z^2$ is always positive). As described in Figure 2.2, the final diffraction pattern has strong peaks at the reciprocal lattice positions, which are broadened along the surface normal direction and result in streaks of continuous intensity along the out-of-plane direction. Since these streaks of continuous diffraction intensities, which originate from truncation of the crystal, look like rods along the surface normal, they are called *crystal truncation rods* (CTRs).

Again, without the presence of a crystal surface, the diffraction pattern is a set of discrete Bragg peaks in reciprocal space. The continuous CTR intensities between the Bragg peaks, on the other hand, originate purely from the existence of a surface. Therefore, the CTR intensities are very sensitive to the surface structure of a crystal, and the structure can be determined by analyzing the CTRs. This CTR-based surface characterization method is called *surface x-ray diffraction* (SXRD).

### 2.3.2 Mathematical Formulation

When calculating SXRD diffraction amplitudes, we can usually assume that the crystal is infinitely periodic in both in-plane directions, which are parallel to the surface. The periodicity breaks down only for the out-of-plane direction, due to the surface truncation. Therefore, we can calculate the diffraction amplitude of a unit column of the system, which represents the stacking of unit cells along the entire out-of-plane direction. By extending it in both in-plane directions, calculating the diffraction amplitudes of the entire crystal surface becomes straightforward. Let us call this unit column a *unit stack*. In a model fitting of CTR intensities, we are usually interested in non-bulk-like behavior of atoms near the surface of the crystal, such as atomic displacements from bulk positions or atomic vacancies. Therefore, we can separate the stack into two parts: one is the completely bulk-like part, where all the atoms have the identical bulk-like properties in all unit cells, and the other one is the surface part, where the atoms are allowed to deviate from their bulk properties.

Let us begin with the bulk part of the stack. As described in Section 2.2.5, the structure factor of one bulk unit cell is

$$F(\mathbf{q}) = \sum_{j=1}^{N} \theta_j u_j(\mathbf{q}) f_j(\mathbf{q}) e^{i\mathbf{q}\cdot\mathbf{r}_j}. \tag{2.36}$$

By defining the zero position of the axis along the surface normal as the boundary between the bulk part and the surface part of the stack, we require that all the unit cells below this zero position show bulk-like behavior. The bulk part of the stack can then be obtained by stacking the unit cells from $-\infty$ to $-1$ along the surface normal direction. For simplicity, let us assume that the surface normal is along the $\mathbf{a}_3$ direction. Then, the bulk contribution $F_{bulk}(\mathbf{q})$ to the stack diffraction amplitude can be calculated as

$$E_{bulk}(\mathbf{q}) = F(\mathbf{q}) \sum_{j=-\infty}^{-1} e^{i\mathbf{q}\cdot j\mathbf{a_3}}. \tag{2.37}$$

Now we can continue with the surface part of the stack. The atoms in the surface part can have different positions, occupancies, and Debye-Waller factors compared to their bulk values. Let $N_s$ be the number of atoms in the surface part of the stack. The surface atoms have their own occupancy factors $\theta_{j'}$ and Debye-Waller factors $u_{j'}$, and their positions can be described through their nominal bulk positions $\mathbf{r}_{j'}$ by adding small displacements $\mathbf{d}_{j'}$. Then, the surface contribution $F_{surf}(\mathbf{q})$ to the diffraction

amplitude becomes

$$E_{surf}(\mathbf{q}) = \sum_{j'=1}^{N_s} \theta_{j'} u_{j'}(\mathbf{q}) f_{j'}(\mathbf{q}) e^{i\mathbf{q}\cdot(\mathbf{r}_{j'}+\mathbf{d}_{j'})}, \tag{2.38}$$

and the total structure factor of a stack is

$$E_{stack}(\mathbf{q}) = E_{bulk} + E_{surf}, \tag{2.39}$$

which is the diffraction amplitude from a smooth crystal surface.

## 2.4 Roughness Modeling for Surface Diffraction

If a sample surface exhibits a roughness profile within the length scale of the coherence length of x-rays (typically a few hundred to a few thousand nm [26, 27]), the interference between photons scattered from different atomic layers affects the intensities measured on CTRs. To properly simulate the diffraction amplitude from a rough surface, this effect has to be considered in the calculation. There are two distinct methods of describing the roughness — a layer occupation model and a stack averaging model, which will be described separately in the following subsections.

### 2.4.1 Layer Occupation Model

In the layer occupation model, the surface roughness can be modeled by assigning the occupancy factors of surface atomic layers to the corresponding atomic occupation factors $\theta_i$ of each surface atom in the unit stack. In other words, we create the unit stack by laterally averaging the surface within the x-ray coherence length. As an example, let us describe the surface given in Figure 2.3 using the layer occupation model. Figure 2.3 (a) shows a surface of a simple cubic crystal whose unit cell consists of just one atom. This surface exhibits atomic layer roughness, and the occupation factors for each atomic layer are the following: layer 0 is fully occupied (occupancy 1), layer 1 is 3/4 occupied, layer 2 is 1/2 occupied, and layer 3 is 1/10 occupied. Since three atomic layers are involved in the roughness description, the surface part of the unit stack should have at least three atomic layers to properly describe the roughness. Let us consider a unit stack [marked with a red box in Figure 2.3 (a)] which has four layers of surface atoms above the bulk part. Assuming that no atoms are displaced from their bulk positions and that all atoms in the crystal have identical Debye-Waller factors, the contribution of the surface part can be calculated by assigning surface

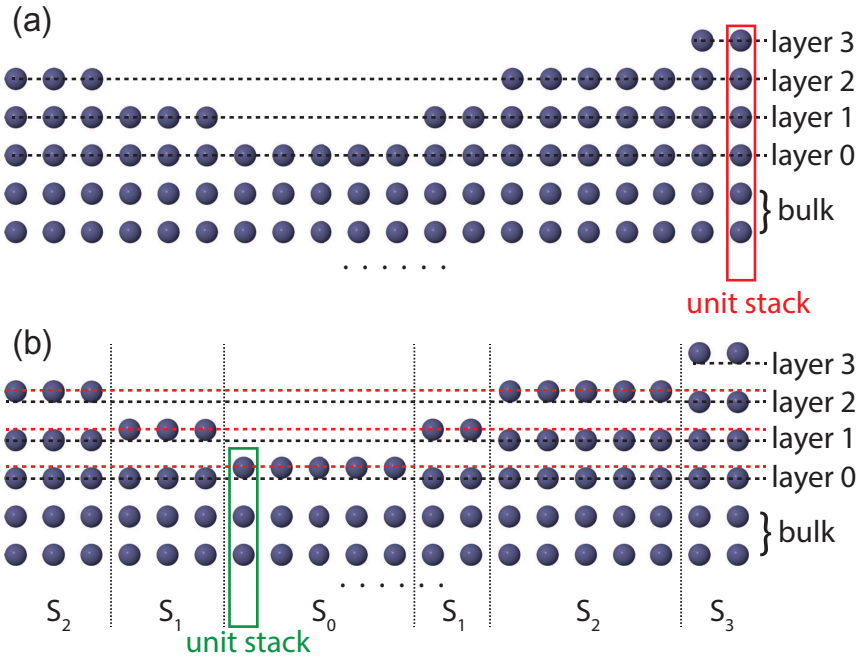


Figure 2.3: (a) A simple example of a rough crystal surface without atomic displacements (b) A rough surface which exhibits outward displacements of the topmost atoms.

layer occupancies to the corresponding $\theta_i$ as follows:

$$\begin{aligned} E_{surf}(\mathbf{q}) &= \sum_{j'=1}^{N_s} \theta_{j'} u_{j'}(\mathbf{q}) f_{j'}(\mathbf{q}) e^{i\mathbf{q}\cdot(\mathbf{r}_{j'}+\mathbf{d}_{j'})} \\ &= u_0(\mathbf{q}) f(\mathbf{q}) (e^{i\mathbf{q}\cdot\mathbf{a}_3} + \frac{3}{4} e^{i\mathbf{q}\cdot 2\mathbf{a}_3} + \frac{1}{2} e^{i\mathbf{q}\cdot 3\mathbf{a}_3} + \frac{1}{10} e^{i\mathbf{q}\cdot 4\mathbf{a}_3}). \end{aligned} \tag{2.40}$$

Using this layer occupation model, the roughness can be intuitively modeled, because the atomic occupancies of surface atoms $\theta_i$ by themselves describe the roughness profile of the surface. This model, however, has a major drawback: it cannot be applied to surfaces with atomic displacements or non-uniform Debye-Waller factors.

Let us now consider a surface where the topmost atoms are being displaced away from the crystal, as depicted in Figure 2.3 (b). In each atomic layer (layer 0-3), some of the atoms remain in their bulk-like position (all but the topmost atom in each stack) and some atoms are displaced from the bulk position (i.e., the topmost atom in each stack). In this case, the positions of each atom in the laterally averaged stack cannot be well-defined, because the different atomic displacements would be averaged over the entire layer, resulting in a wrong representation of the positions of the surface atoms. The same issue arises for non-uniform Debye-Waller factors.

### 2.4.2 Stack Averaging Model

To overcome this problem of lateral averaging in the surface direction, we must treat this roughness using the second approach alluded to above. Rather than laterally averaging the surface to construct a representative unit stack, we can build a model of the rough surface by laterally combining pre-defined unit stacks, which are shifted with respect to each other in the surface normal direction, such that they have their surface termination at different vertical positions. The diffraction amplitude of a stack, which is shifted from the original one by a translation vector $\mathbf{t}$, can be obtained by simply applying the appropriate phase factor $e^{i\mathbf{q}\cdot\mathbf{t}}$ to the original diffraction amplitude. Therefore, the total diffraction amplitude from the rough surface can be calculated by adding the diffraction amplitudes of vertically shifted stacks. This can be easily done by defining weight factors $W_{j'}$ ($\sum_{j'} W_{j'} = 1$), where $W_{j'}$ is the fraction of the surface area whose surface position can be obtained by shifting the unit stack by the vector $\mathbf{t}_{j'}$ within the x-ray coherence length.

If $N_s$ different surface termination positions are included in the model, the averaged diffraction amplitude is

$$E_{avg}(\mathbf{q}) = E_{stack} \sum_{j'=1}^{N_s} W_{j'} e^{i\mathbf{q}\cdot\mathbf{t}_{j'}}. \tag{2.41}$$

In this way, the rough surface shown in Figure 2.3 (b) can be represented using a unit stack containing only one atom (atom 0) in the surface part (marked with a green box), since only the topmost atom in the stack is behaving differently from the bulk atoms. As before, we are assuming that the figure describes the surface within the x-ray coherence length. In this example, those stacks having the same surface position as the original unit stack are occupying 1/4 of the total surface ($S_0$), and the surface, terminated at the position vertically shifted by one unit cell from the original unit stack, is also occupying 1/4 of the total surface ($S_1$). In the same way, stacks $S_2$ and $S_3$ are occupying 2/5 and 1/10 of the total surface, respectively. Therefore, the averaged total diffraction amplitude from this surface can be calculated as

$$E_{stack}(\mathbf{q}) = E_{bulk} + u_0(\mathbf{q}) f_0(\mathbf{q}) e^{i\mathbf{q}\cdot(\mathbf{r}_0+\mathbf{d}_0)} \tag{2.42}$$

$$E_{avg}(\mathbf{q}) = E_{stack}\left(\frac{1}{4}e^{i\mathbf{q}\cdot\mathbf{a}_3} + \frac{1}{4}e^{i\mathbf{q}\cdot 2\mathbf{a}_3} + \frac{2}{5}e^{i\mathbf{q}\cdot 3\mathbf{a}_3} + \frac{1}{10}e^{i\mathbf{q}\cdot 4\mathbf{a}_3}\right). \tag{2.43}$$

This model is described as the *column approximation model* by E. Vlieg [28]. This

is called 'column approximation' since it assumes that the entire surface is terminated by the identical structure apart for the vertical shifts.

The famous 'beta model' proposed by I. K. Robinson [10] is also based on the same concept as stack averaging, and this model approximates the roughness profile with a $\beta^n$ shape function. The beta model is widely used for SXRD [29–32], since the summation can be analytically calculated in a simple closed-form. Models with other functional forms as well as the $\beta^n$ model will be discussed later in Section 2.4.5 after introducing symmetry operations in the roughness modeling in the next section.

### 2.4.3 Stack Averaging with Symmetry Operations

Some crystals have more than one distinct surface termination. Especially for terraced surfaces formed by screw-axis operations (in-plane rotation combined with out-of-plane translation), such as Si (001) or ZnO (0001) surfaces, applying a simple phase factor to a unit stack is not enough to model the diffraction amplitude, because the phase relation between the diffraction amplitude of a type A to type B termination is not the same as a type B to type A.

The ZnO(0001) Zn-polar surface is a good example, because it is known that the ZnO Zn-polar (0001) surface contains two different terminations, which are 180° rotated with respect to each other, due to the triangular terraces and pits with half unit-cell step heights [33, 34]. ZnO single crystals have a hexagonal wurtzite structure as depicted in Figures 2.4 (a) and (b). Figures 2.4 (c) and (d) show the half unit-cell step height terraces of the surface. Although all terraces are terminated with atomic layers of $p3m1$ symmetry, the terminations are not identical for all terraces. As can be seen in Figure 2.4 (c) and (d), the surface terminations are rotated by 180° with respect to adjacent terraces (denoted as type A and type B). Therefore, there are two differently oriented terminations on the surface.

Let us consider the general case of a terrace surface generated by an $n$-fold screw-axis operation. The rotation operation can be described by a rotation matrix $\mathbf{R}$, and a vector $\mathbf{v}$ which gives the position of the rotation axis within the unit cell. The step height is specified by a translation vector $\mathbf{t}$ along the out-of-plane direction. Hence, the atomic coordinates of an atom originally at a position $\mathbf{r}$ will be transformed to $\mathbf{r}'$:

$$\mathbf{r}' = \mathbf{R}(\mathbf{r} - \mathbf{v}) + \mathbf{v} + \mathbf{t}. \tag{2.44}$$

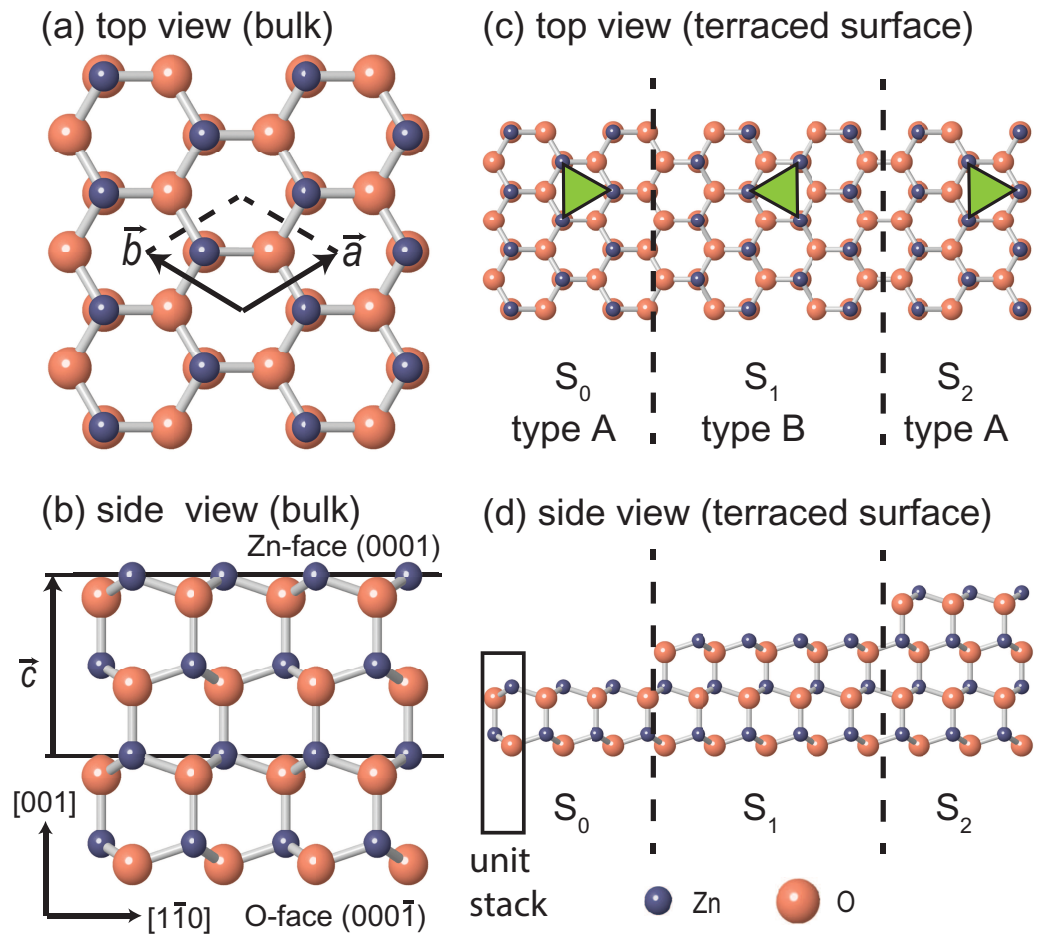


Figure 2.4: ZnO crystal structure and its terraced (0001) surface; (a) top view of a ZnO crystal, where $\vec{a}$ and $\vec{b}$ denote the in-plane lattice vectors (b) side view of a ZnO crystal, where $\vec{c}$ denotes the out-of-plane lattice vector (c) top view of a terraced ZnO (0001) surface, the green triangles highlight the type A and type B terminations, which are 180° rotated with respect to to each other. (d) side view of a terraced ZnO (0001) surface.

The only position-dependent part of the diffraction amplitude, $e^{i\mathbf{q}\cdot\mathbf{r}}$, therefore becomes

$$e^{i\mathbf{q}\cdot\{\mathbf{R}(\mathbf{r}-\mathbf{v})+\mathbf{v}+\mathbf{t}\}} \tag{2.45}$$

$$= e^{i(\mathbf{R}^{-1}\mathbf{q})\cdot\mathbf{r}} e^{i\mathbf{q}\cdot(\mathbf{t}-\mathbf{R}\mathbf{v}+\mathbf{v})}. \tag{2.46}$$

Because the Debye-Waller $u(\mathbf{q})$ is independent on translations, it becomes $u(\mathbf{R}^{-1}\mathbf{q})$ after the operation. The atomic form factor $f(\mathbf{q})$ is calculated from a spherically symmetric electron density, and hence depends only on the magnitude of the momentum transfer. Therefore, the stack diffraction amplitude $E^1_{stack}$ from a terrace, which is one step higher than the unit stack, can be calculated from the unit stack diffraction

amplitude $E^0_{stack}$ as

$$E^1_{stack}(\mathbf{q}) = E^0_{stack}(\mathbf{R}^{-1}\mathbf{q}) \cdot e^{i\mathbf{q}\cdot(\mathbf{t}-\mathbf{R}\mathbf{v}+\mathbf{v})}, \tag{2.47}$$

and that of a terrace which is $n$ steps higher than the unit stack becomes

$$E^n_{stack}(\mathbf{q}) = E^0_{stack}(\mathbf{R}^{-n}\mathbf{q}) \cdot e^{i\mathbf{q}\cdot(n\mathbf{t}-\mathbf{R}^n\mathbf{v}+\mathbf{v})}. \tag{2.48}$$

By averaging these diffraction amplitudes with the corresponding weight factors, we can obtain the total diffraction amplitude from this surface within the x-ray coherence length. In a typical CTR measurement, however, the x-rays illuminate a surface area much wider than the x-ray coherence length. Therefore, the measured intensity is a global incoherent average of diffracted intensities from local surfaces within the coherence length. This does not make any difference for surfaces with identical termination, since every local surface produces the same intensity profile. For surfaces with several different terminations, however, the intensities diffracted from each local surface can be different. This results in measured intensities which are different from each local intensity.

As an example, we can look at the ZnO (0001) surface diffraction pattern depicted in Figure 2.5. Even though each termination of the ZnO (0001) surface has a $p3m1$ symmetry (3-fold symmetry), two possible terminations exist that are rotated by 180° with respect to each other. This results in an overall $p6mm$ symmetry (6-fold symmetry) in the measured diffraction pattern. Figure 2.5 (a) shows the measured (10L) and (01L) CTRs of ZnO (0001). They are almost perfectly overlapping each other, which verifies the $p6mm$ symmetry. Figures 2.5 (b)-(d) show the simulations for these two rods. A completely bulk-like unit stack without any atomic displacement is used, and the model includes two stacks to represent the two terrace levels with the same weight factor for both terraces. Let the unit stack have type A termination. For the case where the type A terrace is lower than the type B terrace (denoted by A→B), the local diffraction amplitude and intensity are

$$E^{A\to B}_{avg}(\mathbf{q}) = \frac{1}{2}\left(E_{stack}(\mathbf{q}) + E_{stack}(\mathbf{R}^{-1}\mathbf{q})e^{i\frac{1}{2}\mathbf{a}_3\cdot\mathbf{q}}\right) \tag{2.49}$$

$$I^{A\to B} = |E^{A\to B}_{avg}|^2. \tag{2.50}$$

Figure 2.5 (c) shows this simulated intensity of the (10L) and (01L) rods for the A→B step. Even though the diffraction amplitude is a 1:1 ratio average of the diffraction amplitudes from type A and type B stacks, the intensity does not show

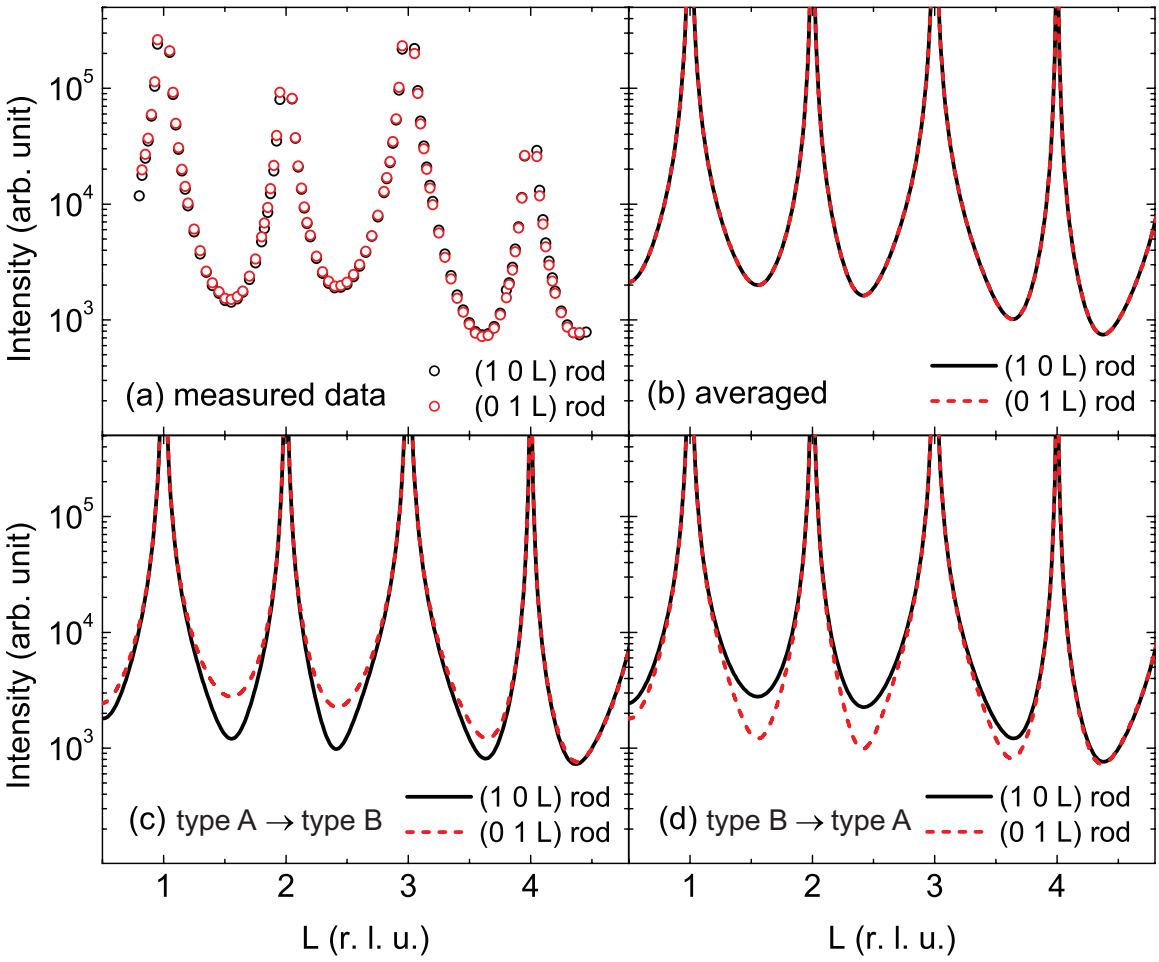


Figure 2.5: The (10L) and (01L) CTRs of the ZnO (0001) surface (a) measured data (b) averaged simulation including two types of terrace steps (c) simulation of the A→B terrace step only (d) simulation of the A→B step only.

the 6-fold symmetry of the measured data, as can be clearly seen in the region near the middle between two Bragg peaks. A B→A step (the type B terrace is lower than the type A terrace) intensity can be calculated in a similar manner as

$$E_{avg}^{B\to A}(\mathbf{q}) = \frac{1}{2}\left(E_{stack}(\mathbf{R}^{-1}\mathbf{q})e^{i\frac{1}{2}\mathbf{a}_3\cdot\mathbf{q}} + E_{stack}(\mathbf{R}^{-2}\mathbf{q})e^{i\mathbf{a}_3\cdot\mathbf{q}}\right) \quad (2.51)$$

$$I^{B\to A} = |E_{avg}^{B\to A}|^2. \quad (2.52)$$

Figure 2.5 (d) shows this calculated intensity, also with incorrect symmetry, as expected.

The correct intensity is obtained by incoherently averaging the intensities of those

two types of steps:

$$I^{avg} = \frac{(I^{A\to B} + I^{B\to A})}{2}, \tag{2.53}$$

and Figure 2.5 (b) shows the incoherently averaged intensity, which reproduces the perfect agreement between the (10L) and (01L) CTRs as observed in the experimental data.

In the general case, a minimum number $n$ of operations are required to transform a terraced domain to a terrace whose diffraction pattern is identical to that of the original terrace, and we can write the total diffracted intensity as

$$I^{avg} = \frac{1}{n}\sum_{j=0}^{n-1} I^j, \tag{2.54}$$

with

$$I^j = \left| \sum_{k=j}^{N_s+j-1} W_k E_{stack}(\mathbf{R}^{-k}\mathbf{q}) e^{i(k\mathbf{t}-\mathbf{R}^k\mathbf{v}+\mathbf{v})\cdot\mathbf{q}} \right|^2 \tag{2.55}$$

and $N_s$ is the number of different stacks included in the model.

An obvious choice for $n$ is the smallest positive integer which satisfies $\mathbf{R}^n = \mathbb{1}$ (identity matrix) and $n\mathbf{d} = n_1\mathbf{a}_1 + n_2\mathbf{a}_2 + n_3\mathbf{a}_3$ for $n_1$, $n_2$, and $n_3$ integers. For some crystals with higher surface symmetry, however, the required number of operations to achieve the same symmetry is smaller than the obvious choice described above. For example, cubic Si (001) surface terraces are related by the transformation of a quarter of out-of-plane lattice vector translation combined with a 90° rotation. Therefore, $n$=4 is the smallest integer which satisfies the above condition. Since the Si surface has two-fold symmetry, however, only two operations, which correspond to a total of a 180° rotation and a half out-of-plane lattice vector translation, are needed to obtain the identical diffraction pattern to that of the original terrace.

### 2.4.4 Defining More Unit Stacks

For simple systems such as a single crystal surface, defining one unit stack is usually enough to model the entire surface. However, more complicated systems, such as rough films deposited on rough substrates, are difficult to model with a single unit stack. Figure 2.6 describes such a case. Since the thickness of the film layers is not the same, the averaging of stacks, that are merely translations and rotations of a single stack, cannot fully reproduce the surface and interface structure. In this complicated case, we need to define more than one unit stack. In Figure 2.6, the unit stacks $S_1$, $S_2$, and $S_3$ are marked with black boxes. In principle, this system

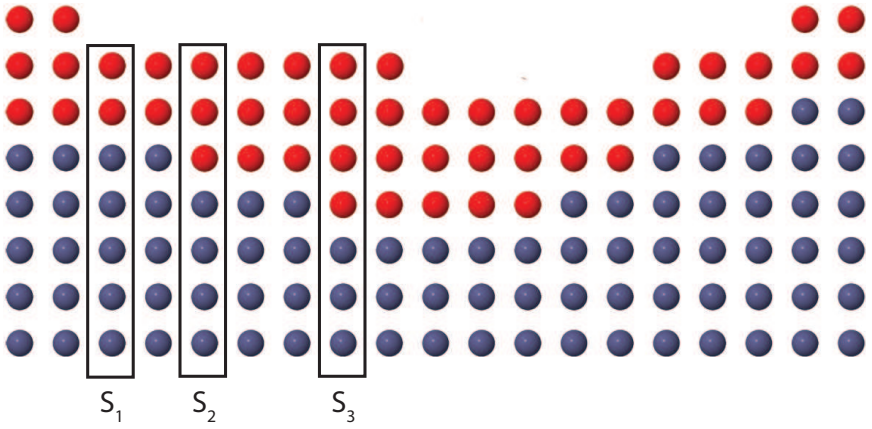


Figure 2.6: Example of a rough film (red) grown on a rough substrate (blue).

can be modeled by applying the proper transformation operations to these three unit stacks and averaging them with corresponding weight factors. However, as more and more degrees of freedom in the form of individual stacks or atomic parameters are introduced into the model, the computational complexity increases quickly, and powerful computers and algorithms are needed to perform the calculations and carry out the model fitting. One approach to mitigate this problem is to couple the atomic properties of nominally identical atoms across multiple stacks to reduce the number of free parameters. For example, we can assume that the substrate unit cells and the film unit cell right above the substrate behave identically in all three unit stacks.

### 2.4.5 Modeling Roughness Using Functional Forms

When performing a model fitting of CTRs from rough surfaces, the occupation factors of the layer occupancy model or the weight factors of the stack-averaging model can be obtained by simply fitting them as adjustable parameters. It becomes computationally demanding, however, if many layers or stacks are involved in the calculation. For efficient fitting, the occupation or weight factors can also be obtained by modeling the roughness profile with a functional form.

For the layer occupancy model, the out-of-plane roughness profile is directly related to the occupation factors for each layer. Therefore, by defining a roughness profile function $\theta(z)$ as a function of out-of-plane position $z$, the occupancy of the $i^{\text{th}}$ atom in the surface part of the unit stack, $\theta_i$, can be directly written as $\theta_i = \theta(z_i)$. If we can determine $\theta(z)$ by fitting its functional form, all occupation factors $\theta_i$ can be directly computed.

In case of the stack averaging model, the weight factors $W_i$ are not directly equal

to the layer occupancy. Since $W_i$ indicates the fraction of the surface terminated at the $i^{\text{th}}$ terrace, it can be calculated by subtracting the layer occupation of the next higher level, $\theta_{i+1}$, from that of the $i^{\text{th}}$ layer ($\theta_i$). For example, the weight factor of level $S_1$ in Figure 2.3 (b) can be obtained by subtracting the occupancy of layer 2 from that of layer 1. Therefore, the weight factor of the stacks terminated at the out-of-plane position $z$ can be calculated from the functional form as

$$W_i = \theta(z_i) - \theta(z_{i+1}). \tag{2.56}$$

Note that the weight factors obtained by taking this difference are not guaranteed to satisfy the normalization condition, $\sum_i W_i = 1$. If a simulation of the absolute intensity value is required, the weight factors obtained from functional forms should be normalized before averaging.

Three examples of functional forms — the beta, double beta, and error function — are discussed below. The ROD manual [28, 35] describes additional functional forms.

#### 2.4.5.1 The $\beta$ Roughness Model

The $\beta$ roughness model for SXRD was first proposed by I. K. Robinson [10]. The layer occupancy of the k$^{\text{th}}$ atomic layer away from the topmost fully occupied layer is described as $\beta^k$. Figure 2.7 (a) shows a few roughness profiles obtained from the $\beta$ model. As can be seen in the figure, the $\beta$ roughness model is a good approximation of an exponential roughness profile, such as that of a film deposited on some substrate, which shows a slower decrease in the layer occupation as a function of $z$ [29]. The $\beta$ model roughness factors can be summed analytically from $k$=0 to $\infty$ to obtain a simple roughness factor $R_\beta$ that depends only on $\beta$ and $q_3$, for the case of a simple cubic crystal [10]. Even for more complex crystals, E. Vlieg developed an 'approximated $\beta$ model' to describe the case of step heights of less than one unit cell [35] in the same manner. The advantage of this model is that the roughness is modeled by just applying a simple roughness factor, which can be easily calculated, to each diffraction amplitude. The $\beta$ model, however, is not adequate to describe roughness profiles with non-exponential forms, which can be found, for example, in polished crystal surfaces, which feature a rapid decrease in the surface layer occupations.

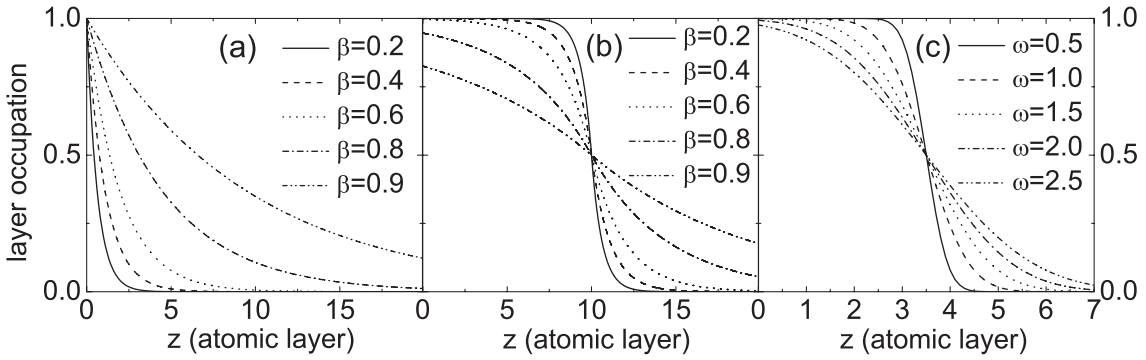


Figure 2.7: (a) $\beta$ roughness profiles for various $\beta$ values. The roughness profile shows an exponential decay. (b) Double-$\beta$ roughness profiles. The tails are longer than those of error function profile. (c) Roughness profile of various error function (integrated Gaussian) widths.

#### 2.4.5.2 The Double-$\beta$ Roughness Model

An exponential function is characterized by a sharply decreasing head and a slowly decreasing tail, as can be seen in Figure 2.7 (a). By stitching together two exponential functions back-to-back, a roughness profile with a sharply decreasing central part and slowly decreasing tails on both sides [see Figure 2.7 (b)] can be obtained. Since this profile has both sharply and slowly decaying features, it can simulate the intermixing profile at the interfaces between different materials. Letting $p$ be the position of the center of the double-$\beta$ profile, the layer occupancy factors can be calculated as

$$\theta(z) = \begin{cases} 1 - 0.5 \cdot \beta^{p-z}, & \text{if } z < p \\ 0.5 \cdot \beta^{z-p}, & \text{otherwise.} \end{cases} \tag{2.57}$$

Figure 2.7 (b) shows this profile for different $\beta$ values.

#### 2.4.5.3 The Error Function Roughness Model

In order to simulate a sharper roughness profile, an error function can be used instead of the exponential function above. Given an error function of width $w$ and position $p$, the layer occupation can be written as

$$\theta(z) = \frac{1}{2}\left\{1 + erf\left(\frac{z-p}{w}\right)\right\}. \tag{2.58}$$

Figure 2.7 (b) shows the error function roughness profiles for various widths.

## Bibliography


[1] C. Kittel, *Introduction to Solid State Physics, 8th ed.* (John Wiley & Sons, Inc., 2004).

[2] N. W. Ashcroft and N. D. Mermin, *Solid State Physics* (Thomson Learning, Inc., 1976).

[3] A. Authier, U. Bonse, R. Feder, W. Graeff, W. Hartmann, S. Kozaki, H. J. Queisser, E. Spiller, and M. Yoshimatsu, *X-ray optics: applications to solids*, edited by H. J. Queisser (Berlin; New York: Springer-Verlag, 1977).

[4] D. W. Bennett, *Understanding single-crystal x-ray crystallography* (Weinheim: Wiley-VCH, 2010).

[5] D. Liang, *Fundamentals of x-ray crystallography, 2nd ed.* (Beijing: Science Press ; Oxford, UK: Alpha Science International, 2011).

[6] G. H. Stout and L. H. Jensen, *X-ray structure determination: a practical guide, 2nd ed.* (John Wiley & Sons, Ltd, 1989).

[7] B. E. Warren, *X-ray Diffraction* (Addison-Wesley Publishing Company, Reading, Massachusetts, 1969).

[8] C. Giacovazzo, H. L. Monaco, G. Artioli, D. Viterbo, M. Milanesio, G. Ferraris, G. Gilli, P. Gilli, G. Zanotti, and M. Catti, *Fundamentals of Crystallography, 3rd ed.*, edited by C. Giacovazzo (Oxford University Press, USA, 2011).

[9] C. M. Schlepütz, *Systematic Structure Investigation of YBCO Thin Films with Direct Methods and Surface X-ray Diffraction*, Ph.D. thesis, Mathematisch-naturwissenschaftliche Fakultät, Universität Zürich (2009), doi: 10.6084/m9.figshare.942424.

[10] I. K. Robinson, "Crystal truncation rods and surface roughness," *Phys. Rev. B* **33**, 3830 (1986).

[11] I. K. Robinson and D. J. Tweet, "Surface X-ray diffraction," *Rep. Prog. Phys.* **55**, 599 (1992).

[12] E. Vlieg, J. V. D. Veen, S. Gurman, C. Norris, and J. Macdonald, "X-ray diffraction from rough, relaxed and reconstructed surfaces," *Surf. Sci.* **210**, 301 (1989).

[13] S. K. Sinha, E. B. Sirota, S. Garoff, and H. B. Stanley, "X-ray and neutron scattering from rough surfaces," *Phys. Rev. B* **38**, 2297 (1988).

[14] J. D. Jackson, *Classical Electrodynamics, 3rd ed.* (John Wiley & Sons, Inc., 1999).

[15] P. Willmott, *An Introduction to Synchrotron Radiation: Techniques and Applications* (John Wiley & Sons, Ltd., 2011).

[16] L. J. P. Ament, M. van Veenendaal, T. P. Devereaux, J. P. Hill, and J. van den Brink, "Resonant inelastic x-ray scattering studies of elementary excitations," *Rev. Mod. Phys.* **83**, 705 (2011).

[17] M. J. Cooper, W. Schülke, H. Kawata, N. Shiotani, S. Manninen, E. Zukowski, N. K. Hansen, L. Dobrzynski, P. E. Mijnarends, Y. Kubo, B. Barbiellini, A. Bansil, N. Sakai, and H. Fretwell, *X-Ray Compton Scattering*, edited by M. J. Cooper (OUP Oxford, 2004).

[18] W. Schülke, *Electron Dynamics by Inelastic X-Ray Scattering* (Oxford University Press, Oxford, 2007).

[19] E. N. Maslen, A. G. Fox, and M. A. O'Keefe, *International Tables for Crystallography Volume C: Mathematical, physical and chemical tables, First online edition*, edited by E. Prince (International Union of Crystallography, 2006) Chap. 6.1.1. X-ray scattering, pp. 554–590.

[20] M. Birkholz, *Thin Film Analysis by X-Ray Scattering* (WILEY-VCH Verlag GmbH & Co. KGaA, Weinheim, 2006).

[21] O. K. Ersoy, *Diffraction, Fourier Optics and Imaging* (John Wiley & Sons, Inc., 2007).

[22] J. P. Glusker, M. Lewis, and M. Rossi, *Crystal Structure Analysis for Chemists and Biologists* (Wiley-VCH, Inc., 1994).

[23] G. B. Arfken and H. J. Weber, *Mathematical Methods for Physicists 6th ed.* (Elsevier Inc., 2005).

[24] R. W. Grosse-Kunstleve and P. D. Adams, "On the handling of atomic anisotropic displacement parameters," *J. Appl. Crystallogr.* **35**, 477 (2002).

[25] K. N. Trueblood, H.-B. Bürgi, H. Burzlaff, J. D. Dunitz, C. M. Gramaccioli, H. H. Schulz, U. Shmueli, and S. C. Abrahams, "Atomic Dispacement Parameter Nomenclature. Report of a Subcommittee on Atomic Displacement Parameter Nomenclature," *Acta Crystallogr. A* **52**, 770 (1996).

[26] V. Kohn, I. Snigireva, and A. Snigirev, "Direct Measurement of Transverse Coherence Length of Hard X Rays from Interference Fringes," *Phys. Rev. Lett.* **85**, 2745 (2000).

[27] I. A. Vartanyants and A. Singer, "Coherence properties of hard x-ray synchrotron sources and x-ray free-electron lasers," *New J. Phys.* **12**, 035004 (2010).

[28] E. Vlieg, "*ROD*: a program for surface X-ray crystallography," *J. Appl. Crystallogr.* **33**, 401 (2000).

[29] V. Vonk, C. Ellinger, N. Khorshidi, A. Vlad, A. Stierle, and H. Dosch, "In situ x-ray study of $Fe_3Al$ (110) subsurface superlattice disordering during oxidation," *Phys. Rev. B* **78**, 165426 (2008).

[30] O. Bikondoa, W. Moritz, X. Torrelles, H. J. Kim, G. Thornton, and R. Lindsay, "Impact of ambient oxygen on the surface structure of $\alpha$-$Cr_2O_3$(0001)," *Phys. Rev. B* **81**, 205439 (2010).

[31] K. S. Tanwar, C. S. Lo, P. J. Eng, J. G. Catalano, D. A. Walko, G. E. Brown Jr., G. A. Waychunas, A. M. Chaka, and T. P. Trainor, "Surface diffraction study of the hydrated hematite surface," *Surf. Sci.* **601**, 460 (2007).

[32] T. P. Trainor, A. M. Chaka, P. J. Eng, M. Newville, G. A. Waychunas, J. G. Catalano, and G. E. Brown Jr., "Structure and reactivity of the hydrated hematite (0001) surface," *Surf. Sci.* **573**, 204 (2004).

[33] O. Dulub, L. A. Boatner, and U. Diebold, "STM study of the geometric and electronic structure of ZnO (0001)-Zn, (000$\bar{1}$)-O, (10$\bar{1}$0), and (11$\bar{2}$0) surfaces," *Surf. Sci.* **519**, 201 (2002).

[34] M. Valtiner, X. Torrelles, A. Pareek, S. Borodin, H. Gies, and G. Grundmeier, "In Situ Study of the Polar ZnO(0001)-Zn Surface in Alkaline Electrolytes," *J. Phys. Chem. C* **114**, 15440 (2010).

[35] E. Vlieg, "A concise ROD manual," `http://ftp.esrf.eu/pub/scisoft/ANA-ROD/binaries/rodmanual.pdf`.

# CHAPTER III

# Investigated Materials

## 3.1 Zinc Oxide: ZnO

### 3.1.1 Introduction

Although not known to the general public by name, zinc oxide (ZnO) has been widely used for making white pigments, enhancing the vulcanization process of rubber, and wound treatment [1, 2]. In recent years, ZnO is gaining even more attention due to its unique surface chemistry as well as optical and transport properties, which are related to many important technological applications in fields as diverse as catalysis, gas sensing, corrosion prevention, and optoelectronics [3].

Especially as a transparent direct wide band gap II-VI semiconductor (band gap 3.3 $e$V at 300 K), ZnO has been intensely investigated for electronic applications [3, 4]. Several epitaxial film and bulk crystal growth methods have been developed, and nowadays, high-quality large-area bulk single crystal wafers with a large exciton binding energy ($\sim 60\ me$V) can be readily obtained from various manufacturers [5, 6].

Several device applications of ZnO, including Schottky barrier diodes (SBDs), metal-semiconductor-metal (MSM) photodetectors, and metal semiconductor field effect transistors (MESFETs), are closely related to the interface transport properties, via the Schottky barrier height and ideality factor [7–10]. Therefore, this dissertation focuses on the Schottky interfaces between various metal contacts with large-area bulk ZnO crystal surfaces.

### 3.1.2 Basics of Schottky Interfaces[1]

Consider a metal and an n-type semiconductor. Figure 3.1 (a) shows the ideal energy-band diagram before the contact between the metal and the semiconductor is

[1]Note that most of the contents in this section are based on the information given in [8].

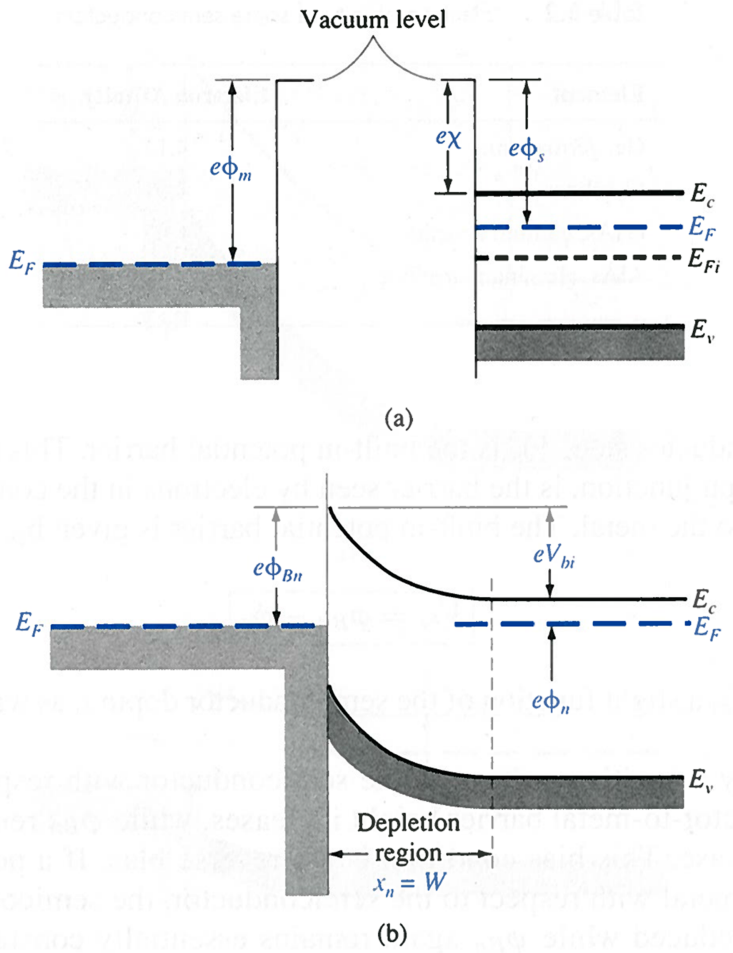


Figure 3.1: (a) Energy-band diagram of a metal and a semiconductor before making contact. (b) Ideal energy-band diagram of a metal-n-semiconductor junction in case of $\phi_m > \phi_s$. Reprinted from [8] with permission (© 1997, McGraw-Hill Education).

established. In this figure, $\phi_m$ indicates the metal work function, $\phi_s$ represents the semiconductor work function, and $\chi$ describes the electron affinity with the vacuum level as a reference. The values for work functions and electron affinities are tabulated in the literature [8] for many common contact metals. Because the metal and the semiconductor are not in contact yet, each material is in equilibrium with its own Fermi level. Once the contact is made and thermal equilibrium is achieved, the metal and semiconductor should share one Fermi level throughout the system. Therefore, during the process of reaching equilibrium, the electrons from the semiconductor flow into the metal since the metal has lower energy states. Since the donor atoms in the n-type semiconductor remain in the same positions during this process, a space charge region (or depletion region) is formed near the interface.

Figure 3.1 (b) describes the band diagram after equilibrium is established. In this figure, $\phi_{B_n}$ describes the potential energy difference between the metal and the conduction band of the semiconductor, and the electrons in the metal have to overcome this barrier to move into the semiconductor. In an ideal case, this potential barrier can be calculated as

$$\phi_{B_n} = (\phi_m - \chi), \tag{3.1}$$

and this is called the *Schottky barrier*.

The electrons in the conduction band of the semiconductor will also see a potential barrier when they flow into the metal. This intrinsic barrier without a bias voltage, $V_{bi}$, is called the *built-in potential barrier*, which is

$$V_{bi} = \phi_{B_n} - \phi_n. \tag{3.2}$$

Under the reverse bias condition (where the semiconductor is connected to the positive terminal of a voltage source, and the metal is connected to the negative terminal) with an applied bias voltage $V_R$, the potential barrier from the semiconductor into the metal increases by $V_R$, but the Schottky barrier height $\phi_{B_n}$ does not change for an ideal Schottky junction [see Figure 3.2 (a)]. In this case, the electrons in the semiconductor cannot easily flow into the metal due to the increased potential barrier.

In the case of a forward bias (metal connected to the positive terminal of the voltage source, semiconductor connected to the negative terminal), the potential barrier from the semiconductor to the metal decreases by $V_R$, while the Schottky barrier height remains constant, as in the reverse bias case [Figure 3.2 (b)]. Since the potential barrier height is reduced, the electrons in the semiconductor can easily move into the metal.

From the potential barrier behavior described above, one can expect a rectifying behavior of the Schottky junctions in their current-voltage relationship. The current transport at the Schottky interface is mainly due to thermionic emission (TE) of the majority carriers of the semiconductor. Therefore, the voltage-current (V-I) relation at the Schottky interface can be described with the following expression:

$$I = A^* T^2 \exp\Big(\frac{-q\phi_B}{kT}\Big)\Big\{\exp\Big(\frac{qV - IR_s}{nkT}\Big) - 1\Big\}, \tag{3.3}$$

where $A^*$ is the effective Richardson constant, $k$ is the Boltzmann constant, $T$ is temperature, $R_s$ is the series resistance, and $n$ is the ideality factor [7, 8]. The values of the ideality factor $n$ strongly depend on the non-ideality of the interface phenomena, such

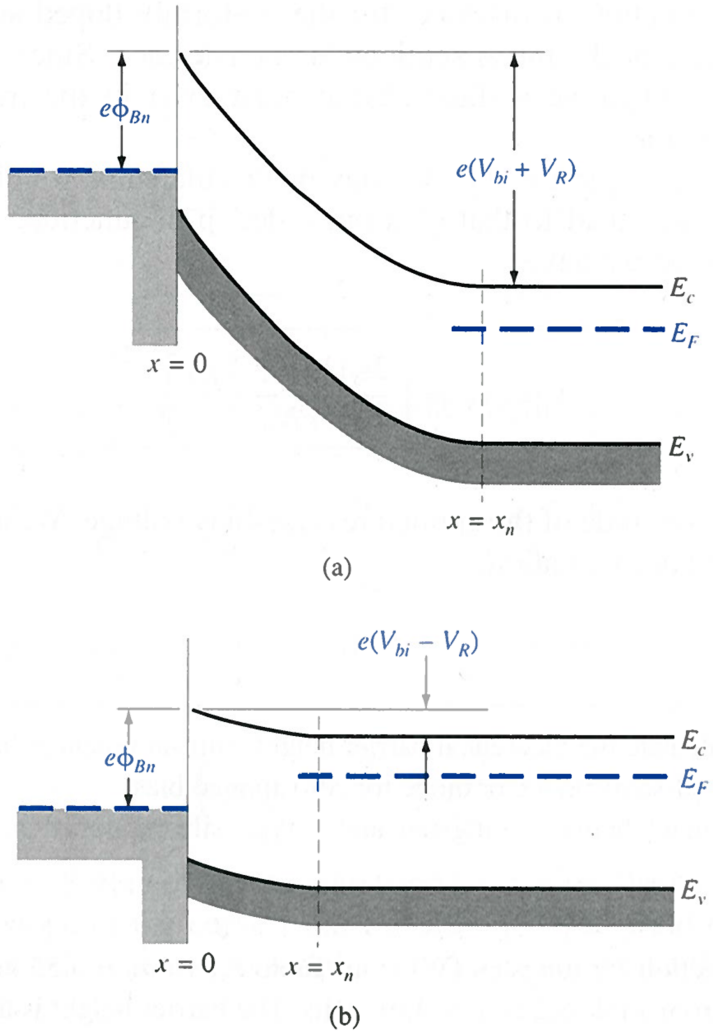


Figure 3.2: Ideal energy-band diagram of a metal-semiconductor junction (a) under reverse bias (b) under forward bias. Reprinted from [8] with permission (© 1997, McGraw-Hill Education).

as image force lowering, thermionic field emission, and lateral contact inhomogeneity, which result in $n$ greater than unity [7, 11, 12].

The description up to this point is based on the Schottky-Mott theory, where the Schottky barrier depends only on the metal work function and electron affinity of the semiconductor. In real systems, however, a more comprehensive approach, which accounts for the chemical bonding between the metal and semiconductor, is necessary to truly understand the electronic behavior of the Schottky junction. This elaborate theoretical approach is beyond the scope of this dissertation, but interested readers are referred to a review article by R. T. Tung [11].

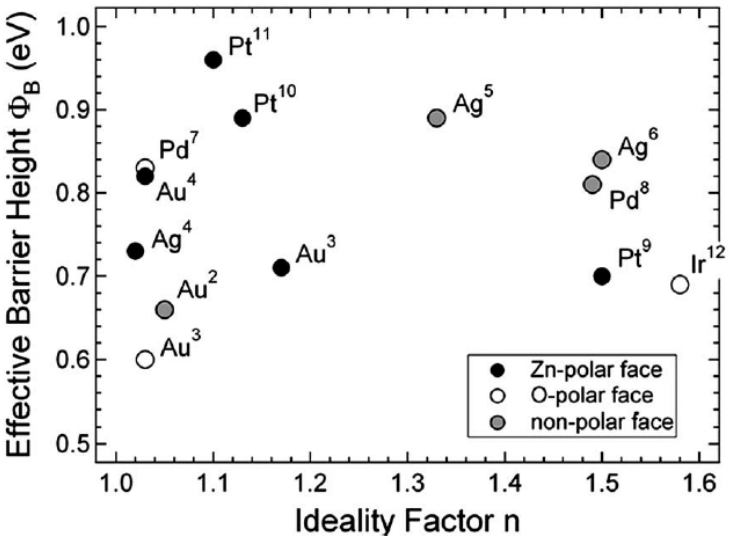


Figure 3.3: Effective barrier height ($\Phi_B$) vs ideality factor ($n$) for the best reported Schottky contacts on n-type ZnO. Reprinted from [7] with permission (© 2007, AIP Publishing LLC).

### 3.1.3 Motivation to Study ZnO Schottky Interfaces

In 1965, C. A. Mead first reported the Schottky barrier heights between vacuum cleaved ZnO surfaces and several metal contact layers [13], and ZnO Schottky contacts have been intensively studied for several different metals including Pt, Pd, Au, Ag, and Ir [6, 7, 10, 13–24]. The current transport performance of Schottky contacts can be described with two main parameters: the effective barrier height $\Phi_B$ and the ideality factor $n$ [see Equation (3.3)], and the best reported values in the literature can be found in Figure 3.3.

As can be seen in the figure, significantly different $\Phi_B$ and $n$ values are reported even for the same metal contact and the same surface termination. This is because the performance of Schottky contacts can be significantly influenced by surface morphology, surface states, chemical bonding between the semiconductor and metal, and substrate defects [6].

Therefore, a precise knowledge of the structural properties of the Schottky interfaces is a prerequisite for understanding the performance of the Schottky contacts, which is essential for controlling and optimizing their properties for device application. However, despite a large number of experimental and theoretical studies, the respective structures of ZnO surfaces and interfaces remain a topic of debate, with many alternative structures already described [3, 25–37]. This lack of consensus arises primarily from the competition of various surface stabilization mechanisms and

a host of different preparation procedures and conditions. Indeed, one expects the phase diagrams arising from the various stabilization mechanisms which compensate the energetic instability of polar ZnO surfaces to be quite complex [26, 34].

The problem is compounded by the widely differing conditions under which samples are prepared for these studies, ranging from sputter cleaning and annealing in ultra-high vacuum (UHV) to organic solvent cleaning in ambient environments commonly used in device fabrication and processing. Samples prepared under the latter conditions are the focus of the current studies reported here.

Particularly for the ZnO O-polar $(000\bar{1})$ surfaces, there is a distinct lack of reliable structural information. Previous studies report the bare surface to be terminated by hydrogen adatoms bound to the surface oxygen [35, 37, 38], but it is not clear what happens to these hydroxyl groups once a conducting contact layer is deposited. Scanning tunneling microscopy (STM) measurements with high resolution are challenging due to the poor conductivity of the surface, especially at room temperature [39, 40]. Diffraction experiments have been carried out in UHV [25, 33], but not under conditions typical for device fabrication. Surface X-ray diffraction (SXRD) offers the capability to access the surface and buried interface structures non-destructively under typical device fabrication conditions, and provides picometer accuracy for the determination of atomic positions.

With this motivation, this dissertation firstly focuses on a systematic SXRD study of the atomic structure of uncoated ZnO Zn-polar (0001) and O-polar $(000\bar{1})$ surfaces and metal Schottky contacts to ZnO prepared under typical device fabrication conditions. Again, Schottky contacts are important building blocks in many electronic devices, and an understanding of their interface structure is crucial, since electronic and structural properties are usually strongly correlated. This is particularly true for semiconductors characterized by highly ionic bonding (e.g., ZnO), in which small atomic displacements can potentially result in large changes in electronic behavior. The work on ZnO polar surfaces summarized here is published in two papers accepted in *J. Phys.: Condens. Matter* [41] and *Surf. Sci.* [42].

### 3.1.4 Sample Preparation

The ZnO Schottky interface structural study presented here has been conducted in collaboration with the research group of Prof. Steven M. Durbin (currently at Western Michigan University, Michigan, USA) and Dr. Martin W. Allen at the University of Canterbury, Christchurch, New Zealand. All the samples for this study were prepared in New Zealand by these collaborators.

Table 3.1: List of investigated ZnO Zn-polar (0001) samples. SF denotes structure factor. The SXRD data were measured either at beamline X04SA of Swiss Light Source (SLS) or at Sector 13-BM-C of Advanced Photon Source (APS).

| Sample | 1 | 2 | 3 | 4 | 5 | 6 | 7 |
|---|---|---|---|---|---|---|---|
| Cap layer | - | - | - | Au | Au | IrOx | IrOx |
| Thickness [nm] | - | - | - | 40 | 25 | 40 | 25 |
| Beamline | SLS | SLS | SLS | SLS | APS | SLS | APS |
| Total SF | 1180 | 2082 | 2446 | 1891 | 997 | 2030 | 596 |
| Averaged SF | 536 | 699 | 629 | 651 | 606 | 683 | 416 |
| $\sigma_{\text{sym}}$ [%] | 5.3 | 8.7 | 8.6 | 8.5 | 8.5 | 9.7 | 6.4 |

#### 3.1.4.1 ZnO Zn-polar (0001) Surfaces

Single-crystal ZnO (0001) wafers were hydrothermally grown along the +c-axis by Tokyo Denpa Co., Ltd. and epi-polished to low miscut angles ($< 0.1^{\circ}$) [43]. The investigated samples are listed in Table 3.1. For measurements on uncoated surfaces, samples 1-3 were ultrasonically cleaned using organic solvents, dried in $N_2$, and subsequently exposed to air. Polycrystalline Schottky contacts were deposited on other samples after the same cleaning procedure, either as plain gold by thermal evaporation (samples 4,5) or in the form of non-stoichiometric iridium oxide ($IrO_x$) layers by eclipse pulsed laser deposition (EPLD) in an oxygen ambient (samples 6,7). The latter method has been shown to produce high quality Schottky contacts to ZnO [10].

#### 3.1.4.2 ZnO O-polar ($000\bar{1}$) Surfaces

Uncoated, plain-metal-coated, and oxidized-metal-coated samples were prepared from hydrothermally grown and epi-polished ZnO wafers (miscut $< 0.1^{\circ}$) supplied by Tokyo Denpa Co., Ltd. Table 3.2 gives a list of the investigated samples. Three samples for each of the uncoated, plain metal-coated, and oxidized metal-coated sample groups were investigated in order to verify the reproducibility of the results. All samples were cleaned using only mild solvents as described previously [6], as this is the optimal treatment for Schottky fabrication. Schottky contact layers of gold (Au: sample 4) were deposited by thermal evaporation, silver (Ag: sample 5, 6) layers by radio frequency (RF) sputtering of an Ag target using a pure argon atmosphere [6], and non-stoichiometric silver oxide ($AgO_x$: sample 7, 8) was deposited by reactive RF sputtering of an Ag target in an argon/oxygen atmosphere [7]. Another sample with a non-stoichiometric iridium oxide contact ($IrO_x$: sample 9) was grown by

Table 3.2: List of investigated ZnO O-polar $(000\bar{1})$ samples. SF denotes structure factor. The SXRD data were measured either at beamline X04SA of Swiss Light Source (SLS) or at Sector 13-BM-C and Sector 33-ID-D of Advanced Photon Source (APS13 and APS33, respectively).

| Sample No. | 1 | 2 | 3 | 4 | 5 | 6 | 7 | 8 | 9 |
|---|---|---|---|---|---|---|---|---|---|
| Cap layer | - | - | - | Au | Ag | Ag | $AgO_x$ | $AgO_x$ | $IrO_x$ |
| Thick. [nm] | - | - | - | 30 | 50 | 50 | 50 | 50 | 40 |
| Beamline | SLS | APS33 | APS13 | SLS | APS13 | APS13 | APS13 | APS13 | APS33 |
| Total SF | 1048 | 2032 | 636 | 1320 | 714 | 605 | 518 | 600 | 1063 |
| Averaged SF | 542 | 1033 | 455 | 597 | 461 | 418 | 359 | 417 | 650 |
| $\sigma_{\text{sym}}$ [%] | 11.5 | 9.0 | 8.7 | 8.9 | 8.2 | 19.0 | 7.5 | 8.1 | 13.6 |

EPLD of an Ir target in an oxygen ambient [10]. All contact layers were deposited at room temperature. Non-stoichiometric silver oxide and iridium oxide contacts to the O-polar face of ZnO form very good quality Schottky contacts with ideality factors approaching unity, whereas the rectifying performance of plain metal Au and Ag contacts on the O-polar face is significantly worse with lower barrier heights, higher ideality factors, and higher leakage currents [6, 7, 10].

## 3.2 Bismuth Ferrite: $BiFeO_3$

### 3.2.1 Multiferroics

K. Aizu defined the term *ferroic* in his paper published in 1970 as the following [44]: "A crystal is provisionally referred to as being '*ferroic*' when it has two or more orientation states in the absence of magnetic field, electric field, and mechanical stress, and can shift from one to another of these states by means of a magnetic field, an electric field, a mechanical stress, or a combination of these." Figure 3.4 describes hysteresis loops that can be observed from three well-known ferroicities: ferroelectricity, ferromagnetism, and ferroelasticity. As can be seen in the figure, ferroelectric materials show hysteretic behavior in their spontaneous polarization ($P_i$), which is induced by an electric field. Similarly, ferromagnetic and ferroelastic materials exhibit hysteresis in their spontaneous magnetization ($M_i$) and elastic strain ($e_{ij}$), which can be triggered by a magnetic field and uniaxial stress, respectively [45].

In modern technology, ferroic materials are playing a crucial role in various aspects. Ferromagnetic materials are widely used in data storage devices, and researches are actively pushing to fully utilize their potential for high-density integration and better energy efficiency in so-called "spintronic" devices. Ferroelectric materials are essential for the actuator and sensor industry, which makes use of the switching prop-

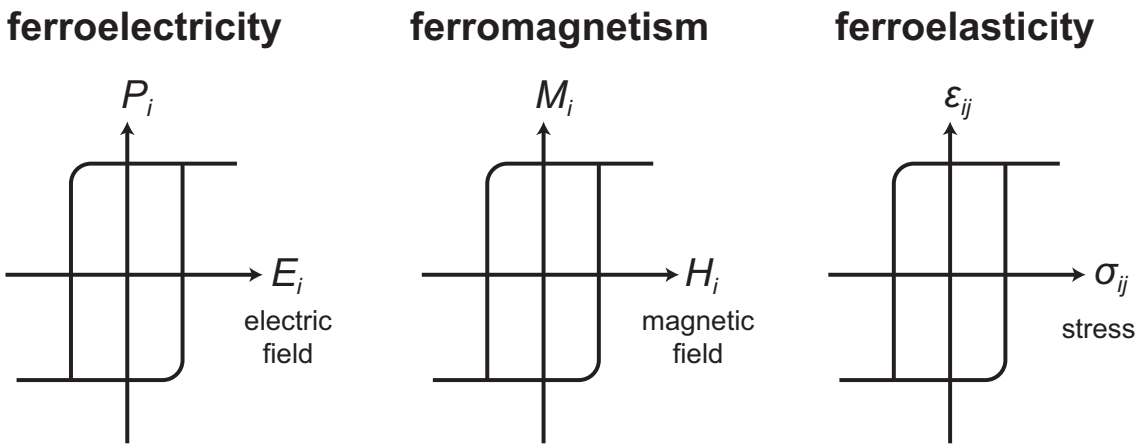


Figure 3.4: Typical hysteresis loops for ferroelectric, ferromagnetic, and ferroelastic materials. $P_i$, $M_i$, and $\varepsilon_{ij}$ represent a component of spontaneous magnetization, spontaneous polarization, and spontaneous elastic strain.

erties of their spontaneous polarization [46, 47]. Ferroelastic materials are playing an important role in earth sciences, especially in mineralogy, and also in shape memory alloy applications [48].

Some materials can exhibit more than one type of ferroic properties simultaneously. These materials are referred to as *Multiferroics*. In most multiferroics, those ferroic characteristics not only just co-exist, but interact with each other. Figure 3.5 shows the coupling between three major ferroic order parameters and their driving fields. This interaction allows controlling one of the order parameters by driving fields for another one. For example, in case of a magnetoelectric multiferroics (materials with both ferroelectric and ferromagnetic ordering), the magnetization $M$ can be controlled by an electric field, or the polarization $P$ can be controlled by a magnetic field.

In the real world, it is not difficult to find ferroelectric-ferroelastic multiferroics, since most ferroelectric materials show an excellent performance as ferroelastics or piezoelectrics as well on account of their crystal point symmetries. They are already being used in broad applications where conversion between the elastic and electric energy is needed [46, 47].

Magnetoelectric multiferroics, however, are less common compared to the ferroelectric-ferroelastic multiferroics, mainly due to a symmetry argument. Consider a ferroelectric material, which exhibits a spontaneous polarization. When an inversion symmetry operation is applied in the direction of the polarization, the system will undergo a measurable structural rearrangement, because the polarization vector has been flipped

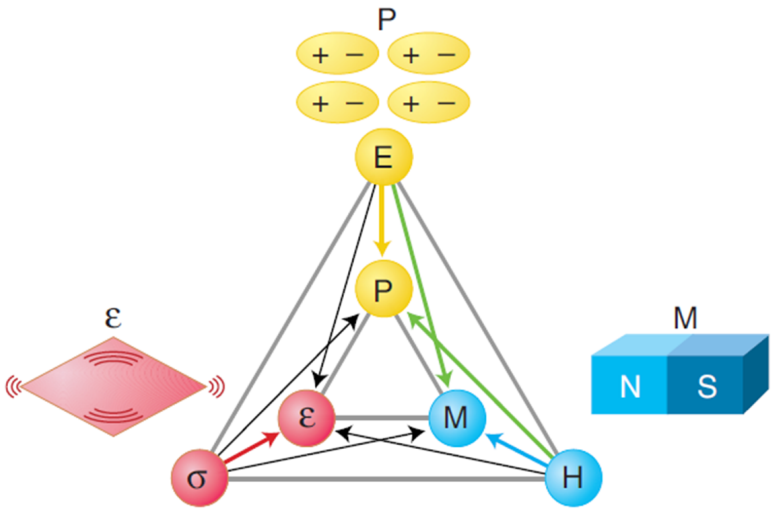


Figure 3.5: Coupling diagram for three different ferroic order parameters. Polarization ($P$), magnetization ($M$), and strain ($\varepsilon$) can interact with each other, so that each order parameter can be controlled via an external field other than its intrinsic one. Reprinted from [46] with permission (© 2005, The American Association for the Advancement of Science).

by this operation. Therefore, to exhibit a spontaneous polarization, the system has to have a broken inversion symmetry at least in the direction of the polarization. In case of a spontaneous magnetism, rather than the spacial symmetry, time reversal symmetry should be broken. In a simple heuristic argument, the magnetization (or spin) in the $z$ direction can be described by a counterclockwise rotating electron in the $x$-$y$ plane. If we reverse the time, the electron will now be rotating in a clockwise direction, and consequently the magnetization direction will be flipped, so the time reversal symmetry is broken. Therefore, both spatial inversion and time reversal symmetries should be broken in magnetoelectric multiferroics. Only 13 point groups among the total 233 Schubnikov magnetic point groups can exhibit the simultaneous symmetry breaking of those two [47], therefore severely limiting the number of possible structures for magnetoelectric multiferroics.

In spite of their scarcity, magnetoelectric multiferroics are gaining more attention, particularly in light of the tendency towards smaller and higher density devices with better energy efficiency. Coupling between ferroelectricity and ferromagnetism can allow a single device to have multiple functions and also support low-energy information storage devices via controlling the electric polarization with a magnetic field rather than an electric field [46].

Numerous attempts have been made to find stable room-temperature magneto-

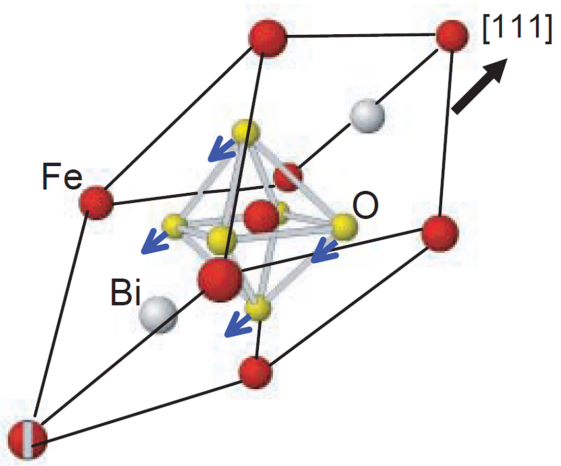


Figure 3.6: Rhombohedral unit cell structure of bulk $BiFeO_3$. Red, white and yellow atoms represent iron, bismuth, and oxygen atoms, respectively. The displacement of the oxygen octahedron (blue arrows) relative to the centered Fe atom produces the ferroelectric polarization. Reprinted from [49] with permission (© 2003, The American Association for the Advancement of Science).

electric multiferroics, but there is only one such material which has been found so far: bismuth ferrite ($BiFeO_3$). This material is one of the main topics of this dissertation and will be introduced in detail in the following section.

### 3.2.2 $BiFeO_3$

As one of the few room temperature multiferroic materials (ferroelectric: $T_C \sim 1103$ K, antiferromagnetic: $T_N \sim 643$ K) and the only known one that is a stable phase, bismuth ferrite ($BiFeO_3$) has been studied extensively in recent years [49–60]. The bulk form of $BiFeO_3$ is known to have a rhombohedrally distorted quasi-cubic perovskite structure with $a = b = c = 5.633$ Å, $\alpha = \beta = \gamma = 59.4°$, and an $a^-a^-a^-$ (Glazer notation [61]) octahedral tilt pattern [62], exhibiting both anti-ferrodistortive displacements and a spontaneous polarization along the <111> pseudocubic axes. This rhombohedral unit cell is depicted in Figure 3.6.

The ferroelectric ordering in this case is accompanied by a distortion of the unit cell structure. There are two main mechanisms that can chemically stabilize the distortion: 1) the ligand-field hybridization of a transition metal atom with its surrounding anions, and 2) the existence of lone-pair ions in the unit cell [47]. The ferroelectricity of $BiFeO_3$ originates from the latter mechanism—the lone pair electrons in the $Bi^{3+}$ ion [47].

Lone pair electrons are two valence electrons which do not form an (sp)-hybridized chemical bonding. For example, two s-orbital electrons in $Bi^{3+}$ or $Pb^{3+}$ ions can become an unstable lone pair instead of forming a stable $sp^2$ or $sp^3$ bonding state, so they contribute to a mixing between the $(ns)^2$ ground state and lower excited states such as $(ns)^1(np)^1$. This unusual chemical activity can stabilize the off-centering of the lone pair ion, which brakes the inversion symmetry, eventually resulting in the ferroelectricity. $PbTiO_3$, $Na_{0.5}Bi_{0.5}TiO_3$, $BiFeO_3$, and $BiMnO_3$ are famous examples of lone-pair induced ferroelectrics [47].

$BiFeO_3$ exhibits the typical $ABO_3$ perovskite structure, with $Bi^{3+}$ ions, which are responsible for the ferroelectric ordering, occupying the A-sites. $Fe^{3+}$ ions, with Fe being one of the most prominent magnetic transition metals, are located at the B-sites of $BiFeO_3$, and they contribute to the antiferromagnetic ordering of this material. These features are the origin of the multiferroicity of $BiFeO_3$.

The ferroelectric polarization of $BiFeO_3$ measured in the early days (in 1960s) was only a few $\mu C\,cm^{-2}$ [63], which is not sufficient for device applications. In recent years, however, the ongoing development and improvement of crystal growth methods enabled the synthesis of high-quality $BiFeO_3$ crystals, which resulted in a 10-fold improvement in the ferroelectric polarization. Moreover, modern film-growth technology has allowed high-quality heteroepitaxial growth of $BiFeO_3$ on various substrates, opening the door for practical device applications of this material [47].

When epitaxial $BiFeO_3$ thin films are grown under a compressive strain on (001)-oriented perovskite substrates, several studies [50, 52, 55–57] have reported that the polarization direction is tilted towards the [001] out-of-plane direction, while maintaining a significant in-plane component, depending on the amount of epitaxial strain from the substrate. This effect is accompanied by a significant enhancement of the spontaneous polarization and a series of phase transitions from rhombohedral (R), for small strains, to R-like monoclinic ($M_A$) to T-like monoclinic ($M_C$) and to tetragonal (T), for larger strains, the latter two of which exhibit a giant c/a ratio [55, 56]. Here, $M_C$ denotes a monoclinic structure with the ferroelectric polarization vector ($\mathbf{P}$) parallel to the $[u0v]$ or $[0uv]$ pseudocubic direction, whereas in the $M_A$ monoclinic structure, the polarization is parallel to the $[uuv]$ $(u < v)$ pseudocubic direction [64]. Bismuth ferrite films (thickness > 26 nm) grown on (001) $SrTiO_3$ (STO) substrates (-1.4% compressive strain) exhibit the R-like monoclinic structure ($M_A$) with a c/a ratio close to unity [56, 57, 65]. When deposited on $LaAlO_3$ substrates (-4.3% compressive strain), the films (thickness > 20 nm) show the T-like monoclinic structure ($M_C$) with enhanced c/a ratio ($\sim$ 1.23) [52, 56, 66].

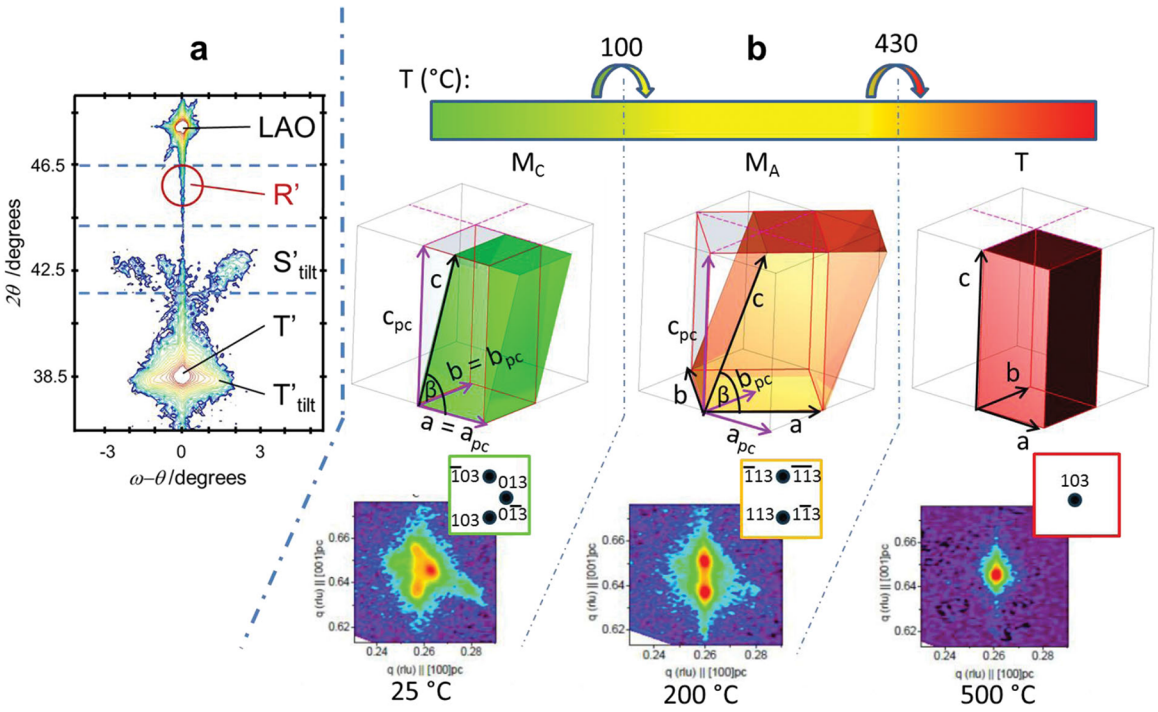


Figure 3.7: (a) X-ray diffraction reciprocal space map from ($\omega$-$\theta$, $2\theta$) scans on a $\sim$ 45 nm $BiFeO_3$ film grown on a $LaAlO_3$ substrate. (b) Temperature dependence of the unit-cell symmetry of the film, observed from the reciprocal space maps of $103_{pc}$ peaks. The subscript pc denotes pseudocubic. Reprinted from [66] with permission (© 2013, WILEY-VCH Verlag GmbH & Co. KGaA, Weinheim).

Several structural domains co-exist in $BiFeO_3$ films grown on $SrTiO_3$ and $LaAlO_3$ substrates, due to four possible orientations of monoclinic unit cells relative to the pseudocubic substrate lattice. Especially for the films on $LaAlO_3$ substrates, different unit-cell structures can be found at the boundary between those domains. Figure 3.7 (a) shows the reciprocal space map of $BiFeO_3$ grown on $LaAlO_3$, obtained from ($\omega$-$\theta$, $2\theta$) scans. The monoclinic domains contribute to the intense peak marked with 'T', and the tilted unit cells at the domain boundary produce the weak peaks marked with 'S'. Moreover, a structural phase transition from $M_C$ to $M_A$ to T can be observed at approximately 100 °C and 430 °C, respectively, as described in Figure 3.7 (b) [66]. $BiFeO_3$ films grown on $SrTiO_3$ substrates also exhibit a structural phase transition from $M_A$ to $M_C$ when heated above 740 °C, and there is another structural phase transition near 860 °C [67]. Since it is difficult to measure the film structure reliably at such high temperatures, no reported unit cell structure above 860 °C exist yet.

As discussed above, the $BiFeO_3$ films clearly show structural transitions induced by epitaxial strain and temperature. Here, we can raise one question: if applying higher

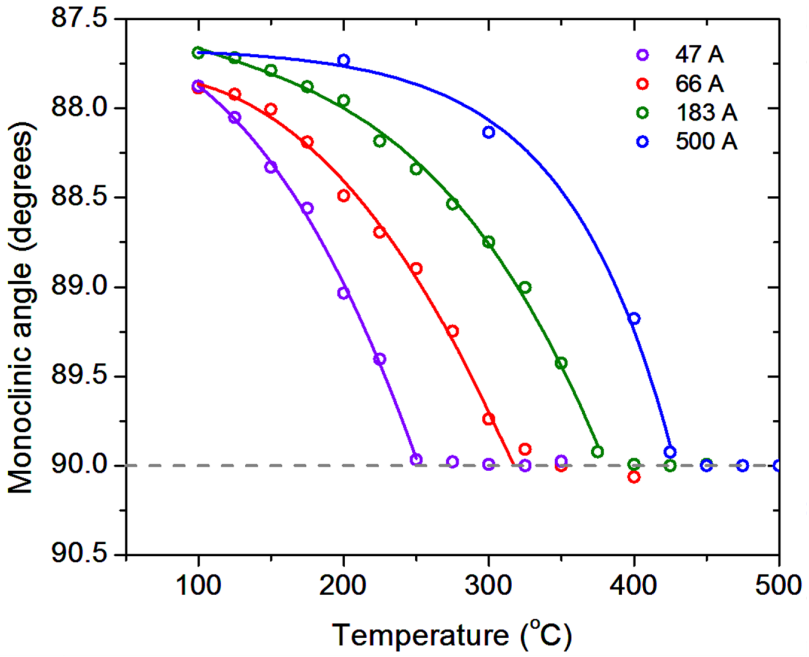


Figure 3.8: Thickness dependence of the structural transition temperature ($M_A$ to T transition) for $BiFeO_3$ films grown on $LaAlO_3$ substrates. Figure courtesy of Dr. Hans M. Christen and Dr. Wolter Siemons, Oak Ridge National Laboratory [73], reprinted with permission.

epitaxial strain can induce the structural phase transition, can a similar transition be obtained by making the film thinner so that the epitaxial strain becomes effective throughout the entire film?

Previous studies [68–70] have shown that the effects of the perovskite heterointerfaces generally extend over only a few unit cells. In particular, ultra-thin $BiFeO_3$ films grown on (001) $SrTiO_3$ substrates with a $SrRuO_3$ buffer layer showed evidence for a transition to tetragonal symmetry [59, 71, 72]. Moreover, for $BiFeO_3$ films grown on (001) $LaAlO_3$ substrates, it has been found that the transition temperature for $M_A$ to T decrease as the film thickness decreases, and films with thickness between 3 nm and 7 nm demonstrated the $M_A$ structure at room temperature (Figure 3.8) [73].

Therefore, two main motivations exist for the $BiFeO_3$ thin film study in this dissertation: 1) How do the boundary conditions and the corner-connected oxygen octahedra network at the film-substrate interface affect the symmetry of the $BiFeO_3$ films grown on $SrTiO_3$ substrates, especially for ultra-thin films? 2) For $BiFeO_3$ films grown on $LaAlO_3$ films, does the room temperature $M_A$ symmetry observed in thinner films still follow a similar $M_C$-$M_A$-T sequence of transitions, or is it a new phase? And can a true tetragonal symmetry be stabilized if the film becomes even thinner than 3

nm?

In Chapter VI, these questions will be addressed via 3D-RSM experiments on ultra-thin $BiFeO_3$ films at different temperatures. A correct determination and deeper understanding of the ultra-thin regime of the $BiFeO_3$ film structure is critical in the sense that the multiferroic and electronic properties depend strongly on the film heteroepitaxy. Most importantly, this is essential for many innovative applications of multiferroics such as low-power electronics and energy storage.

The work on $BiFeO_3$ films grown on $SrTiO_3$ substrates summarized here is published in a paper accepted in *APL Mater.* [60].

### 3.2.3 Sample Preparation

#### 3.2.3.1 $BiFeO_3$ Films Grown on (001) $SrTiO_3$ Substrates

The studies on $BiFeO_3$ films grown on (001) $SrTiO_3$ substrates were performed in collaboration with Professor Darrell Schlom's group at Cornell University, and all the samples were prepared at Cornell. The $BiFeO_3$ thin films with three thicknesses [10 unit cells (UC), 20 UC, and 50 UC films, where 1 UC $\sim$ 0.4 nm] were grown by Dr. Carolina Adamo using reactive molecular-beam epitaxy (MBE) on (001) $SrTiO_3$ substrates (miscut $< 0.1°$) in an adsorption-controlled regime [74] utilizing distilled ozone [75].

#### 3.2.3.2 $BiFeO_3$ Films Grown on (001) $LaAlO_3$ Substrates

The structural investigation on $BiFeO_3$ films grown on (001) $LaAlO_3$ substrates has been carried out in collaboration with Dr. Hans M. Christen's group at Oak Ridge National Laboratory, and all these samples were prepared at Oak Ridge. A detailed description of the growth procedure can be found in [66]. The $BiFeO_3$ thin films with 2 nm, 4 nm, 5 nm, and 20 nm thicknesses were grown by Dr. Christianne Beekman and Dr. Wolter Siemons with pulsed laser deposition (PLD) on (001) $LaAlO_3$ substrates. A base pressure of $5\times10^{-7}$ Torr was maintained with a 25 mTorr oxygen background pressure. The substrate was held at 675 °C during the deposition. A focused KrF excimer laser (wavelength: 248 nm) with an energy density of 0.4 J/cm$^2$ was targeting a 10% excess Bi $BiFeO_3$ sintered pellet. The films were grown with a 0.03 Å/pls average deposition rate at a laser repetition rate of 2 Hz.

# Bibliography


[1] N. Padmavathy and R. Vijayaraghavan, "Enhanced bioactivity of ZnO nanoparticles—an antimicrobial study," *Sci. Technol. Adv. Mater.* **9**, 035004 (2008).

[2] A. Moezzi, A. M. McDonagh, and M. B. Cortie, "Zinc oxide particles: Synthesis, properties and applications," *Chem. Eng. J.* **185-186**, 1 (2012).

[3] C. Wöll, "The chemistry and physics of zinc oxide surfaces," *Prog. Surf. Sci.* **82**, 55 (2007).

[4] Ü. Özhür, Y. I. Alivov, C. Liu, A. Teke, M. A. Reshchikov, S. Doğan, V. Avrutin, S.-J. Cho, and H. Morkoç, "A comprehensive review of ZnO materials and devices," *J. Appl. Phys.* **98**, 041301 (2005).

[5] D. Look, "Recent advances in ZnO materials and devices," *Mater. Sci. Eng.: B* **80**, 383 (2001).

[6] M. W. Allen, M. M. Alkaisi, and S. M. Durbin, "Metal Schottky diodes on Zn-polar and O-polar bulk ZnO," *Appl. Phys. Lett.* **89**, 103520 (2006).

[7] M. W. Allen, S. M. Durbin, and J. B. Metson, "Silver oxide Schottky contacts on n-type ZnO," *Appl. Phys. Lett.* **91**, 053512 (2007).

[8] D. A. Neamen, *Semiconductor physics and devices : basic principles, 2nd ed.* (The McGrew-Hill Companies, Inc., 1997).

[9] B. J. Coppa, C. C. Fulton, S. M. Kiesel, R. F. Davis, C. Pandarinath, J. E. Burnette, R. J. Nemanich, and D. J. Smith, "Structural, microstructural, and electrical properties of gold films and Schottky contacts on remote plasma-cleaned, n-type ZnO (0001) surfaces," *J. Appl. Phys.* **97**, 103517 (2005).

[10] M. W. Allen, R. J. Mendelsberg, R. J. Reeves, and S. M. Durbin, "Oxidized noble metal Schottky contacts to n-type ZnO," *Appl. Phys. Lett.* **94**, 103508 (2009).

[11] R. T. Tung, "Recent advances in Schottky barrier concepts," *Mater. Sci. and Eng.: R* **35**, 1 (2001).

[12] L. J. Brillson and Y. Lu, "ZnO Schottky barriers and Ohmic contacts," *J. Appl. Phys.* **109**, 121301 (2011).

[13] C. Mead, "Surface barriers on ZnSe and ZnO," *Phys. Lett.* **18**, 218 (1965).

[14] K. Ip, B. Gila, A. Onstine, E. Lambers, Y. Heo, K. Baik, D. Norton, S. Pearton, S. Kim, J. LaRoche, and F. Ren, "Effect of ozone cleaning on Pt/Au and W/Pt/Au Schottky contacts to n-type ZnO," *Appl. Surf. Sci.* **236**, 387 (2004).

[15] M. W. Allen and S. M. Durbin, "Influence of oxygen vacancies on Schottky contacts to ZnO," *Appl. Phys. Lett.* **92**, 122110 (2008).

[16] B. J. Coppa, R. F. Davis, and R. J. Nemanich, "Gold Schottky contacts on oxygen plasma-treated, n-type ZnO($000\bar{1}$)," *Appl. Phys. Lett.* **82**, 400 (2003).

[17] S.-H. Kim, H.-K. Kim, and T.-Y. Seong, "Effect of hydrogen peroxide treatment on the characteristics of Pt Schottky contact on n-type ZnO," *Appl. Phys. Lett.* **86**, 112101 (2005).

[18] M. W. Allen, P. Miller, J. B. Metson, R. J. Reeves, M. M. Alkaisi, and S. M. Durbin, "Schottky Contact Behaviour as a Function of Metal and ZnO Surface Polarity," *Mater. Res. Soc. Symp. Proc.* **0957**, K09-03 (2006).

[19] H. Sheng, S. Muthukumar, N. W. Emanetoglu, and Y. Lu, "Schottky diode with Ag on ($11\bar{2}0$) epitaxial ZnO film," *Appl. Phys. Lett.* **80**, 2132 (2002).

[20] U. Grossner, S. Gabrielsen, T. M. Børseth, J. Grillenberger, A. Y. Kuznetsov, and B. G. Svensson, "Palladium Schottky barrier contacts to hydrothermally grown n-ZnOand shallow electron states," *Appl. Phys. Lett.* **85**, 2259 (2004).

[21] H. von Wenckstern, G. Biehne, R. A. Rahman, H. Hochmuth, M. Lorenz, and M. Grundmann, "Mean barrier height of Pd Schottky contacts on ZnO thin films," *Appl. Phys. Lett.* **88**, 092102 (2006).

[22] L. J. Brillson, H. L. Mosbacker, M. J. Hetzer, Y. Strzhemechny, G. H. Jessen, D. C. Look, G. Cantwell, J. Zhang, and J. J. Song, "Dominant effect of near-interface native point defects on ZnO Schottky barriers," *Appl. Phys. Lett.* **90**, 102116 (2007).

[23] H. Endo, M. Sugibuchi, K. Takahashi, S. Goto, S. Sugimura, K. Hane, and Y. Kashiwaba, "Schottky ultraviolet photodiode using a ZnO hydrothermally grown single crystal substrate," *Appl. Phys. Lett.* **90**, 121906 (2007).

[24] S. Liang, H. Sheng, Y. Liu, Z. Huo, Y. Lu, and H. Shen, "ZnO Schottky ultraviolet photodetectors," *J. Cryst. Growth* **225**, 110 (2001), proceedings of the 12th American Conference on Crystal Growth and Epitaxy.

[25] A. Wander, F. Schedin, P. Steadman, A. Norris, R. Mcgrath, T. Turner, G. Thornton, and N. Harrison, "Stability of Polar Oxide Surfaces," *Phys. Rev. Lett.* **86**, 3811 (2001).

[26] O. Dulub, U. Diebold, and G. Kresse, "Novel Stabilization Mechanism on Polar Surfaces: ZnO(0001)-Zn," *Phys. Rev. Lett.* **90**, 016102 (2003).

[27] M. Valtiner, X. Torrelles, A. Pareek, S. Borodin, H. Gies, and G. Grundmeier, "In Situ Study of the Polar ZnO(0001)–Zn Surface in Alkaline Electrolytes," *J. Phys. Chem. C* **114**, 15440 (2010).

[28] M. Valtiner, M. Todorova, G. Grundmeier, and J. Neugebauer, "Temperature Stabilized Surface Reconstructions at Polar ZnO (0001)," *Phys. Rev. Lett.* **103**, 065502 (2009).

[29] M. Valtiner, M. Todorova, and J. Neugebauer, "Hydrogen adsorption on polar ZnO (0001)-Zn: Extending equilibrium surface phase diagrams to kinetically stabilized structures," *Phys. Rev. B* **82**, 165418 (2010).

[30] S. King, S. Parihar, K. Pradhan, H. Johnson-Steigelman, and P. Lyman, "Observation of a $(\sqrt{3} \times \sqrt{3})R30°$ reconstruction on O-polar ZnO surfaces," *Surf. Sci.* **602**, L131 (2008).

[31] O. Dulub, L. A. Boatner, and U. Diebold, "STM study of the geometric and electronic structure of ZnO (0001)-Zn, $(000\bar{1})$-O, $(10\bar{1}0)$, and $(11\bar{2}0)$ surfaces," *Surf. Sci.* **519**, 201 (2002).

[32] N. Jedrecy, S. Gallini, M. Sauvage-Simkin, and R. Pinchaux, "Copper growth on the O-terminated ZnO$(000\bar{1})$ surface: Structure and morphology," *Phys. Rev. B* **64**, 085424 (2001).

[33] N. Jedrecy, S. Gallini, M. Sauvage-Simkin, and R. Pinchaux, "The ZnO non-polar $(10\bar{1}0)$ surface: an X-ray structural investigation," *Surf. Sci.* **460**, 136 (2000).

[34] G. Kresse, O. Dulub, and U. Diebold, "Competing stabilization mechanism for the polar ZnO(0001)-Zn surface," *Phys. Rev. B* **68**, 245409 (2003).

[35] M. Kunat, S. Gil Girol, T. Becker, U. Burghaus, and C. Wöll, "Stability of the polar surfaces of ZnO: A reinvestigation using He-atom scattering," *Phys. Rev. B* **66**, 081402 (2002).

[36] R. Lindsay, C. A. Muryn, E. Michelangeli, and G. Thornton, "ZnO$(000\bar{1})$-O surface structure: hydrogen-free (1×1) termination," *Surf. Sci.* **565**, L283 (2004).

[37] B. Meyer, "First-principles study of the polar O-terminated ZnO surface in thermodynamic equilibrium with oxygen and hydrogen," *Phys. Rev. B* **69**, 045416 (2004).

[38] M. W. Allen, D. Y. Zemlyanov, G. I. N. Waterhouse, J. B. Metson, T. D. Veal, C. F. McConville, and S. M. Durbin, "Polarity effects in the x-ray photoemission of ZnO and other wurtzite semiconductors," *Appl. Phys. Lett.* **98**, 101906 (2011).

[39] J. V. Lauritsen, S. Porsgaard, M. K. Rasmussen, M. C. R. Jensen, R. Bechstein, K. Meinander, B. S. Clausen, S. Helveg, R. Wahl, G. Kresse, and F. Besenbacher, "Stabilization Principles for Polar Surfaces of ZnO," *ACS Nano* **5**, 5987 (2011).

[40] T. M. Parker, N. G. Condon, R. Lindsay, F. M. Leibsle, and G. Thornton, "Imaging the polar $(000\bar{1})$ and non-polar $(10\bar{1}0)$ surfaces of ZnO with STM," *Surf. Sci.* **415**, L1046 (1998).

[41] C. M. Schlepütz, Y. Yang, N. S. Husseini, R. Heinhold, H.-S. Kim, M. W. Allen, S. M. Durbin, and R. Clarke, "The presence of a (1×1) oxygen overlayer on ZnO(0001) surfaces and at Schottky interfaces," *J. Phys.: Condens. Matter* **24**, 095007 (2012).

[42] Y. Yang, C. M. Schlepütz, F. Bellucci, M. W. Allen, S. M. Durbin, and R. Clarke, "Structural investigation of ZnO O-polar $(000\overline{1})$ surfaces and Schottky interfaces," *Surf. Sci.* **610**, 22 (2013).

[43] E. Ohshima, H. Ogino, I. Niikura, K. Maeda, M. Sato, M. Ito, and T. Fukuda, "Growth of the 2-in-size bulk ZnO single crystals by the hydrothermal method," *J. Cryst. Growth* **260**, 166 (2004).

[44] K. Aizu, "Possible Species of Ferromagnetic, Ferroelectric, and Ferroelastic Crystals," *Phys. Rev. B* **2**, 754 (1970).

[45] V. K. Wadhawan, *Introduction to ferroic materials* (Amsterdam: Gordon & Breach, 2000).

[46] N. A. Spaldin and M. Fiebig, "The Renaissance of Magnetoelectric Multiferroics," *Science* **309**, 391 (2005).

[47] K. Wang, J.-M. Liu, and Z. Ren, "Multiferroicity: the coupling between magnetic and polarization orders," *Advances in Physics* **58**, 321 (2009).

[48] E. K. Salje, "Ferroelastic Materials," *Annu. Rev. Mater. Res.* **42**, 265 (2012).

[49] J. Wang, J. B. Neaton, H. Zheng, V. Nagarajan, S. B. Ogale, B. Liu, D. Viehland, V. Vaithyanathan, D. G. Schlom, U. V. Waghmare, N. A. Spaldin, K. M. Rabe, M. Wuttig, and R. Ramesh, "Epitaxial $BiFeO_3$ Multiferroic Thin Film Heterostructures," *Science* **299**, 1719 (2003).

[50] R. J. Zeches, M. D. Rossell, J. X. Zhang, A. J. Hatt, Q. He, C.-H. Yang, A. Kumar, C. H. Wang, A. Melville, C. Adamo, G. Sheng, Y.-H. Chu, J. H. Ihlefeld, R. Erni, C. Ederer, V. Gopalan, L. Q. Chen, D. G. Schlom, N. A. Spaldin, L. W. Martin, and R. Ramesh, "A Strain-Driven Morphotropic Phase Boundary in $BiFeO_3$," *Science* **326**, 977 (2009).

[51] G. Catalan and J. F. Scott, "Physics and Applications of Bismuth Ferrite," *Adv. Mater.* **21**, 2463 (2009).

[52] H. Béa, B. Dupé, S. Fusil, R. Mattana, E. Jacquet, B. Warot-Fonrose, F. Wilhelm, A. Rogalev, S. Petit, V. Cros, A. Anane, F. Petroff, K. Bouzehouane, G. Geneste, B. Dkhil, S. Lisenkov, I. Ponomareva, L. Bellaiche, M. Bibes, and A. Barthélémy, "Evidence for Room-Temperature Multiferroicity in a Compound with a Giant Axial Ratio," *Phys. Rev. Lett.* **102**, 217603 (2009).

[53] A. J. Hatt, N. A. Spaldin, and C. Ederer, "Strain-induced isosymmetric phase transition in $BiFeO_3$," *Phys. Rev. B* **81**, 054109 (2010).

[54] M. B. Holcomb, L. W. Martin, A. Scholl, Q. He, P. Yu, C.-H. Yang, S. Y. Yang, P.-A. Glans, M. Valvidares, M. Huijben, J. B. Kortright, J. Guo, Y.-H. Chu, and R. Ramesh, "Probing the evolution of antiferromagnetism in multiferroics," *Phys. Rev. B* **81**, 134406 (2010).

[55] Z. Chen, Z. Luo, C. Huang, Y. Qi, P. Yang, L. You, C. Hu, T. Wu, J. Wang, C. Gao, T. Sritharan, and L. Chen, "Low-Symmetry Monoclinic Phases and Polarization Rotation Path Mediated by Epitaxial Strain in Multiferroic $BiFeO_3$ Thin Films," *Adv. Funct. Mater.* **21**, 133 (2011).

[56] H. Christen, J. Nam, H. Kim, A. Hatt, and N. Spaldin, "Stress-induced R-$M_A$-$M_C$-T symmetry changes in $BiFeO_3$ films," *Phys. Rev. B* **83**, 144107 (2011).

[57] F. Johann, A. Morelli, D. Biggemann, M. Arredondo, and I. Vrejoiu, "Epitaxial strain and electric boundary condition effects on the structural and ferroelectric properties of $BiFeO_3$ films," *Phys. Rev. B* **84**, 094105 (2011).

[58] J. M. Rondinelli, S. J. May, and J. W. Freeland, "Control of octahedral connectivity in perovskite oxide heterostructures: An emerging route to multifunctional materials discovery," *Mater. Res. Soc. Bull.* **37**, 261 (2012).

[59] C. J. M. Daumont, S. Farokhipoor, A. Ferri, J. C. Wojdeł, J. Íñiguez, B. J. Kooi, and B. Noheda, "Tuning the atomic and domain structure of epitaxial films of multiferroic $BiFeO_3$," *Phys. Rev. B* **81**, 144115 (2010).

[60] Y. Yang, C. M. Schlepütz, C. Adamo, D. G. Schlom, and R. Clarke, "Untilting $BiFeO_3$: The influence of substrate boundary conditions in ultra-thin $BiFeO_3$ on $SrTiO_3$," *APL Mater.* **1**, 052102 (2013).

[61] A. M. Glazer, "Simple ways of determining perovskite structures," *Acta Crystallogr. A* **31**, 756 (1975).

[62] F. Kubel and H. Schmid, "Structure of a ferroelectric and ferroelastic monodomain crystal of the perovskite $BiFeO_3$," *Acta Crystallogr. B* **46**, 698 (1990).

[63] S. V. Kiselev, R. P. Ozerov, and G. S. Zhdanov, "Detection of magnetic order in ferroelectric $BiFeO_3$ by neutron diffraction," *Sov. Phys. Dokl.* **7**, 742 (1963).

[64] D. Vanderbilt and M. H. Cohen, "Monoclinic and triclinic phases in higher-order Devonshire theory," *Phys. Rev. B* **63**, 094108 (2001).

[65] G. Xu, H. Hiraka, G. Shirane, J. Li, J. Wang, and D. Viehland, "Low symmetry phase in (001) $BiFeO_3$ epitaxial constrained thin films," *Appl. Phys. Lett.* **86**, 182905 (2005).

[66] C. Beekman, W. Siemons, T. Z. Ward, M. Chi, J. Howe, M. D. Biegalski, N. Balke, P. Maksymovych, A. K. Farrar, J. B. Romero, P. Gao, X. Q. Pan, D. A. Tenne, and H. M. Christen, "Phase Transitions, Phase Coexistence, and Piezoelectric Switching Behavior in Highly Strained $BiFeO_3$ Films," *Adv. Mater.* **25**, 5561 (2013).

[67] H. Toupet, F. Le Marrec, C. Lichtensteiger, B. Dkhil, and M. G. Karkut, "Evidence for a first-order transition from monoclinic $\alpha$ to monoclinic $\beta$ phase in $BiFeO_3$ thin films," *Phys. Rev. B* **81**, 140101 (2010).

[68] A. Y. Borisevich, H. J. Chang, M. Huijben, M. P. Oxley, S. Okamoto, M. K. Niranjan, J. D. Burton, E. Y. Tsymbal, Y. H. Chu, P. Yu, R. Ramesh, S. V. Kalinin, and S. J. Pennycook, "Suppression of Octahedral Tilts and Associated Changes in Electronic Properties at Epitaxial Oxide Heterostructure Interfaces," *Phys. Rev. Lett.* **105**, 087204 (2010).

[69] S. H. Chang, Y. J. Chang, S. Y. Jang, D. W. Jeong, C. U. Jung, Y.-J. Kim, J.-S. Chung, and T. W. Noh, "Thickness-dependent structural phase transition of strained $SrRuO_3$ ultrathin films: The role of octahedral tilt," *Phys. Rev. B* **84**, 104101 (2011).

[70] J. M. Rondinelli and N. A. Spaldin, "Substrate coherency driven octahedral rotations in perovskite oxide films," *Phys. Rev. B* **82**, 113402 (2010).

[71] K. Saito, A. Ulyanenkov, V. Grossmann, H. Ress, L. Bruegemann, H. Ohta, T. Kurosawa, S. Ueki, and H. Funakubo, "Structural Characterization of $BiFeO_3$ Thin Films by Reciprocal Space Mapping," *Jpn. J. Appl. Phys.* **45**, 7311 (2006).

[72] Y. H. Chu, M. P. Cruz, C. H. Yang, L. W. Martin, P. L. Yang, J. X. Zhang, K. Lee, P. Yu, L. Q. Chen, and R. Ramesh, "Domain Control in Multiferroic $BiFeO_3$ through Substrate Vicinality," *Adv. Mater.* **19**, 2662 (2007).

[73] W. Siemons, C. Beekman, and H. M. Christen, Private communication.

[74] J. F. Ihlefeld, N. J. Podraza, Z. K. Liu, R. C. Rai, X. Xu, T. Heeg, Y. B. Chen, J. Li, R. W. Collins, J. L. Musfeldt, X. Q. Pan, J. Schubert, R. Ramesh, and D. G. Schlom, "Optical band gap of $BiFeO_3$ grown by molecular-beam epitaxy," *Appl. Phys. Lett.* **92**, 142908 (2008).

[75] C. T. Nelson, B. Winchester, Y. Zhang, S.-J. Kim, A. Melville, C. Adamo, C. M. Folkman, S.-H. Baek, C.-B. Eom, D. G. Schlom, L.-Q. Chen, and X. Pan, "Spontaneous Vortex Nanodomain Arrays at Ferroelectric Heterointerfaces," *Nano Lett.* **11**, 828 (2011).

# CHAPTER IV

# Experimental Setup and Analysis Methods

## 4.1 Introduction

In this chapter, the experimental setup used for synchrotron x-ray scattering data acquisition and the analysis methods for the acquired data will be introduced. After starting with a brief overview of the synchrotron x-ray source and beamline optics, the methods used for mounting and aligning the samples will be described. This is followed by an account of the data acquisition techniques for SXRD and 3D-RSMs. The post-experiment data processing procedure will be briefly discussed, and the SXRD model fitting method utilizing genetic algorithms will be introduced. Finally, details about 3D-RSM reconstruction from area detector measurements will be described.

## 4.2 Experimental Setup

### 4.2.1 Synchrotron X-ray Sources and Beamlines

Modern synchrotron facilities usually consist of five main components: the linear accelerator, the booster synchrotron, the electron storage ring, insertion devices (or bending magnets), and beamlines (experimental hall) [1, 2]. Figure 4.1 shows the schematic of a typical synchrotron facility. The operation of the synchrotron can be summarized as follows [1, 2]:

1) Electrons emitted from a hot cathode ($\sim 1100\,^{\circ}\mathrm{C}$) enter into a linear accelerator. By high-voltage alternating electric field, the electrons are accelerated to hundreds of millions of electron volts energy by sequential high-voltage electric fields; at this stage, the electrons are already moving at $> 99\%$ the speed of light.

2) Electrons accelerated by the linear accelerator move into the booster ring. Electric fields in RF cavities boost the electron energy from hundreds of MeV to a

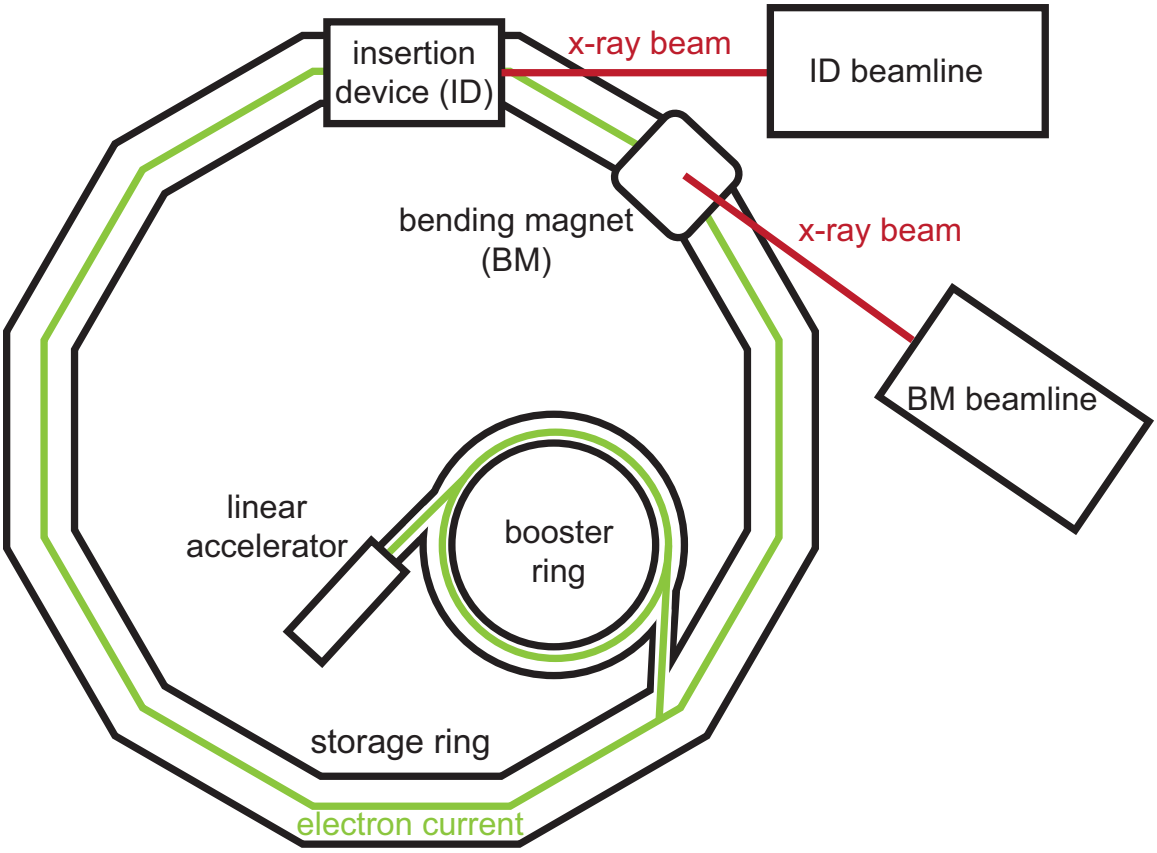


Figure 4.1: Brief schematic of a third-generation synchrotron facility.

few GeV, resulting in electrons faster than 99.99999% of the speed of light.

3) These highly energetic electrons are now injected into the storage ring. As can be seen in Figure 4.1, the orbital path of the electrons consists of several alternating straight sections and bent sections. Insertion devices (IDs) are placed in the straight sections of the storage ring, and the bent sections are equipped with bending magnets (BMs), which can change the propagation direction of the electrons. The sections with BMs are designed to make the electron path a closed loop around the storage ring.

4) Very strong electromagnetic radiation can be obtained from the straight sections with IDs. Insertion devices are made of two arrays of strong permanent magnets with alternating N and S poles in each array [Figure 4.2 (a)]. At the straight section of the storage ring, the IDs are placed so that the electron path lies between these two magnet arrays. The electrons feel rapid accelerations due to the magnets, and the actual path of the electron becomes wavy rather than straight [see Figure 4.2 (b)], resulting in intense electromagnetic radiation with minimized divergence. Bending magnets also accelerate the storage ring electrons by changing their directions, and

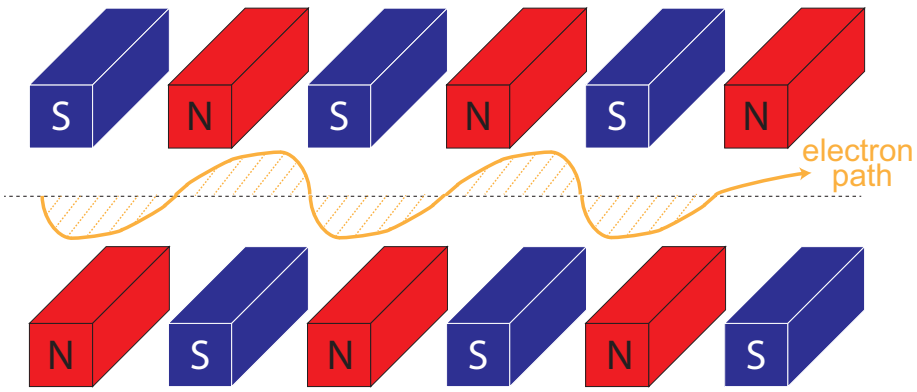


Figure 4.2: Schematic of an insertion device: two arrays of magnets with alternating N and S poles, and the corresponding path of the storage ring electrons.

therefore produce electromagnetic radiation. Although the BM radiation is more divergent and less intense compared to the ID radiation, the BM still delivers orders of magnitude higher x-ray intensities compared to conventional lab sources such as x-ray tubes.

5) The electromagnetic radiation generated from IDs or BMs is delivered to corresponding beamlines. Depending on the specific purpose of each beamline (imaging, scattering, spectroscopy, etc.), the beamline optics setup varies significantly from one beamline to another. Figure 4.3 shows a typical optics setup for monochromatic x-ray diffraction beamlines.

The strong polychromatic radiation generated from an ID or a BM first goes through beam-defining slits and/or apertures and enters into the mirror/monochromator system. Since the real part of the index of refraction of typical solid materials at x-ray energies is slightly less than unity, total external reflection occurs when the incidence angle is less than the critical angle. The critical angle is usually on the order of $10^{-1}$ degrees, and the value depends on the index of refraction of the material and the x-ray wavelength. Therefore, different materials are used as x-ray mirrors for different x-ray wavelengths. Nowadays, x-ray mirrors are designed in such a way that the mirror can be bent or twisted by applying different forces on the corners of the mirror. Therefore, well-focused and collimated x-ray beams can be obtained by carefully adjusting the curvature of the mirrors.

For atomic-scale structural studies, the scattering experiments are performed with hard x-rays (wavelength $<$ 6 Å). To obtain monochromatic hard x-rays, crystal monochromators are typically employed. Using Bragg's law, $n\lambda = 2d\sin\theta$, with a fixed crystallographic layer spacing $d$ of the monochromator, the peak x-ray wave-

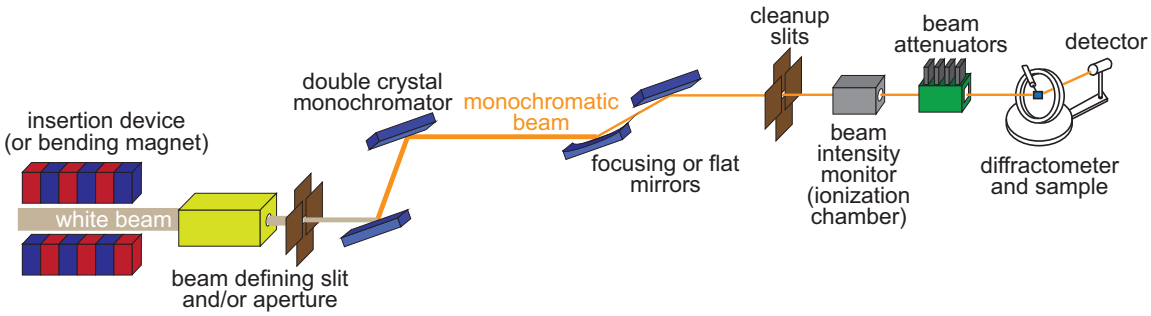


Figure 4.3: Schematic of monochromatic x-ray scattering beamline optics.

length $\lambda$ can be tuned by adjusting the x-ray incidence angle $\theta$ on the monochromator. The monochromatized beam, however, can contain not only the fundamental wavelength ($\lambda_0$: the wavelength that satisfies Bragg's equation with $n$=1) but also higher harmonic contamination ($n$=2 or higher). This is because the Bragg equation can also be satisfied with the identical lattice spacing ($d$) and angle ($\theta$) for $n = 2$ and $\lambda = \lambda_0/2$, and similarly for higher $n$. These unwanted higher energy photons can be successfully rejected using additional mirrors. Since the critical angle of x-rays for the same material decreases as the x-ray energy increases, the proper choice of mirror material and mirror angle would allow total external reflection only for those photons with the fundamental wavelength, but not for higher harmonics.

### 4.2.2 Sample Alignment for Diffraction Experiments

After going through all the beamline optics including monochromators, mirrors, and slits, a properly shaped and well-focused beam can be obtained. The beam and diffractometer positions are adjusted such that the beam goes through the origin of all diffractometer axes, and the beam propagation direction is parallel to the diffractometer $y$ axis (in the diffractometer axes convention of Figure 4.4).

The experimental data in this dissertation were measured at Sectors 13-BM-C, 13-ID-C, 33-BM-C, and 33-ID-D at the Advanced Photon Source, Argonne National Laboratory, USA, and beamline X04SA at Swiss Light Source, Paul Scherrer Institute, Switzerland. Sectors 13-BM-C, 13-ID-C, and 33-ID-D are equipped with Newport 6-circle diffractometers using a kappa geometry [3], and 33-BM-C is equipped with a Huber 4-circle diffractometer with a Eulerian geometry [4]. Sector X04SA uses a (2+3) circle Newport diffractometer and a hexapod [5].

The investigated samples typically have a surface area of 5×5 to 10×10 mm$^2$, with 0.5 to 1 mm thickness. The samples are mounted on the diffractometer using brass pins glued to the back side of the sample with beeswax. At the zero position

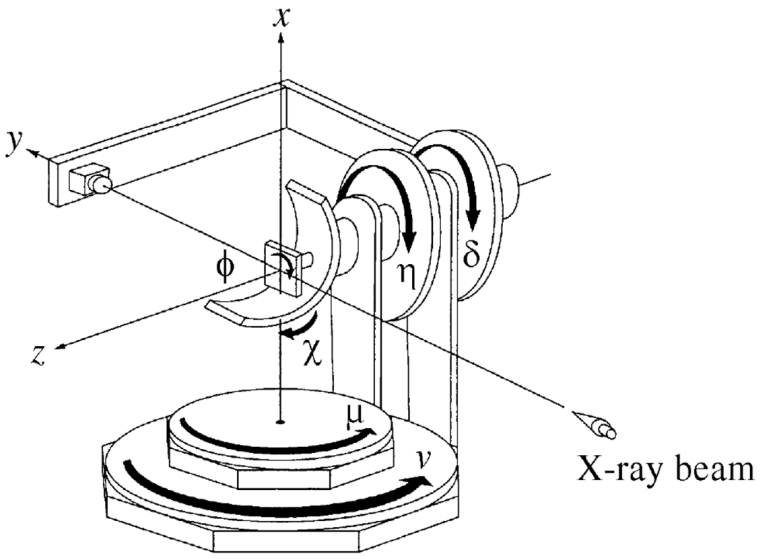


Figure 4.4: Typical 6-circle diffractometer axes with all at the zero positions. Reprinted from [3] with permission (© 1999, International Union of Crystallography).

of the diffractometer (Figure 4.4), the optical surface of the sample can be aligned perpendicular to the $z$ axis of the diffractometer using a laser reflection. While shining a laser beam on the sample surface, the rotation stage of the goniometer head or chi and phi angles (when using 6-circle diffractometer) can be adjusted until the laser reflection is stationary during a 180° rotation of the sample around the $z$ axis.

Once the sample surface is aligned, the sample is placed at the diffractometer center using sample translation stages. Nowadays, most beamlines use cameras for monitoring the diffractometer and sample positions during the experiment. The diffractometer center position can be marked on the monitor screen, so that the adjustments for lateral position of the sample can be easily done by just moving the sample to the marked diffractometer center position while monitoring the camera image.

The next step is to adjust the position of the sample carefully with respect to its surface normal direction so that the sample surface is exactly at the diffractometer center. This step is important because diffractometer angle calculations are based on the assumption that the x-ray scattering occurs exactly at the diffractometer center. Note that the laser alignment makes the optical surface of the sample parallel to the x-ray beam propagation direction, and that the x-ray beam is aligned so that the beam goes through the diffractometer center. This means that the sample surface should be cutting the x-ray beam exactly into half when the sample surface is at the diffractometer center. Since the lateral dimensions of the investigated samples

are large enough to completely block the entire x-ray beam, this condition can be achieved by moving the sample in its surface normal direction until exactly half of the initial x-ray beam is transmitted (the other half is blocked by the sample), while monitoring the intensity of the transmitted x-ray beam.

The orientation of the crystallographic axes ($a$, $b$, and $c$ axes) of the sample relative to the diffractometer axes depends on how the sample is mounted on the diffractometer. The next step is finding the orientation of the sample axes, i.e., finding the *orientation matrix*. A typical procedure for obtaining orientation matrices of single crystal substrates is described in Appendix A. Once the orientation matrix is obtained, the diffractometer angles can be calculated for any arbitrary reciprocal space position, although there will be inaccessible regions due to the x-ray wavelength or instrumental restrictions.

Most of the user-accessible beamline instruments including x-ray detectors and diffractometers are controlled by a software package called SPEC [6]. All sample alignments and measurements are performed using SPEC, which is widely used at almost every diffraction beamline.

## 4.3 ZnO Measurements and Analysis: SXRD and Model Fitting

As introduced in Chapter III, the atomic structure of ZnO Zn-polar (0001) and O-polar $(000\bar{1})$ surfaces and Schottky interfaces are measured with SXRD. The following sections describe the CTR measurements, the post-beamtime data processing, and the model fitting for the atomic structure determination.

### 4.3.1 CTR Measurements

When calculating the diffractometer angles for a given reciprocal space position in SPEC, it is assumed that a point detector is mounted on the diffractometer arm in a way that the direct x-ray beam hits the point detector when the diffractometer is at its zero position. In this dissertation, a PILATUS 100K area detector [7] is employed for fast and reliable data acquisition [8, 9]. In this case, where an area detector is used, the *center pixel* is defined as a reference point where the direct x-ray beam hits when the diffractometer is at its zero position. Therefore, the calculated diffractometer angles would bring this center pixel to the desired reciprocal space position.

As described in Chapter II, the existence of a well-defined surface produces diffraction intensities, i.e., CTRs, at integer H and K with non-integer (continuous) L positions in reciprocal space. Therefore, CTR datasets can be obtained by scanning along the L direction at fixed H and K for all accessible integer H and K. Ideally, the CTR signals show up at the center pixel of the detector. In reality, instrumental misalignments or sample miscuts may tilt the CTRs slightly from the L direction, and the signals will be slightly off from the center pixel in these cases.

Since ZnO surfaces exhibit a *p6mm* symmetry, measuring CTRs in 1/12 of the HK reciprocal space plane determines the entire diffraction pattern through the 6-fold symmetry operations. During the experiments, 1/12 of the HK plane plus several equivalent CTRs are recorded (1) to double check the symmetry, and (2) to obtain the statistical errors from symmetry averaging.

Either a 4-circle or a 6-circle diffractometer is used for the diffraction experiments in this study. Since only three diffractometer axes are needed to determine the reciprocal space position (HKL), there is one redundant degree of freedom for calculating diffractometer angles in case of 4-circle diffractometers and three redundancies for 6-circle diffractometers. Therefore, there should be some constraints to reduce the diffractometer degrees of freedom and determine a unique solution for the diffractometer angles for a given HKL position.

For determining the appropriate diffractometer constraints for CTR measurements, one geometrical aspect is important: the *active area*. During the CTR measurement, the x-ray beam is projected onto the sample surface with a certain size and shape, depending on the orientation of the sample surface with respect to the incident x-ray beam. This area of the projected x-ray beam on the sample surface is called the *active area*. Since only the sample surface within the active area contributes to the x-ray scattering, different diffraction intensities will be observed even for the same reciprocal space point if the diffraction conditions are achieved by two different diffractometer geometries with different active areas. To prevent inconsistencies due to a changing active area during the CTR measurements, a 'fixed incident angle to the sample surface' constraint is usually employed. For a symmetrically shaped incident x-ray beams, fixing the incident angle allows the shape and size of the projected x-ray beam to be consistent throughout the measurement. In case of using a 6-circle diffractometer, the diffractometer axes for a given sample position can be totally fixed except for rotation around the sample normal direction. This will keep the shape of the projected beam fully consistent regardless of the shape of the incident beam unless the projected x-ray beam is larger than the sample due to a very low incident

angle.

### 4.3.2 Post-Beamtime SXRD Data Processing

All post-beamtime data processing in this section is performed based on the procedure described in a Ph.D. thesis by Dr. Christian M. Schlepütz [10]. The procedure is only briefly introduced here, but more details can be found in [10].

The raw detector images taken during the beamtime contain background scattering and other unwanted signals (tails of substrate Bragg peaks, powder rings from polycrystalline metal contacts, etc.) as well as the desired CTR signal. Also, the x-ray counting response of each pixel in the detector is slightly different from pixel to pixel. Signals close to the substrate Bragg peaks are sometimes very intense and reducing the incident x-ray flux is necessary to prevent the saturation of the detector. In this case, the measured intensities must be corrected with the beam attenuation ratio. When the synchrotron is in non-topup mode operation, the electron current in the storage ring will decay as a function of time, and the incident x-ray beam intensity will vary accordingly. Beamlines are equipped with ionization chambers to monitor the incident x-ray flux during the experiment to provide correction factors for this issue. Considering all these factors, post-beamtime data processing is necessary in order to properly extract the CTR signals from the raw detector images and apply corrections to minimize any inconsistencies in the dataset.

The inhomogeneous pixel responses can be corrected by taking a flat-field calibration of the detector. Using an amorphous scatterer (glass slides or Kapton foil), the detector can be exposed to uniform x-ray intensity across the entire detector. This uniform intensity should be measured for a long enough time to obtain sufficient counting statistics for each pixel. Based on the statistics, the counting response of each pixel can be calibrated.

After flat-field analysis, the CTR signals are extracted from the raw image using a MATLAB based software *Scananalysis* developed by Dr. Christian M. Schlepütz. Figure 4.5 shows the typical data extraction window of *Scananalysis*. The raw detector image is displayed in the main panel (left), the white loop around the CTR signal is called *signal region of interest (ROI)*, and the red loop around the signal ROI is called *background ROI*. When these ROIs are defined, the software integrates the photon counts of the pixels inside the signal ROI, and fits a background function using the values in those pixels that are within background ROI but not part of the signal ROI. The background data in the background ROI and fit function to the background are plotted in upper right panel, so the shape of the background fit

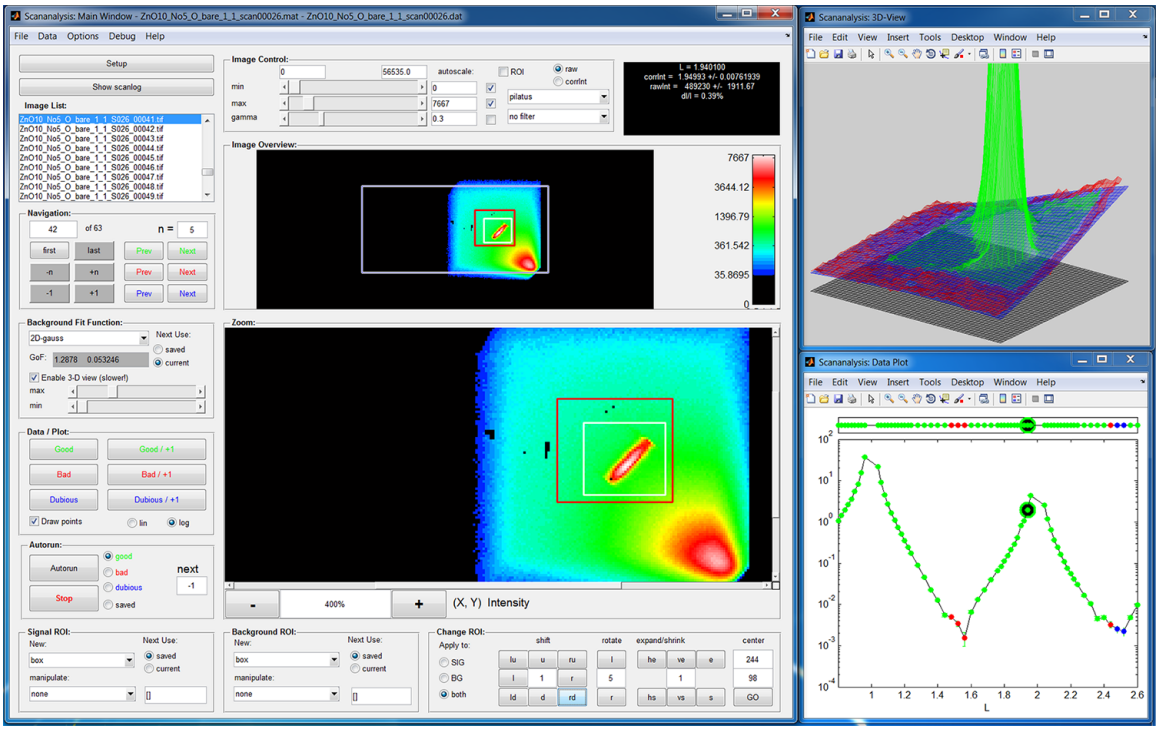


Figure 4.5: Typical CTR data processing window of *Scananalysis*.

can be checked from the plot. Unfortunately, there is no easy way of automating the selection of ROIs and the choice of a background function, and every detector image must be processed manually. The *Scananalysis* software is designed to simultaneously process the flat-field data, raw images, and datafile which contains the attenuator and monitor count information during the scan. Therefore, flat-field, attenuator and monitor corrections are automatically applied during the ROI selection and background fitting procedure.

As described in Chapter II, the diffraction intensity is dependent on the angle between the polarization direction of the incident x-ray beam and the direction of the scattered wave. If the angle between those two directions is smaller than 90°, there will be a loss of diffraction intensity due to the polarization. Most of the synchrotron x-rays are horizontally polarized (parallel to the lab floor—$yz$ plane in Figure 4.4), and therefore a vertical scattering plane geometry (both incident and scattered wavevectors are in vertical plane—$xy$ plane in Figure 4.4) is preferred to minimize the loss of diffraction intensity. In some cases, however, a non-vertical scattering geometry is necessary due to other geometric restrictions such as limited diffractometer motion or the need to maintain a constant x-ray incident angle on the sample surface. Since the direction of the incident x-ray beam is fixed, the polarization

correction factors depend only on the direction of scattered wavevector, which can be calculated from the angular positions of the detector.

Another important correction factor is the *Lorentz factor*. In a theoretical formulation, it is assumed that the x-ray source is perfectly monchromatic and the CTR intensities are nonzero only if H and K are exactly integers (i.e., $\delta$ functions in HK-plane). In reality, the x-ray source has a finite energy bandwidth, and also the CTRs have a finite extent. Therefore, during the experiment, the CTR can be observed over a finite angular range, rather than at a delta function in position. Since the positions in the reciprocal lattice are not linearly related to the angular motions of diffractometer angles, the same angular range may cover different ranges in reciprocal space, depending on the corresponding position in reciprocal space. This issue can be corrected by the Lorentz factor, which, in general, can be calculated from the determinant of the Jacobian matrix for the coordinate transformation between the diffractometer angles and reciprocal space. In this study, all sample surfaces are co-planar with their HK plane of the reciprocal space. In this case, the Lorentz factor can be simply calculated as $\sin(\beta_{out})$, where $\beta_{out}$ is the angle between the scattered wavevector and the sample surface [10].

Lastly, the CTR data should be corrected with the active area during the measurement. As discussed above, the deviation in active area can be minimized by running the experiment with a 'fixed incident angle' constraint. Note, however, that the specular (00L) rod cannot be measured with a fixed incident angle, and low x-ray incident angle experiments on small samples can result in beam spillage, which can significantly change the active area depending on the azimuthal rotation of the sample even when using a fixed incident angle. In these cases, the active area of the sample surface can be simulated from the diffractometer positions based on the measured shape of the incident beam and the shape of the sample at the diffractometer zero position.

### 4.3.3 Model Fitting with a Genetic Algorithm

The atomic structure of a crystal surface can be determined from the measured CTRs, using a model fitting process. The surface structure can be modeled with several free parameters, such as atomic positions and occupation factors of the surface atoms, and the CTR intensities can be simulated from the modeled structure. The discrepancies between the simulated and measured CTR intensities can be measured by a *figure of merit* (FOM) function. Typical FOMs used for SXRD are $\chi^2$,

crystallographic $R$, log, and logarithmic $R$ ($R_{\log}$), which are defined as

$$\chi^2 = \frac{1}{N-1}\sum_i \left|\frac{E_i^{\exp} - E_i^{\sim}}{E_i^{\exp}}\right|^2 \tag{4.1}$$

$$R = \frac{\sum_i \left||E_i^{\exp}| - |E_i^{\sim}|\right|}{\sum_i |E_i^{\exp}|} \tag{4.2}$$

$$\log = \frac{1}{N-1}\sum_i \left|\log_{10}(|E_i^{\exp}|) - \log_{10}(|E_i^{\sim}|)\right| \tag{4.3}$$

$$R_{\log} = \frac{\sum_i \left|\log_{10}(|E_i^{\exp}|) - \log_{10}(|E_i^{\sim}|)\right|}{\sum_i \log_{10}(|E_i^{\exp}|)}, \tag{4.4}$$

where N denotes the total number of datapoints in a dataset, $E_i^{\exp}$ are the measured intensities, and $E_i^{\sim}$ are the simulated intensities using a given model and a corresponding set of parameters. A smaller FOM value indicates a better agreement between the measured and simulated CTRs, and the goal of the fitting is to find a model and a parameter set with the lowest FOM.

One of the widely used algorithms for CTR fitting is the conventional gradient descent algorithm. Figure 4.6 illustrates a typical fit using this algorithm. Consider a parameter space of two variables, as given in Figure 4.6 (a). Starting from an initial guess of the parameters, the parameters are changed in the direction of the steepest descent of the FOM until the gradient becomes zero. With the proper choice of the initial guess, the fitting successfully finds the global minimum of the given parameter space [Figure 4.6 (b)]. For some initial guesses, however, the fitting becomes trapped in local minima and fails to find the global minimum, as can be seen in Figure 4.6 (c).

In case of CTR fitting, which typically involves more than 10 fitting parameters, the parameter space becomes very complicated and many local minima can exist. Because every trial fitting has a significant chance of being trapped in a local minimum, gradient descent algorithms are not reliable in this case. Moreover, the gradient descent method is a deterministic algorithm, which always reproduces the identical result if started with the same initial parameters. Therefore, it is also not possible to check the reliability of the solution by running the same fitting multiple times.

To obtain reliable fitting results, the measured CTRs were fitted using a specialized module to model SXRD data in the structural refinement program *GenX* [11]. *GenX* employs differential evolution algorithms [11–14], which use global search procedures and efficiently avoid becoming trapped in local minima. In addition, differential algorithms are non-deterministic, and every fitting trial leads to different results,

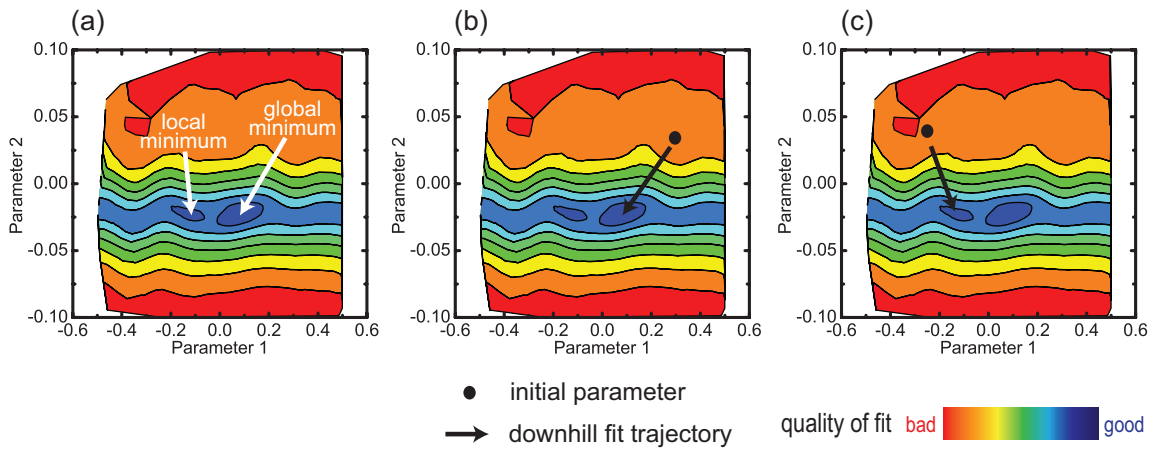


Figure 4.6: Illustration of the gradient descent algorithm. (a) A parameter space with two variable parameters has a local minimum and a global minimum. (b) Staring with a good initial guess, the fitting successfully finds the global minimum. (c) For certain other initial guesses, the fitting can be trapped in a local minimum and it fails to find the global minimum.

even with the identical initial guesses. This allows one to check the reliability of the final result, which can be done by running the same fit several times and verifying that it converges to the same solution every time.

The differential evolution algorithms are based on the fundamental concepts of genetic evolution. Starting from a parent population of individuals, a next generation is formed through a reproduction process that includes the recombination of genetic materials from the parents and random mutations thereof. Those parents with a better fitness for survival have a higher likelyhood of passing their genetic information to the next generation. This concept is generally referred to as the *survival of the fittest*.

In the context of genetic optimization algorithms, these concepts are applied in the following way. The set of fitting parameters corresponds to the set of genes in an individual. The fitness of a particular individual is measured by the FOM value corresponding to its set of parameter values. The differential evolution algorithm starts with a parent population which consists of a number of individuals. The next generation (test population) is then created from the parent population in the way described in Figure 4.7. First, one individual, namely 'selected individual', from the parent population is chosen to evolve into the test population. Next, the 'best individual' with the lowest FOM among the parent population is identified. Then, a vector is generated by taking the difference between two randomly selected individuals from the parent population. This vector is multiplied by a *mutation constant* $k_m$, and

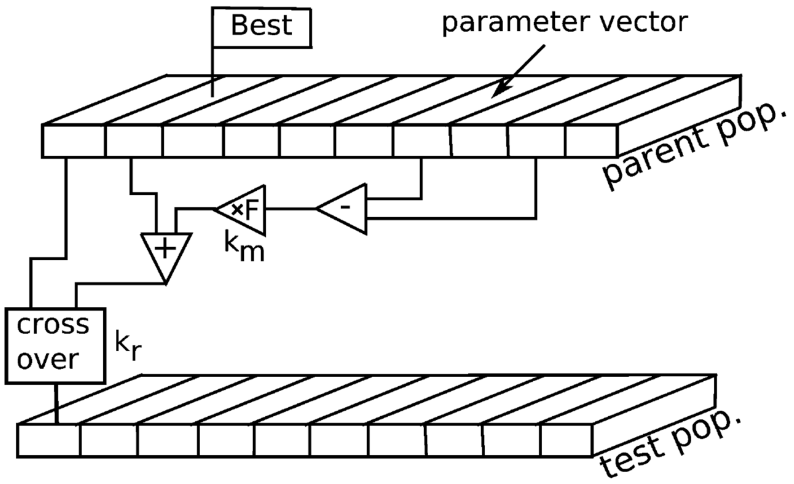


Figure 4.7: The creation of the trial vectors in the differential evolution algorithm. Reprinted from [11] with permission (© 2007, International Union of Crystallography).

added to the best individual to create a 'new vector'. Finally, each parameter in the selected individual will be exchanged for one of the new vector with a probability given by a *recombination constant* $k_r$, to create a new individual in the test population. This process is repeated for every individual in the parent population, which results in a test population with the same number of individuals as the parent population. In the next iteration, this test population becomes a new parent population to create yet a new test population.

Since all the individuals in the test population contain information from the best individual in the parent population, the entire test population tends to move toward the best individual as the fitting continues. During this process, the individuals randomly search the parameter space (the degree of randomness depends on the $k_m$ and $k_r$ values), and this greatly reduces the risk of being trapped in local minima. Figure 4.8 describes the fitting behavior of the differential evolution algorithm. As can be seen in the figure, all the individuals successfully converge into the global minimum.

Since the efficiency of the search behavior strongly depends on the $k_m$ and $k_r$ values, before starting to use genetic algorithms for a system with a given FOM, proper $k_m$ and $k_r$ values should be established. The procedure for determining the control parameters used in this study is described in Appendix B.

The evolution history of individual parameter sets provides correlation information between parameters, which allows for a more precise error bar estimation, even with FOMs other than $\chi^2$ least squares. A detailed description about obtaining proper

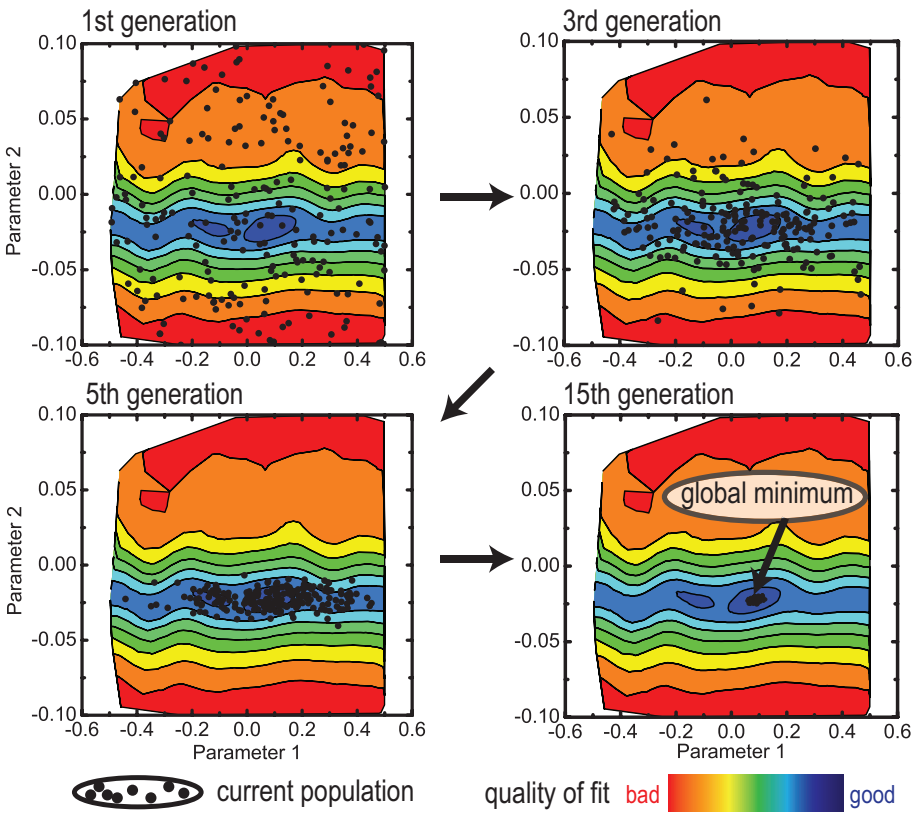


Figure 4.8: Schematic of the search behavior of genetic algorithms. All individuals converge into the global minimum after 15 generations, successfully avoiding the local minimum.

error bars from the fitting history can be found in Appendix C.

## 4.4 $BiFeO_3$ Measurements and Analysis: 3D-RSM

The unit-cell symmetry of a crystal can be determined by studying the symmetry of the diffraction pattern. Unlike a determination of the detailed atomic structure inside the unit cell, which requires a thorough analysis of the diffraction intensities, the unit cell symmetry can be obtained by qualitatively examining the existence of the Bragg peaks and their splitting patterns (see Appendix D). For this purpose, 3D-RSM can be a very important technique, because it allows one to display the diffraction pattern in any direction in 3D reciprocal space. The RSMs can be efficiently measured at synchrotrons, especially with modern pixel area detectors. Since each area detector image represents a two-dimensional slice of reciprocal space, any kind of diffractometer angle scan would contain 3-dimensional information as a set of two-dimensional reciprocal space slices. By virtue of fast gridding algorithms, these can

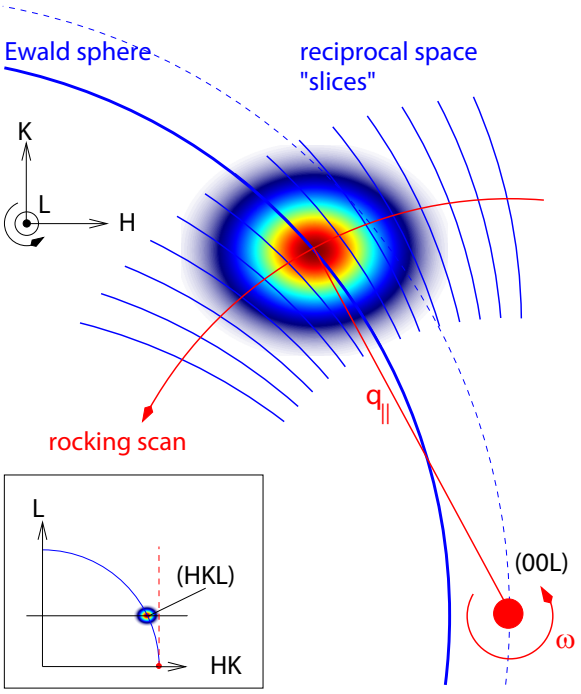


Figure 4.9: The 3-dimensional reciprocal space volume can be sampled by a single rocking scan with a pixel detector, because each detector image is a 2D slice of the reciprocal space. Figure courtesy of Dr. Christian M. Schlepütz, Argonne National Laboratory. Reproduced with permission.

be easily converted to 3D volumes of scattering intensities mapped onto a standard rectangular grid.

### 4.4.1 RSM Measurements

To measure RSMs of $BiFeO_3$ thin films, a PILATUS 100K area detector is employed. The intensity distribution around each peak is measured in a series of single scans along the L-direction, or as rocking scans around the azimuthal rotation axis of the sample surface, or by a combination of these two. Figure 4.9 shows how the 3D-volume in reciprocal space can be sampled during a rocking scan with an area detector. Due to the Lorentz factor issue described in Section 4.3.2, the angular range required for capturing the entire peak splitting pattern is different for each peak, depending on the position of the peak in the reciprocal space. Therefore, the scan range for each peak should be checked before running the scan. Usually, multiple rocking scans with large angular ranges are needed for the peaks with low L indices, whereas single L scans can cover a sufficient angular range for peaks with high L indices.

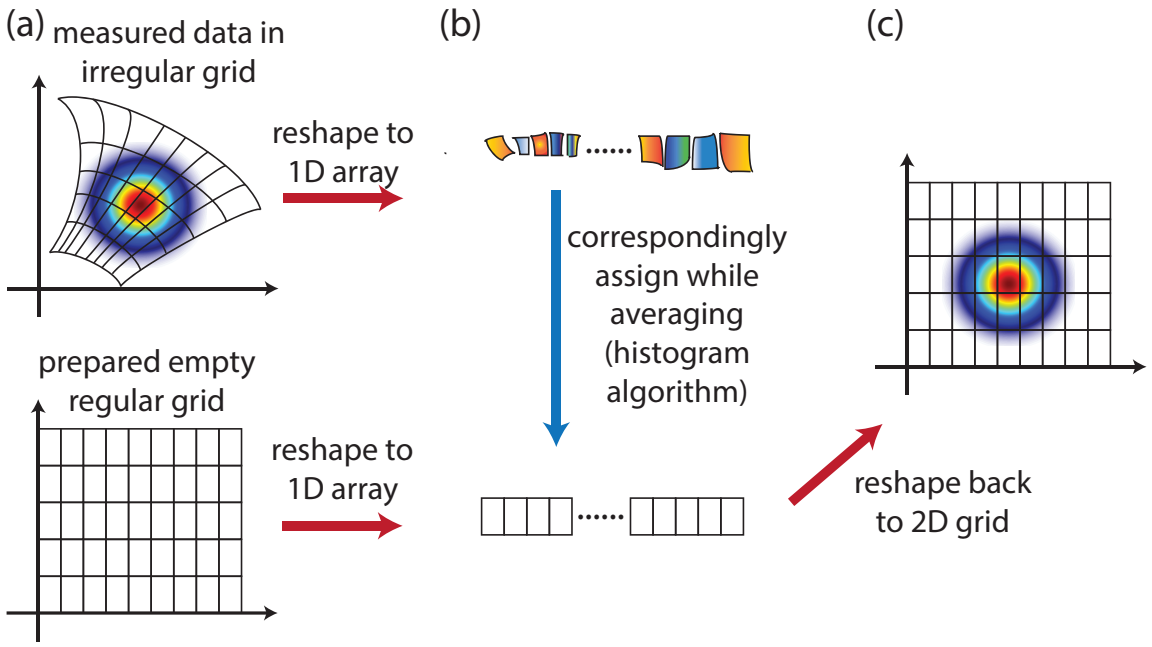


Figure 4.10: Reciprocal space volume reconstruction procedure. This figure describes the reconstruction of a 2D intensity distribution for simplicity, but the actual reconstruction algorithm works similarly for a 3D intensity volume. (a) Measured intensity data on an irregular grid of reciprocal space and an empty rectangular grid. (b) Interpolation procedure using a histogram algorithm. (c) Interpolated intensity data on the regular rectangular grid.

### 4.4.2 Reciprocal Space Volume Reconstruction

During the RSM scan, detector images are recorded together with the corresponding diffractometer positions. The next step is to convert this angle-intensity information to intensities in a 3D reciprocal space volume. Each pixel in the detector corresponds to a unique reciprocal space point, which can be calculated from the angular position of the pixel in diffractometer coordinates. This calculation procedure is well-described in [5].

Again, since the relation between the diffractometer angular space and the reciprocal space is non-linear, the reciprocal space volume obtained from the scan is in an irregular grid, as described in Figure 4.10 (a). This irregular grid is very difficult to handle in standard graphical software such as Origin [15] and MATLAB [16], and should be interpolated to a rectangular grid so that it can be properly displayed as a map.

Dr. Christian M. Schlepütz has developed an efficient algorithm for converting the irregular grid intensity data to regular grid data. This procedure is described

in Figure 4.10. First, an empty rectangular grid, which is slightly larger than the irregular grid, is prepared for storing the intensity data [Figure 4.10 (a)]. The size of each voxel can be arbitrarily determined depending on the desired resolution of the RSM, but the regular grid voxel size should be larger than the largest voxel in the irregular grid (therefore, this determines the maximum resolution of the final RSM) to prevent holes in the reconstructed intensity map. Next, the irregular intensity grid and the regular empty grid are converted to 1D arrays with the proper indices assigned to each array element. Here, the indices are determined such that they represent the reciprocal space positions of the original voxels. Then, using a fast histogram algorithm, the intensity value in each element of the irregular 1D array is assigned to an element of the regular 1D array with the corresponding reciprocal space index. If more than one intensity value falls into a single element of the regular grid, their averaged intensity is used instead [Figure 4.10 (b)]. The desired 3D reciprocal space volume with a regular grid can be finally obtained by just re-shaping the regular 1D array to the original 3D grid size [Figure 4.10 (c)].

## Bibliography


[1] Advanced Photon Source at Argonne National Laboratory, "APS Systems Map," http://www.aps.anl.gov/About/APS_Overview/map.html.

[2] P. Willmott, *An Introduction to Synchrotron Radiation: Techniques and Applications* (John Wiley & Sons, Ltd., 2011).

[3] H. You, "Angle calculations for a '4S+2D' six-circle diffractometer," *J. Appl. Crystallogr.* **32**, 614 (1999).

[4] W. R. Busing and H. A. Levy, "Angle calculations for 3- and 4-circle X-ray and neutron diffractometers," *Acta Crystallogr.* **22**, 457 (1967).

[5] C. M. Schlepütz, S. O. Mariager, S. A. Pauli, R. Feidenhans'l, and P. R. Willmott, "Angle calculations for a (2+3)-type diffractometer: focus on area detectors," *J. Appl. Crystallogr.* **44**, 73 (2011).

[6] Certified Scientific Software, "SPEC," http://www.certif.com/.

[7] DECTRIS®, "PILATUS x-ray pixel detector," https://www.dectris.com/.

[8] C. M. Schlepütz, R. Herger, P. R. Willmott, B. D. Patterson, O. Bunk, C. Brönnimann, B. Henrich, G. Hülsen, and E. F. Eikenberry, "Improved data acquisition in grazing-incidence X-ray scattering experiments using a pixel detector," *Acta Crystallogr. A* **61**, 418 (2005).

[9] P. Kraft, A. Bergamaschi, C. Broennimann, R. Dinapoli, E. F. Eikenberry, B. Henrich, I. Johnson, A. Mozzanica, C. M. Schlepütz, P. R. Willmott, and B. Schmitt, "Performance of single-photon-counting PILATUS detector modules," *J. Synchrotron Rad.* **16**, 368 (2009).

[10] C. M. Schlepütz, *Systematic Structure Investigation of YBCO Thin Films with Direct Methods and Surface X-ray Diffraction*, Ph.D. thesis, Mathematisch-naturwissenschaftliche Fakultät, Universität Zürich (2009), doi: 10.6084/m9.figshare.942424.

[11] M. Björck and G. Andersson, "GenX: an extensible X-ray reflectivity refinement program utilizing differential evolution," *J. Appl. Crystallogr.* **40**, 1174 (2007).

[12] J. Martínez-Blanco, V. Joco, C. Quirós, P. Segovia, and E. G. Michel, "Surface x-ray diffraction analysis using a genetic algorithm: the case of Sn/Cu(100)-$(3\sqrt{2} \times \sqrt{2})$R45°," *J. Phys.: Condens. Matter* **21**, 134011 (2009).

[13] R. Storn and K. Price, "Differential Evolution — A Simple and Efficient Heuristic for global Optimization over Continuous Spaces," *J. Glob. Optim.* **11**, 341 (1997).

[14] M. Wormington, C. Panaccione, K. M. Matney, and D. K. Bowen, "Characterization of structures from X-ray scattering data using genetic algorithms," *Phil. Trans. R. Soc. Lond. A* **357**, 2827 (1999).

[15] OriginLab®, "Origin®: Data Analysis and Graphing Software," `http://www.originlab.com/index.aspx?go=PRODUCTS/Origin`.

[16] MathWorks®, "MATLAB®: The Language of Technical Computing," `http://www.mathworks.com/products/matlab/`.

# CHAPTER V

# ZnO Polar Surfaces and Schottky Interfaces

## 5.1 Introduction

The experimental results and discussion about the ZnO Zn-polar (0001) and O-polar ($000\bar{1}$) surfaces and Schottky interfaces are published in peer-reviewed journals (Zn-polar surface: [1], O-polar surface: [2]). A significant part of this chapter consists of the text and figures from the published articles.

## 5.2 Zn-polar Surface Results

### 5.2.1 Measurements and Analysis

For each sample, at least 8 symmetrically-inequivalent ($p6mm$) and several equivalent CTRs were recorded, typically resulting in 400-700 averaged structure factors per data set and systematic errors of 5-10% between symmetry equivalents (see Table 3.1). The measured structure factors were fitted using a specialized module for *GenX* [3], as described in Section 4.3.3. All fits were repeated at least ten times with random parameter initializations to verify the reproducibility and uniqueness of a solution. To give the low-intensity regions of the CTRs a similar weight in the fit as the high-intensity points close to the Bragg peaks, a logarithmic $R$-factor, $R_{\log}$, was employed for the fitting FOM, and all final fit results are also given in terms of the standard crystallographic $R$-factor (see Section 4.3.3 for FOM definitions).

### 5.2.2 Results

In-plane line scans along high-symmetry directions gave no evidence for surface or interface reconstructions on any sample. The out-of-plane CTR measurements revealed a 6-fold rotational symmetry of the diffraction pattern ($p6mm$), consistent

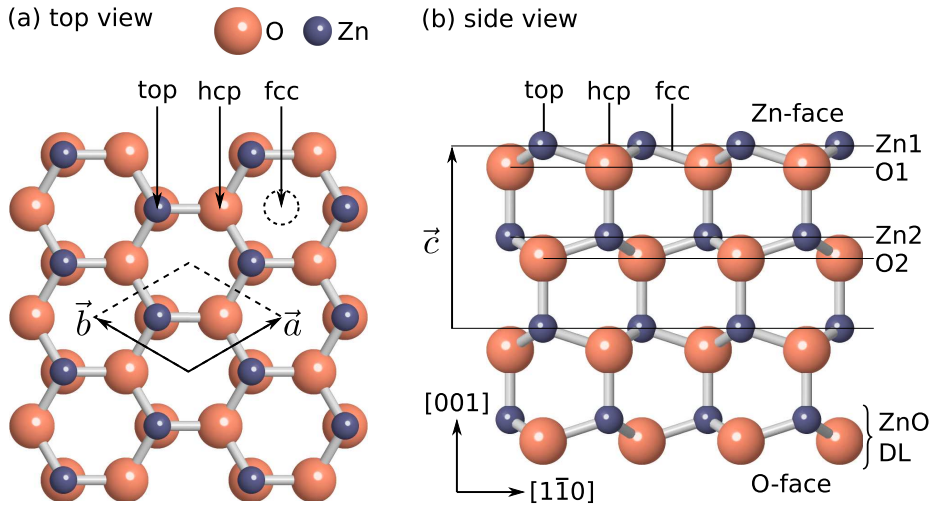


Figure 5.1: Atomic structure of a bulk-like ZnO (0001) surface. (a) Top view with the surface unit cell. (b) Side view along the [110] direction. Note the presence of two ZnO double layers (DLs) within the unit-cell height $c$. Also indicated are the three high-symmetry positions in the crystal unit cell at the on-top (top), hexagonal closed-packed hollow (hcp) and face-centered cubic hollow (fcc) sites.

with the presence of two 180°-rotated domains with local $p3m1$ symmetry separated by 1/2 unit-cell height terrace steps [4]. This agrees with AFM measurements on hydrothermal ZnO (0001) Zn-polar surfaces prepared in an identical manner, which have shown evidence of triangular islands and pits with 180° rotation between triangles on terraces separated by a single DL step [5].

To identify the characteristic structural features, we tested a large number of different models with varying degrees of complexity based on the bulk-like surface structure shown in Figure 5.1. Atomic $z$-displacements ($\Delta z$), occupations ($p_{\mathrm{occ}}$), and Debye-Waller factors of all atoms in up to four ZnO DLs were allowed to vary freely. The local $p3m1$ surface symmetry only permits atomic movements $\Delta z$ along the $z$-direction and allows adatoms to be present in just three different positions in the unit cell: at $(x, y) = (0, 0)$ (fcc hollow), $(1/3, 2/3)$ (on-top), and $(2/3, 1/3)$ (hcp hollow) [6]. In addition to a completely bulk-like structure, we tested various models with adatoms (both oxygen or metal atoms) located at some or all of these allowed locations and free to move within one unit cell away from the surface.

The results of these survey fits draw a consistent picture of the chemical nature of the surfaces or interfaces across all samples, including those coated with metal Schottky layers. The occupation parameters of zinc reveal a sharp surface/interface where only the topmost atomic layer (Zn1) is partially occupied with $p_{\mathrm{occ}}(\mathrm{Zn1}) < 40\%$.

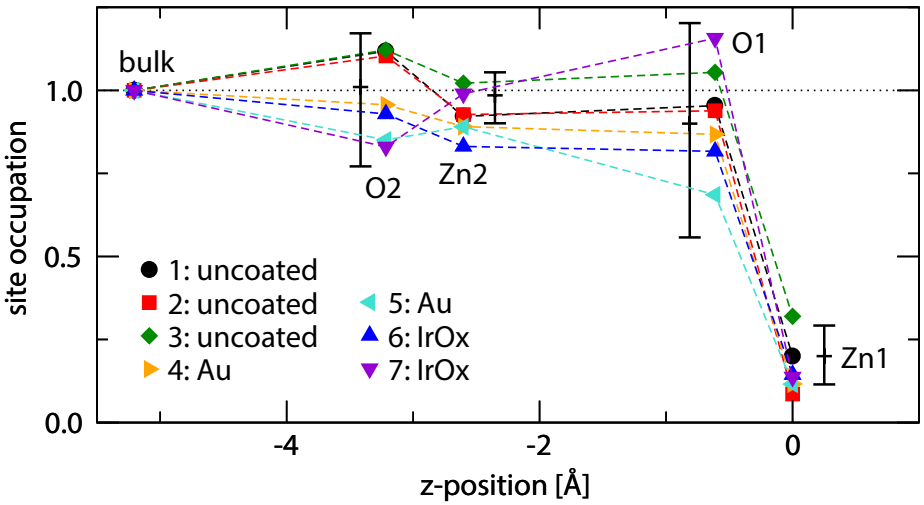


Figure 5.2: Fitted occupation profiles for a bulk-like model for all data sets. Zn1, O1, Zn2, and O2 are defined in Figure 5.1. Average error bars of individual data points are shown next to the data.

The oxygen (O1) occupation within the same DL is, however, close to unity, as is the zinc (Zn2) occupation in the next DL below. An example of this is seen in Figure 5.2, which shows the fitted occupation profile for a bulk-like model without adatoms. When including the adatoms located in the high-symmetry sites on the surface in the fits, we usually observe a comparable partial occupation of oxygen adatoms above the incomplete Zn-layer in the epitaxial on-top position, while the occupations in fcc and hcp hollow sites remain negligible. Consequently, we find an oxygen atom above each Zn atom in the structure, providing strong evidence for the presence of an oxygen overlayer on top of the nominally Zn-terminated surface. On the other hand, no indications exist for the presence of any other ordered adsorbed species or, in particular, the ordering of metal atoms in those samples with metal Schottky contacts.

The partial occupation of the Zn1 layer and its associated oxygen adatoms is most likely attributed to islands and terrace steps on an otherwise atomically flat surface and is a result of averaging over more than one distinct terrace level within the coherence length of the x-rays (typically a few hundred nm). This scenario is consistent with AFM topography measurements on identically prepared samples [5], which show terraces extending over several hundred nm, covered with smaller islands or pits of 30-200 nm in size and half a unit cell in height. As a consequence of this averaging, all atoms in the initial fits (see Figure 5.2) represent a mixture of two or more distinct atoms in different positions with respect to the surface, which are

therefore subject to chemically unequal environments. For example, a large fraction ($> 60\%$) of the O1 atoms forms the overlayer adatom on top of the fully occupied lower terrace level (above the Zn2 atoms), while the rest is associated with fourfold coordinated oxygen atoms within the upper terrace (below the topmost Zn1 layer).

To retrieve the structural relaxations within each individual terrace, it is therefore necessary to use a model that calculates the scattering contributions from different terrace levels separately. The total calculated scattering intensity then consists of a coherent addition of individual terrace contributions, taking into account the proper symmetry operations. These contributions are weighted by occupation factors, determined by fitting, for each terrace level. The atomic model for the structure at the individual terrace level is similar to that used in previous fits, consisting of a bulk-like Zn-terminated surface with possible adatoms at the high-symmetry on-top, fcc-hollow, and hcp-hollow sites. Only the adatom occupations are allowed to vary, as all the other occupation parameters are determined through the terrace occupations. Displacement and Debye-Waller factors were fitted down to the second DL, including overlayer adatoms. More detailed description about modeling of terraced surfaces can be found in Chapter II.

Regarding the presence and nature of the oxygen overlayer, the terrace model confirmed the initial results. Most importantly, we found no indications for structural differences between the uncoated and metal-covered samples. This is qualitatively evident from their exceedingly similar CTR shapes (see Figure 5.3), as large changes in the measured intensities would be expected if either an ordering of the relatively heavy metal atoms or a significant rearrangement of zinc or oxygen atoms at the interface did occur. When fitting the oxygen occupations of all high-symmetry adatoms simultaneously, the coverages for the on-top atoms were consistently close to unity, while the fcc- and bcc-hollow sites showed significantly smaller occupations. Alternatively, when allowing oxygen to be present at only one of the three sites, the lowest FOM on all samples was always achieved with the overlayer atom in the on-top position. Finally, oxygen adatoms always produced better fits than other adatom species; in particular, any of the metals used to produce the Schottky contacts.

Based on this evidence, the on-top oxygen overlayer was accepted as the best description of the surface structure. Figure 5.3 shows the excellent agreement between measured diffraction data and simulated CTR profiles. The corresponding final FOM values and fit parameters are summarized in Table 5.1. All ten randomly initialized fits for each sample converged to the identical solution. The occupation of the overlayer atom, $O_{OL}$, was consistently unity within the error bars, resulting in a fully

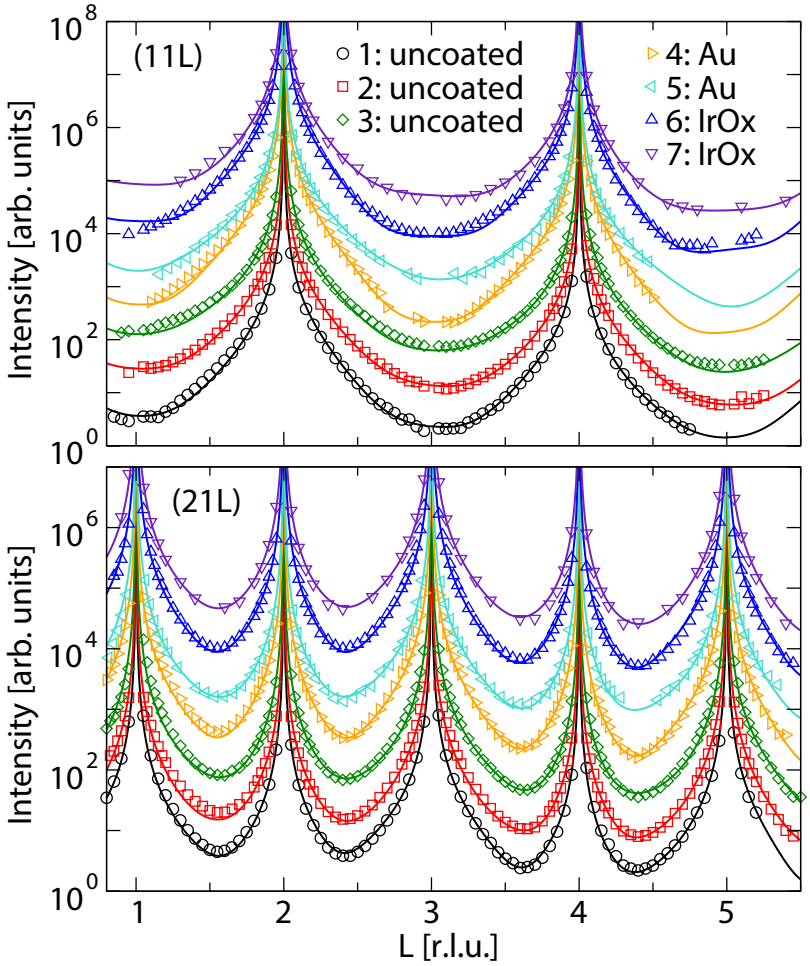


Figure 5.3: Measured diffraction data (open symbols) and corresponding calculated intensities (lines) based on the fitted on-top oxygen overlayer structure for two representative CTRs on all samples. Error bars are smaller than the data points and have been omitted.

covered (1×1) surface structure. The Debye-Waller factors within the topmost ZnO DLs always gave values close to those reported for bulk crystals [7], and manually modifying them had no significant influence on the optimized values of any other parameters. For the overlayer oxygen atoms, the fitted Debye-Waller factors were on average approximately ten times higher than for those in the bulk.

The fitted $z$-displacements are plotted in Figure 5.4. No detectable atomic movements exist for the Zn atoms, while the O1 and O2 atoms seem to relax inwards slightly. However, the observed displacements are small ($< 10$ pm, see Table 5.1), and the sample-to-sample fluctuations of the results are comparable to the observed effect. The error bars of individual displacement values, defined through a 5% increase of the FOM value [3], are of similar magnitude. The average sizes of error

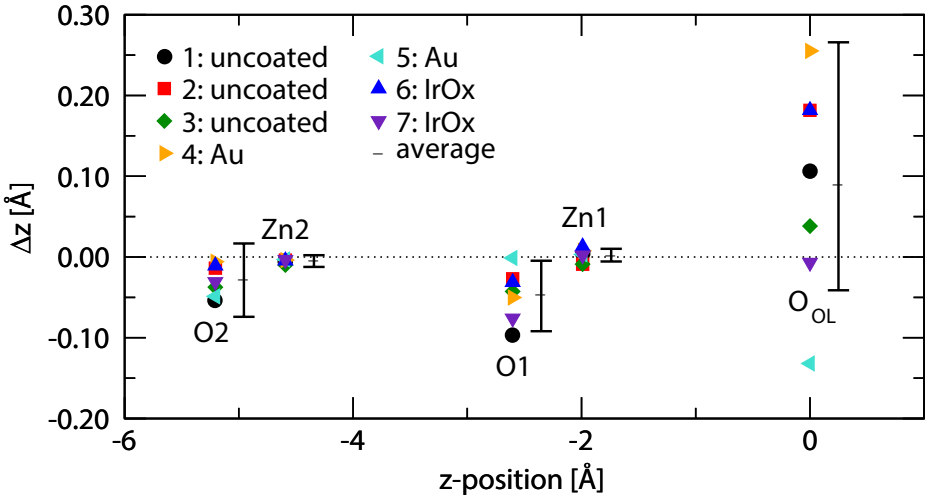


Figure 5.4: Fitted $z$-displacements $\Delta z$ for all samples. Average displacement values and averaged error bars are shown to the right of the data points of individual samples. Refer to Table 5.1 for a complete list of parameter values and uncertainties.

Table 5.1: Final fit results on all samples. $R_{\log}$ and $R$ are given in percent (%); $z$-displacements, $\Delta$z, have units of picometers (pm). Uncertainties in the last digits are shown in parentheses, i.e., 0.33(73) reads $0.33 \pm 0.73$.

| Sample | 1 | 2 | 3 | 4 | 5 | 6 | 7 |
|---|---|---|---|---|---|---|---|
| $R_{\log}$ | 3.90 | 1.64 | 1.56 | 1.71 | 1.49 | 2.07 | 1.68 |
| $R$ | 5.88 | 6.78 | 7.16 | 7.53 | 4.71 | 8.23 | 4.49 |
| $p_{\mathrm{occ}}(\mathrm{O_{OL}})$ | 1.00(12) | 1.00(30) | 1.00(41) | 1.00(21) | 0.89(30) | 1.00(26) | 0.92(39) |
| $\Delta z(\mathrm{O_{OL}})$ | 11(11) | 18(20) | 4(30) | 26(12) | -13(16) | 18(20) | -1(18) |
| $\Delta z$(Zn1) | 0.40(80) | -0.90(71) | -0.89(88) | 0.76(94) | 0.33(73) | 1.27(1.16) | 0.22(80) |
| $\Delta z$(O1) | -9.7(3.5) | -2.7(3.3) | -4.3(5.9) | -5.0(4.3) | -0.1(4.6) | -3.1(5.0) | -7.6(7.2) |
| $\Delta z$(Zn2) | -0.50(67) | -0.38(62) | -0.99(92) | -0.39(70) | -0.31(1.01) | -0.45(81) | -0.34(80) |
| $\Delta z$(O2) | -5.4(4.2) | -1.4(3.3) | -3.7(5.0) | -0.6(4.8) | -4.9(5.2) | -1.1(6.2) | -3.1(5.5) |

bars and average displacement values are shown to the right of the data points in Figure 5.4. For the $\mathrm{O_{OL}}$ atom, most samples show an outward relaxation, but again, the displacements are comparable to the sample-to-sample variations and the individual error bars. The values are also compatible with zero displacements, given their individual uncertainties as listed in Table 5.1 (sample 4 seems to be somewhat of an outlier, but remains within statistically reasonable limits). In conclusion, we do not observe any significant displacements larger than the experimental uncertainties. This is qualitatively consistent with the very symmetric CTR shapes shown in Figure 5.4, as considerable asymmetries in the CTRs indicate strong relaxations.

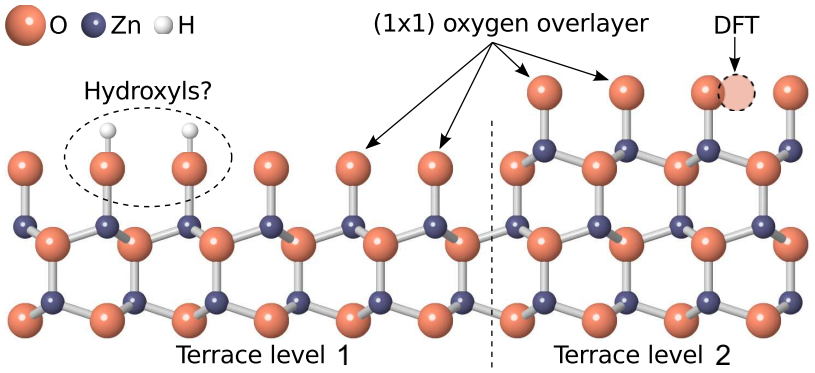


Figure 5.5: Atomic model of the structure giving the best fit to the experimental data, shown in the presence of a terrace step. A (1×1) oxygen overlayer in the on-top position above the last zinc atom covers the entire surface, and is most likely associated with hydroxyl groups in the case of the uncoated surfaces. Also indicated is the most stable oxygen adsorption site predicted by DFT calculations, which is at the the fcc-hollow site [12–14].

### 5.2.3 Discussion

The structural results are summarized in the atomic model shown in Figure 5.5. The observed (1×1) oxygen overlayer on the uncoated Zn-polar ZnO surface is most likely associated with a fully hydroxylated surface, as has been observed by x-ray photoemission spectroscopy (XPS) [8–10]. The presence of hydroxyl (OH) groups, instead of only the observed oxygen atoms, is consistent with the SXRD data, since SXRD lacks sufficient sensitivity to detect the single electron belonging to the hydrogen atoms of the OH groups. Previous XPS measurements on the same epi-polished hydrothermal ZnO material indicate a stable OH coverage of at least 1 monolayer (ML) on the Zn-polar face [10]. The bonding of these hydroxyl groups on the Zn-polar face appears to be very stable, as the XPS signal associated with surface OH bonds remaining clearly visible upon heating of samples in vacuum up to approximately 600°C. Typically, several sputtering and annealing cycles are necessary to completely remove all traces of the OH coverage [11].

Interestingly, the ordered (1×1) oxygen layer remains intact when the surfaces are covered with plain or oxidized metal Schottky contacts. The presence of oxygen at the interface is consistent with *ab initio* calculations of the adsorption of Cu atoms on polar ZnO surfaces and the role of chemical bonding at metal-ZnO interfaces, which indicate that a direct metal-zinc bonding is unfavorable and associated with ohmic rather than the experimentally observed Schottky contact behavior [15–17]. Whether metal adsorption occurs on top of the surface OH groups or by replacing the H atoms

remains unclear from the experimental results, as the detection of hydrogen at buried interfaces is extremely challenging.

From a theoretical standpoint, the formation of a (1×1) oxygen or hydroxyl overlayer is not well understood, as such an arrangement violates the electron counting rule and has been predicted to be thermodynamically unfavorable by density-functional theory (DFT) [12, 13, 16, 18, 19]. Furthermore, this fully occupied overlayer does not appear in any of the calculated phase diagrams for ZnO, which predict no stable phases with greater than 1/2 ML OH coverage and OH adsorption at fcc-hollow rather than on-top sites [12–14] (see Figure 5.5). Our experimental results therefore indicate that alternative stabilization mechanisms that differ from those seen in DFT results may play an important role at surfaces prepared under typical device fabrication conditions.

## 5.3 O-polar Surface Results

### 5.3.1 Measurements and Analysis

Crystal truncation rod datasets from O-polar surfaces also exhibited a $p6mm$ plane-group symmetry on all samples, similar to those of Zn-polar surfaces. A minimum of eight independent CTRs were recorded for each sample. Symmetry averaging resulted in 350-1000 averaged structure factors for each sample with less than 20% systematic errors (see Table 3.2). Again, the genetic algorithm refinement program *GenX* [3] was used for the fitting, and each model was fitted at least 10 times with random initial parameters. Since the O-face CTR intensities near the midpoint between the Bragg peaks were too weak to be measured, there are several gaps between the measured datapoints. In this case, the calculated intensities from the correct model should be weaker than the lowest measurable intensity in the gap region. During the fitting process, however, the FOMs are calculated only with the actually measured datapoints, and the solution with the lowest FOM can show strong intensities in the gap region, which is incorrect. To prevent this overshooting problem in the weak intensity region, a special logarithmic FOM was employed, so that the FOM increases if the simulated intensities overshoot in the gap region. More details about the overshoot prevention can be found in Appendix E. The final FOM is given as the standard crystallographic $R$-factor [1].

The observed $p6mm$ symmetry in the diffraction patterns of ZnO O-polar $(000\overline{1})$ surfaces is the result of two evenly distributed 180°-rotated surface terminations with local $p3m1$ symmetry [20], separated by half-unit-cell steps. To simulate the structure

factors with the correct symmetry and to prevent atomic displacement averaging over multiple terrace steps when introducing surface roughness into the model, a stack-based roughness model was employed. In short, the roughness is introduced by calculating the coherent average over a number of identical but vertically shifted (and, in the case of ZnO, rotated by 180 degrees with respect to the next one) unit stacks. These stacks correspond to the traditional surface models, which describe the local atomic structure on the unit cell level as a function of position from the surface, and contain the usual occupation, Debye-Waller and displacement parameters for each atom. By assigning weight factors to each of the shifted stacks, arbitrary roughness profiles can be simulated. A detailed mathematical description about the SXRD diffraction intensity calculation with roughness modeling can be found in Chapter II.

To allow for a sufficiently broad roughness distribution in the fits, we used a total of sixteen stacks, displaced by half a unit cell in the vertical direction and rotated by 180 degrees about the surface normal with respect to each other. This corresponds to a range of eight ZnO unit cells, which is sufficient to model the height variations encountered within the in-plane x-ray coherence length (typically a few hundred nm). Additionally, the occupancy of the topmost oxygen atom was also fitted to allow for unequal occupations of the zinc and oxygen atoms within a single atomic Zn-O double layer. The roughness was fitted with two different approaches. In the first model, the stack occupations were calculated based on a Gaussian roughness profile, resulting in an error-function-shaped occupation profile of the atomic planes. The only free fit parameter in this case was the width of the Gaussian distribution. The second model allowed all of the individual stack occupancies to vary freely, only constraining the sum of all stack occupations to equal unity (hence resulting in $N - 1$ free fit parameters, where $N$ is the number of stacks).

To confirm the roughness values extracted from SXRD, AFM images were recorded on two of the bare surfaces (samples 2 and 3) using an Asylum Research MFP-3D AFM in tapping mode. In addition to the ultrasonic cleaning procedure applied before the SXRD measurements, the samples were annealed at 350°C for three hours to remove organic material which had accumulated on the surfaces.

### 5.3.2 Results

Previous studies of the ZnO $(000\bar{1})$ surface observed the presence of $\sqrt{3} \times \sqrt{3}$ reconstructions for the surface annealed above 1100°C in UHV [21]. Scans at various non-integer order reciprocal points, corresponding to the $\sqrt{3} \times \sqrt{3}$ surface reconstructions, and additional in-plane scans along high-symmetry directions showed no

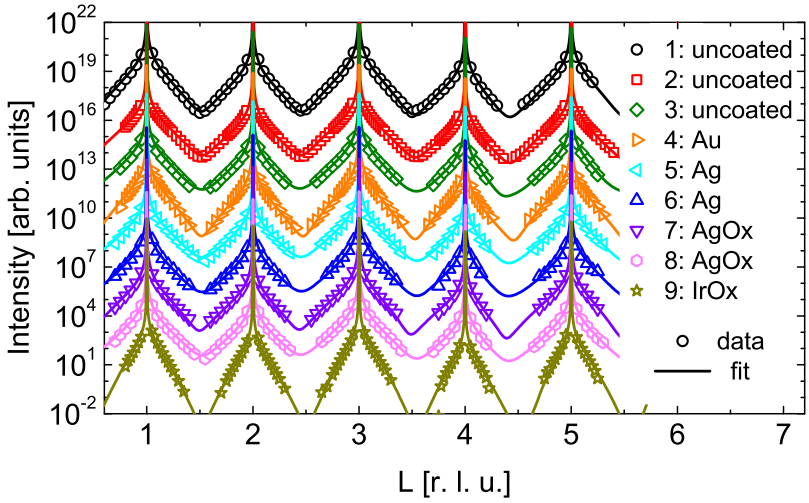


Figure 5.6: Measured CTRs and final fits for the (21L) rod of all samples. The experimental uncertainties are much smaller than the data symbols.

Table 5.2: Final fit results for all samples. All Δz values are given in pm.

| Sample | 1: unc. | 2: unc. | 3: unc. | 4: Au | 5: Ag | 6: Ag | 7: $AgO_x$ | 8: $AgO_x$ | 9: $IrO_x$ |
|---|---|---|---|---|---|---|---|---|---|
| R (%) | 5.88 | 6.52 | 8.92 | 9.09 | 5.51 | 8.78 | 7.33 | 7.38 | 10.5 |
| $p_{occ}$(O1) | 1.00(27) | 1.00(25) | 0.76(23) | 1.00(38) | 0.96(33) | 0.96(33) | 0.68(38) | 0.66(35) | 1.00(45) |
| Δz(O1) | -9.2(130) | -14(10) | -13(11) | -1.1(140) | -8.6(140) | -7.0(120) | -6.0(270) | -7.2(260) | -23(250) |
| Δz(Zn1) | 2.9(11) | 3.9(11) | 2.7(10) | 3.4(15) | 1.5(12) | 0.8(14) | 9.5(26) | 8.6(28) | -5.8(78) |
| Δz(O2) | -9.0(130) | 2.9(64) | 2.4(80) | -5.9(110) | -4.8(100) | -11(10) | -7.5(120) | -3.9(130) | -2.0(160) |
| Δz(Zn2) | -0.6(22) | 1.8(15) | -0.3(21) | 2.2(28) | 0.0(23) | -0.1(34) | -1.6(30) | -0.6(33) | 3.3(11) |
| Δ(O1-Zn1) | -12(13) | -18(10) | -16(11) | -4.5(141) | -10(14) | -7.8(120) | -16(27) | -16(26) | -17(26) |
| FWHM (Å) | 7.62(17) | 6.56(26) | 6.33(22) | 8.66(26) | 6.24(25) | 6.46(27) | 7.07(33) | 6.97(41) | 11.51(44) |
| miscut (°) | 0.020 | 0.005 | 0.039 | 0.012 | 0.031 | 0.025 | 0.056 | 0.034 | 0.039 |

evidence for the existence of any reconstructions in our samples. The presence of adatom ordering within the Schottky overlayer was carefully checked by comparing with several models. However, unlike in the case of the ZnO Zn-polar (0001) surface [1], none of the samples showed any indication of overlayer adatoms in any of the symmetrically allowed positions. Also, any atomic displacements in the in-plane direction are prohibited by the observed *p6mm* symmetry. Therefore, our final model included only the atomic $z$-displacements ($\Delta z$) and Debye-Waller factors of all four atoms within the topmost unit cell, the topmost oxygen (O1) atom occupation ($p_{occ}$), and the surface roughness profile as fitting parameters. A wurtzite ZnO unit cell with lattice parameters of a = 3.2494 Å and c = 5.2054 Å was used for the bulk structure of the crystal.

Figure 5.6 shows the measured CTRs and fit results based on the Gaussian roughness model for the (21L) rod. The corresponding crystallographic R factors [1] and fit parameters are listed in Table 5.2. Compared to the U-shaped Zn-polar surface CTRs [1], the intensities of the O-polar surface CTRs fall off more rapidly away from

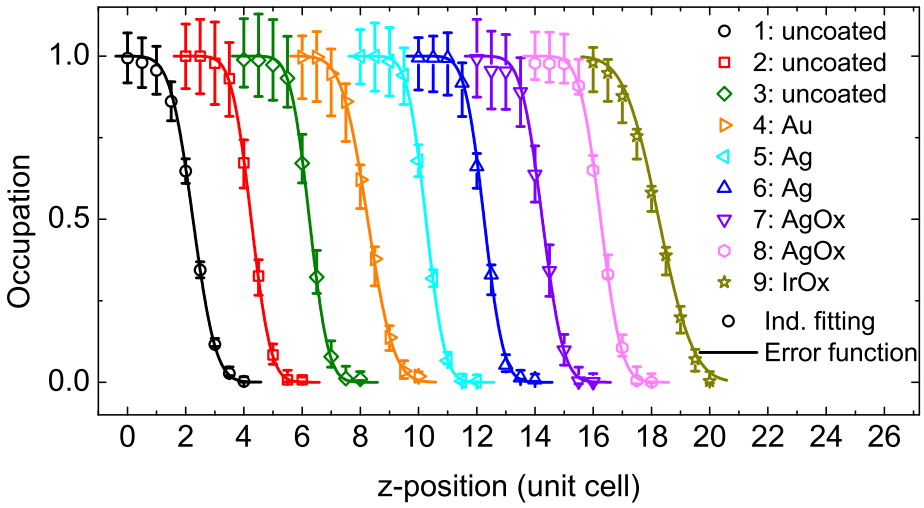


Figure 5.7: Fitted roughness profiles, both for the individual stack occupations (data points) and the Gaussian roughness model (solid line). The individual profiles have been displaced horizontally for clarity.

the Bragg peaks, forming more V-shaped intensity profiles (on a log scale). This exponential decay of intensity indicates that the surfaces have a significant roughness profile within the x-ray coherence length. Sample 9 ($IrO_x$) has a steeper intensity decay compared to all other samples, which exhibit almost identical CTR shapes. Interestingly, no obvious differences exist between uncoated, plain metal-coated, and oxidized metal-coated samples.

The fitted roughness profiles for each sample are shown in Figure 5.7. Allowing the individual stack occupations (represented by the data points) to vary freely always results in a nearly Gaussian roughness profile (solid lines). The full widths at half maximum (FWHM) of the roughness distributions are listed in Table 5.2 and are typically 6-9 Å. The only exception is the $IrO_x$-coated sample with a much broader roughness profile (FWHM ∼12 Å), as expected from its sharper CTR shape. Sample miscut, resulting in an increase in the number of terrace step edges, can be ruled out as the cause of the measured roughness profiles: the miscut angles between the optical and crystallographic surface planes were measured to be less than 0.06° on all samples (see Table 5.2), yielding average terrace widths greater than 250 nm.

Atomic force microscopy (AFM) measurements on the two bare samples 2 and 3 corroborate the results of the SXRD measurements. The AFM image in Figure 5.8 (a) shows that roughness features are very localized. The histogram of the height distribution in panel (b) confirms the Gaussian nature of the roughness profile. The FWHM of the height distributions extracted from the AFM images are 5.14 Å and

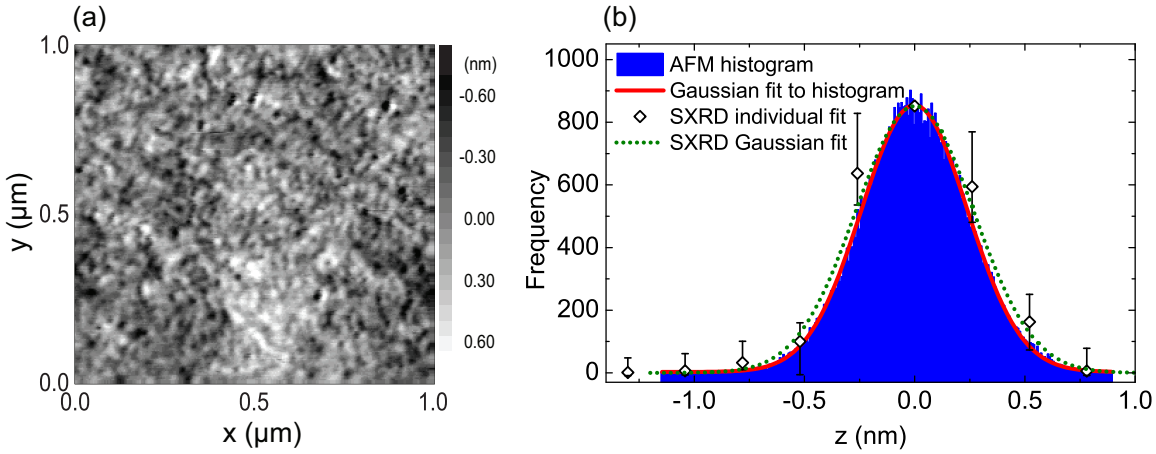


Figure 5.8: (a) AFM image obtained on the bare surface of sample 3. (b) Histogram of the height distribution from the image shown in (a). A Gaussian fit to the histogram is shown by the red line (FWHM = 5.67 Å). Also plotted are the fitted stack occupation parameters (symbols) and Gaussian roughness profile (green dotted line) obtained from the SXRD data, illustrating the good agreement between both measurement methods.

5.67 Å for samples number 2 and 3, respectively, and therefore slightly narrower than those obtained by SXRD.

Table 5.2 also lists the fitted occupations of the topmost oxygen atom. Only three samples (sample 3: uncoated and sample 7, 8: $AgO_x$-coated) appear to have oxygen occupancies of less than one (66%-76%). Interestingly, samples 7 and 8, both coated with oxidized silver, have an under-occupied topmost oxygen layer, whereas the plain silver-coated samples (samples 5, 6) have fully occupied top layers.

The results for the atomic displacements are plotted in Figure 5.9 with the numerical values given in Table 5.2. As expected from the significant difference in the CTR shape, the detailed structure of the $IrO_x$-coated sample is quite different from that of the other samples. The topmost oxygen atoms (O1) are displaced downwards for all samples (0.098 Å on average), but for the $IrO_x$ sample, the displacement is more than twice the average. The Zn atoms directly below the topmost oxygen atoms (Zn1) are displaced outwards (0.030 Å on average), again in contrast to those on the $IrO_x$-coated sample, which show an inward movement. For samples 7 and 8 (both $AgO_x$-coated), which have a significantly lower occupancy of the topmost oxygen layer, the Zn1 atoms are displaced by more than twice the average. Moving further into the bulk, the movements of O2 and Zn2 atoms are considerably smaller and, in fact, compatible with zero within the error bars. The fitted Debye-Waller factors for the topmost four atoms remain very close to the bulk values for ZnO, indicating that

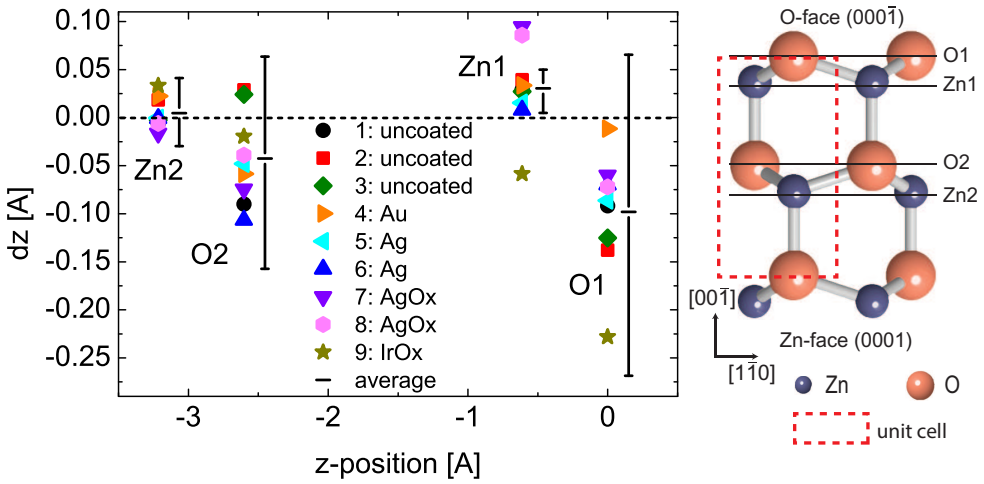


Figure 5.9: Atomic displacements of the atoms within the topmost unit cell. The displayed error bars are calculated as the average over the individual error bars of all nine samples.

the surface structure remains very well ordered.

In discussing these results, it is important to understand that the measured CTR intensities are a result of scattering from a well-ordered crystalline atomic arrangement. As such, they are insensitive to contributions from disordered parts of the sample, such as crystal defects, randomly distributed interstitials, amorphous surface layers, etc. All of these latter effects would result in a broader intensity distribution around the sharp CTR and Bragg peak signals. While we have not explicitly focused on these broader diffraction features, we have not found any evidence for significant disorder in the samples based on the sharp intensity distributions recorded on the area detector. We conclude that our samples were very well ordered, and that the potentially remaining level of disorder has a negligible effect on the results of our structural analysis. This does not imply, however, that we can exclude with certainty the presence of any unordered species in our system, which may have an impact on the physical properties of the Schottky contacts, but simply that our structural measurements are not affected by them.

### 5.3.3 Discussion

The nature of the surface termination of the ZnO O-polar surface has been the subject of much debate [19, 22–24], with several different proposed terminations, including a pure 1×1 [19, 23], a 1×1 with a 1/2 ML of hydrogen adatoms [19, 22], and a 1×3 with a 1/4 ML of oxygen vacancies [19, 22]. The fact that none of the investigated samples showed any signs of surface reconstructions excludes the 1×3

termination from the candidates. Also, a significant amount of surface hydroxyl coverage is reported from XPS experiments performed on identically prepared uncoated samples [10], supporting the hydrogenated termination for uncoated samples. Theoretically calculated ZnO O-polar surface phase diagrams have been published [19], which predict a 1/2 ML hydrogen adatom coverage in atmospheric oxygen and hydrogen partial pressures.

The three uncoated samples and all of the plain-metal-coated samples show a very similar surface structure, both regarding the topmost oxygen occupation and the atomic displacements, indicating a fully occupied 1×1 oxygen termination regardless of the existence of a metal contact on the surface. Unfortunately, direct evidence for hydrogen adatoms cannot be verified with our x-ray measurements due to their small x-ray scattering cross section. An accurate determination of the oxygen occupation parameters is hampered for the same reason, as the sensitivity of x-ray diffraction to small electron densities is limited (note that 1/4 of an oxygen atom corresponds to two electrons, equivalent to the scattering from two H atoms). As such the somewhat smaller oxygen occupation for sample 3 (76% ±23%) may be an artifact of this limited sensitivity, and is compatible with the other fully occupied samples within the error bars. The observed atomic displacements are consistent with the reported results of first principles calculations [19, 20, 25–27]. These theoretical studies predict a strong inward relaxation of the topmost oxygen layer and an outward displacement of the Zn atoms in the layer underneath. This results in a contracted layer spacing between the topmost oxygen and zinc layers compared to the bulk value of 0.61 Å by an amount of -0.189 Å, -0.272 Å [26], -0.207 Å [27], -0.260 Å [25], -0.307 Å [19], -0.25 Å [24], and -0.234 Å [20]. As can be seen in Table 5.2, our measured values for the contraction, $\Delta$(O1-Zn1), confirm the reduced layer spacing, but to a somewhat lesser degree than the predicted amounts. This difference can possibly be attributed to the presence of the hydrogen adatom, which can stabilize the polar surface without strong atomic displacements; a calculation which reported significantly less atomic relaxation of the topmost double-layer in the presence of hydrogen supports this finding [19].

Interestingly, the two $AgO_x$-coated samples (samples 7 and 8) show a consistently different structure. The oxygen occupation of the top layer is reduced by approximately 1/3, and the outward relaxations of the Zn1 atoms are significantly larger by almost a factor of two compared to the uncoated and plain-metal-coated samples (see Table 5.2). Again, the oxygen occupation parameters themselves have large uncertainties, but the fact that they are consistent between the two samples and that they are accompanied by large positional changes of the much heavier Zn1 atoms suggest

that this is not just an artifact, but the differences in comparison to the other samples are real. The fact that we do not observe any reconstruction signals indicates that the oxygen vacancies are not ordered. The reduced oxygen occupation at the surface may at first seem counter-intuitive, since these oxidized samples were prepared in a relatively oxygen-rich environment compared to the plain Ag-coated samples. One has to keep in mind, though, that these samples have been coated at room temperature under conditions far from thermodynamic equilibrium. It is, therefore, quite conceivable that the incorporation of ZnO surface oxygen into a non-stoichiometric $AgO_x$ matrix is more easily achieved than into the pure silver metal film, for example, as a direct consequence of the different lattice distortions. Moreover, according to the theoretical phase diagram [19], oxygen vacancies on uncoated surfaces are expected only at very low oxygen partial pressure ($< 10^{-10}$ $mbar$), but silver is known to be an excellent oxidation catalyst and could potentially lower the energy barrier for the removal of surface oxygen. Unfortunately, our x-ray study of the final structural surface state cannot give any indication of how this equilibrium state was reached, and more detailed chemical studies are clearly needed to elucidate the effect of the oxygen environment on the surface hydroxyl interaction with silver during the deposition.

The $IrO_x$-coated sample (sample 9) shows a markedly different behavior compared to the other eight samples in terms of the shape of the measured CTRs, the roughness FWHM, and atomic displacements. We measured the FWHM of the roughness profile of the $IrO_x$-coated surface to be 2 ML, compared to about 1.5 ML for all the other O-face ZnO samples. Cross-sectional transmission electron microscope (XTEM) images of $IrO_x$/ZnO samples, prepared in an identical manner to those reported here, show a distinct amorphous layer at the interface. Moreover, electron energy loss spectroscopy (EELS) data show evidence for the out-diffusion of the Zn atoms approximately 30 nm into the $IrO_x$ film [28]. These previously reported measurements indicate that the ZnO surface is significantly affected during the EPLD growth. Although the unordered Zn atoms diffused into the amorphous interface layer cannot be detected directly from the CTR intensities, the much wider roughness profile that we observe in the $IrO_x$-coated sample is consistent with the Zn out-diffusion since the diffusion of Zn atoms would indeed make the ordered ZnO surface rougher. Considering that the $IrO_x$-coated sample is the only one of our samples prepared by EPLD, the outlying behavior of this sample is very likely attributed to the different deposition conditions, and not necessarily due to the difference in contact metal.

Finally, we note here that the surface preparation by $Ar^+$ ion sputtering followed by UHV annealing [20, 24] has been shown to lead to atomically smooth O-terminated

ZnO surfaces, with U-shaped CTRs similar to those reported for the Zn-polar (0001) surface [1, 20]. The surface roughness therefore seems to be affected significantly by the sample environment and preparation conditions.

## Bibliography


[1] C. M. Schlepütz, Y. Yang, N. S. Husseini, R. Heinhold, H.-S. Kim, M. W. Allen, S. M. Durbin, and R. Clarke, "The presence of a (1×1) oxygen overlayer on ZnO(0001) surfaces and at Schottky interfaces," *J. Phys.: Condens. Matter* **24**, 095007 (2012).

[2] Y. Yang, C. M. Schlepütz, F. Bellucci, M. W. Allen, S. M. Durbin, and R. Clarke, "Structural investigation of ZnO O-polar $(000\bar{1})$ surfaces and Schottky interfaces," *Surf. Sci.* **610**, 22 (2013).

[3] M. Björck and G. Andersson, "GenX: an extensible X-ray reflectivity refinement program utilizing differential evolution," *J. Appl. Crystallogr.* **40**, 1174 (2007).

[4] N. Jedrecy, M. Sauvage-Simkin, and R. Pinchaux, "The hexagonal polar ZnO(0001)-(1×1) surfaces: structural features as stemming from X-ray diffraction," *Appl. Surf. Sci.* **162-163**, 69 (2000).

[5] M. W. Allen, R. J. Mendelsberg, R. J. Reeves, and S. M. Durbin, "Oxidized noble metal Schottky contacts to n-type ZnO," *Appl. Phys. Lett.* **94**, 103508 (2009).

[6] M. Valtiner, X. Torrelles, A. Pareek, S. Borodin, H. Gies, and G. Grundmeier, "In Situ Study of the Polar ZnO(0001)–Zn Surface in Alkaline Electrolytes," *J. Phys. Chem. C* **114**, 15440 (2010).

[7] H. Sawada, R. Wang, and A. W. Sleight, "An Electron Density Residual Study of Zinc Oxide," *J. Solid State Chem.* **122**, 148 (1996).

[8] B. J. Coppa, C. C. Fulton, S. M. Kiesel, R. F. Davis, C. Pandarinath, J. E. Burnette, R. J. Nemanich, and D. J. Smith, "Structural, microstructural, and electrical properties of gold films and Schottky contacts on remote plasma-cleaned, n-type ZnO (0001) surfaces," *J. Appl. Phys.* **97**, 103517 (2005).

[9] M. Valtiner, S. Borodin, and G. Grundmeier, "Preparation and characterisation of hydroxide stabilised ZnO(0001)-Zn-OH surfaces," *Phys. Chem. Chem. Phys.* **9**, 2406 (2007).

[10] M. W. Allen, D. Y. Zemlyanov, G. I. N. Waterhouse, J. B. Metson, T. D. Veal, C. F. McConville, and S. M. Durbin, "Polarity effects in the x-ray photoemission of ZnO and other wurtzite semiconductors," *Appl. Phys. Lett.* **98**, 101906 (2011).

[11] R. Heinhold, G. T. Williams, S. P. Cooil, D. A. Evans, and M. W. Allen, "Influence of polarity and hydroxyl termination on the band bending at ZnO surfaces," *Phys. Rev. B* **88**, 235315 (2013).

[12] M. Valtiner, M. Todorova, and J. Neugebauer, "Hydrogen adsorption on polar ZnO (0001)-Zn: Extending equilibrium surface phase diagrams to kinetically stabilized structures," *Phys. Rev. B* **82**, 165418 (2010).

[13] M. Valtiner, M. Todorova, G. Grundmeier, and J. Neugebauer, "Temperature Stabilized Surface Reconstructions at Polar ZnO (0001)," *Phys. Rev. Lett.* **103**, 065502 (2009).

[14] G. Kresse, O. Dulub, and U. Diebold, "Competing stabilization mechanism for the polar ZnO(0001)-Zn surface," *Phys. Rev. B* **68**, 245409 (2003).

[15] X.-Q. Dai, H.-J. Yan, J.-L. Wang, Y.-M. Liu, Z. Yang, and M. H. Xie, "The effect of Cu on O adsorption on a ZnO(0001) surface: a first-principles study," *J. Phys.: Condens. Matter* **20**, 095002 (2008).

[16] Y. Dong and L. Brillson, "First-Principles Studies of Metal (111) / ZnO (0001) Interfaces," *J. Electron. Mater.* **37**, 743 (2008).

[17] I. Hegemann, A. Schwaebe, and K. Fink, "Adsorption of single Cu atoms at differently stabilized polar ZnO surfaces: An ab initio study," *J. Comput. Chem.* **29**, 2302 (2008).

[18] A. Wander and N. M. Harrison, "The stability of polar oxide surfaces: The interaction of $H_2O$ with ZnO(0001) and ZnO(000$\bar{1}$)," *J. Chem. Phys.* **115**, 2312 (2001).

[19] B. Meyer, "First-principles study of the polar O-terminated ZnO surface in thermodynamic equilibrium with oxygen and hydrogen," *Phys. Rev. B* **69**, 045416 (2004).

[20] N. Jedrecy, S. Gallini, M. Sauvage-Simkin, and R. Pinchaux, "The ZnO non-polar (10$\bar{1}$0) surface: an X-ray structural investigation," *Surf. Sci.* **460**, 136 (2000).

[21] J. D. Levine, A. Willis, W. Bottoms, and P. Mark, "Correlation of electronic, LEED, and Auger diagnostics on ZnO surfaces," *Surf. Sci.* **29**, 144 (1972).

[22] M. Kunat, S. Gil Girol, T. Becker, U. Burghaus, and C. Wöll, "Stability of the polar surfaces of ZnO: A reinvestigation using He-atom scattering," *Phys. Rev. B* **66**, 081402 (2002).

[23] R. Lindsay, C. A. Muryn, E. Michelangeli, and G. Thornton, "ZnO(000$\bar{1}$)-O surface structure: hydrogen-free (1×1) termination," *Surf. Sci.* **565**, L283 (2004).

[24] A. Wander, F. Schedin, P. Steadman, A. Norris, R. Mcgrath, T. Turner, G. Thornton, and N. Harrison, "Stability of Polar Oxide Surfaces," *Phys. Rev. Lett.* **86**, 3811 (2001).

[25] M.-H. Du, S. B. Zhang, J. E. Northrup, and S. C. Erwin, "Stabilization mechanisms of polar surfaces: ZnO surfaces," *Phys. Rev. B* **78**, 155424 (2008).

[26] Z. Yufei, G. Zhiyou, G. Xiaoqi, C. Dongxing, D. Yunxiao, and Z. Hongtao, "First-principles of wurtzite ZnO (0001) and (000$\bar{1}$) surface structures," *J. Semicond.* **31**, 082001 (2010).

[27] C. Zhou and J. Kang, "Electronic structures of ZnO(0001)-Zn and (000$\bar{1}$)-O polar surfaces," *J. Mater. Sci.: Mater. Electron.* **19**, 229 (2008).

[28] E. L. Mayes, J. G. Partridge, M. R. Field, D. G. McCulloch, S. M. Durbin, H.-S. Kim, and M. W. Allen, "The interface structure of high performance ZnO Schottky diodes," *Physica B* **407**, 2867 (2012).

# CHAPTER VI

# $BiFeO_3$ Films under Compressive Strain

## 6.1 Introduction

The experimental results and discussion about the $BiFeO_3$ films grown on $SrTiO_3$ substrates are published in a peer-reviewed journal [1]. A significant part of this chapter consists of the text and figures from the article.

## 6.2 $BiFeO_3$ Thin Films Grown on $SrTiO_3$ Substrates

### 6.2.1 Measurements

Synchrotron x-ray diffraction experiments were carried out at beamlines 13-BM-C, 33-ID-D, and 33-BM-C of the Advanced Photon Source. To identify the symmetry of the $BiFeO_3$ films, high-resolution 3D-RSMs were measured around high-order film Bragg peaks and half-integer order peaks which are sensitive to the anti-ferrodistortive octahedral tilting pattern. Using a PILATUS 100K area detector [2, 3], the intensity distribution around each peak was measured in a series of single scans along the L-direction as a set of two-dimensional reciprocal space slices. These were then used to reconstruct the 3D-RSMs [4]. Note that all RSMs for $BiFeO_3/SrTiO_3$ results are presented with the same color scale, and all reciprocal space positions are given in units of the inverse substrate ($SrTiO_3$) lattice constants [reciprocal lattice units (r. l. u.)].

### 6.2.2 Results

In Figure 6.1 (a)-(c), we show (HH)L slices through the 3D-RSMs around the 335 peaks for three different film thicknesses. We observe that the signal from the 50 UC thick film [Figure 6.1 (a)] is split into three distinct peaks: a bright one at

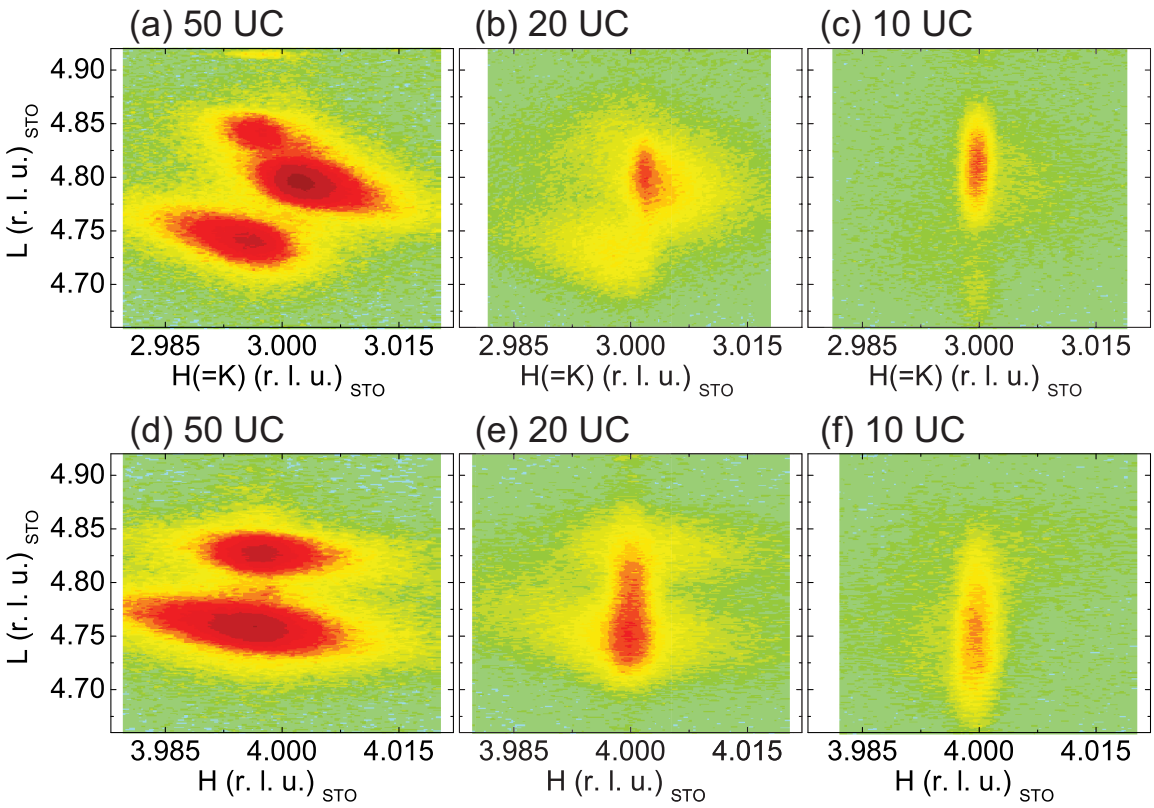


Figure 6.1: (a)-(c) (HH)L map of the $335_{pc}$ (the subscript pc refers to pseudo-cubic) peak for 50 UC, 20 UC, and 10 UC of $BiFeO_3$, respectively. (d)-(f) The corresponding HL map of the $405_{pc}$ peak for 50 UC, 20 UC, and 10 UC of $BiFeO_3$. Note that the weak intensity feature in (c) at L≈4.7 is a Laue finite-thickness fringe, and is not associated with Bragg peak splitting.

the center, and two weaker peaks above and below the center peak. This splitting pattern corresponds to the well-known $M_A$ monoclinic structure in the presence of four domains that tilt in different directions (see Appendix D), reported for $BiFeO_3$ films on $SrTiO_3$ with thicknesses greater than 26 nm [5, 6]. For the 20 UC film [Figure 6.1 (b)], however, the splitting is less pronounced, while for 10 UC [Figure 6.1 (c)], only a single peak is observed (although it is broadened in the out-of-plane direction due to the finite thickness of the film). HL maps around 405 peaks show the same behavior [Figure 6.1 (d)-(f)] with a doubly split diffraction feature transforming into a single peak. These findings prove that there is a structural phase transition as the film thickness decreases.

This disappearance of the peak splitting for the 10 UC film can be explained either by formation of a single-domain monoclinic film structure, or, alternatively, by a transition to a tetragonal film unit cell. We can distinguish between these two possibilities by carefully investigating the symmetry of selected Bragg peaks in

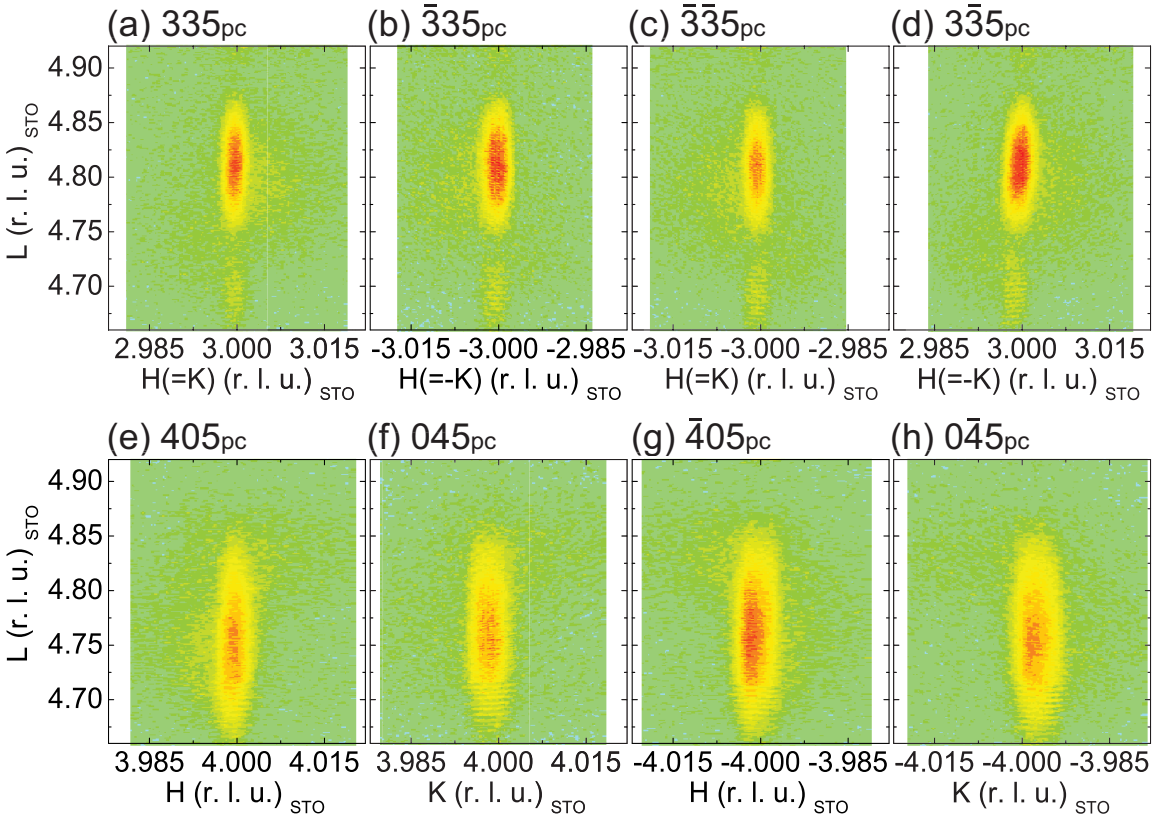


Figure 6.2: RSMs of four-fold symmetrically equivalent film Bragg peaks for the ultra-thin (10 UC) film. Both the 335 (top row) and 405 (bottom row) family of peaks are shown. (a) (HH)L map of the 335 peak (b) (H$\bar{\text{H}}$)L map of the $\bar{3}35$ peak (c) (HH)L map of the $\bar{3}\bar{3}5$ peak (d) (H$\bar{\text{H}}$)L map of the $3\bar{3}5$ peak (e) HL map around the 405 peak (f) KL map around the 045 peak (g) HL map around the $\bar{4}05$ peak (h) KL map around the $0\bar{4}5$ peak.

the 3D-RSM, as described in Appendix D. The single-domain monoclinic structure would result in a tilted film peak pattern with respect to the substrate lattice, while the tetragonal case should yield a perfectly four-fold symmetric diffraction pattern. To check the symmetry, the RSMs of four-fold symmetrically-equivalent positions for each peak were measured. Figure 6.2 (a) - (h) shows the equivalent RSMs for two families of Bragg peaks, 335 and 405, of the 10 UC film. All peaks evidently appear at the same L position, proving that the film structure is tetragonal rather than single-domain monoclinic.

In addition to the disappearance of the peak splitting, a narrowing of the peak width in the in-plane direction can be observed during the transition. The 50 UC monoclinic film peaks [Figure 6.1 (a), (d)] have an in-plane peak width of approximately 0.01 r. l. u., which corresponds to a lateral domain size of roughly 100 unit

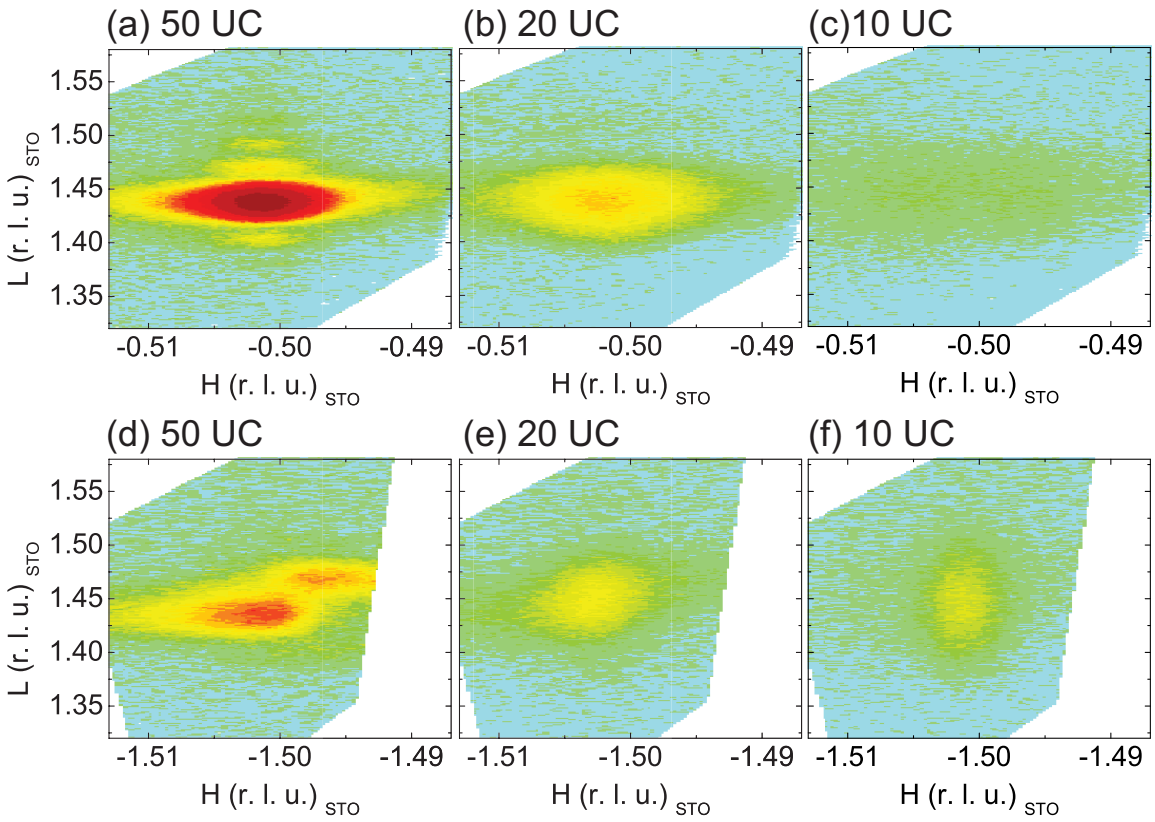


Figure 6.3: (a)-(c) HL map of the $\frac{\bar{1}}{2}\frac{\bar{1}}{2}\frac{3}{2}$ peaks for 50 UC, 20 UC, and 10 UC of $BiFeO_3$, respectively. (d)-(f) The corresponding HL map of the $\frac{\bar{3}}{2}\frac{\bar{5}}{2}\frac{3}{2}$ peak for 50 UC, 20 UC, and 10 UC of $BiFeO_3$.

cells. The 10 UC film peaks [Figure 6.1 (c), (f)], however, are much narrower (almost 1/10 of those of 50 UC film), with their widths being limited mostly by the instrumental resolution rather than the structural coherence length. This indicates that the 10 UC film is coherent with the substrate over significant distances ($>$ 400 nm) and does not form structural domains.

Definitive support for this transition from monoclinic to tetragonal symmetry comes from the measurements of half-integer order peaks associated with the oxygen octahedral tilt pattern in the $BiFeO_3$ film. For the previously reported monoclinic $M_A$ structure in the $BiFeO_3/SrTiO_3$ system, an $a^-a^-b^0$ octahedral tilt pattern is expected [6], which produces half-integer order peaks at all reciprocal space positions with strictly half-integer H, K, and L values, except where H=K=L. For the tetragonal symmetry, however, half-integer peaks at H=K positions are also expected to be missing [7]. Figure 6.3 shows the $\frac{\bar{1}}{2}\frac{\bar{1}}{2}\frac{3}{2}$ and $\frac{\bar{3}}{2}\frac{\bar{5}}{2}\frac{3}{2}$ peaks for the three film thicknesses. The H=K [$\frac{\bar{1}}{2}\frac{\bar{1}}{2}\frac{3}{2}$: Figure 6.3 (a)-(c)] peaks are becoming broader and weaker as the film thickness decreases. In contrast, the H$\neq$K peaks [$\frac{\bar{3}}{2}\frac{\bar{5}}{2}\frac{3}{2}$: Figure 6.3 (d)-(f)] are

Table 6.1: Film lattice parameters calculated from the peak positions. Note that the $M_A$ unit cell has double the volume of the tetragonal unit cell and corresponds to a $\sqrt{2} \times \sqrt{2}$ superstructure rotated by 45 degrees in plane [6]. The volume per formula unit is therefore 62.21(16) Å$^3$.

| Thickness [UC] | $a$ [Å] | $b$ [Å] | $c$ [Å] | $\alpha$ [°] | $\beta$ [°] | $\gamma$ [°] | UC volume [Å$^3$] |
|---|---|---|---|---|---|---|---|
| 10 (tetragonal) | 3.9034(38) | 3.9034(38) | 4.090(14) | 90 | 90 | 90 | 62.31(22) |
| 50 ( $M_A$ ) | 5.5220(50) | 5.5336(35) | 4.0717(98) | 89.399(46) | 90 | 90 | 124.41(33) |

narrowing with a concurrent reduction of the peak splitting, and the width of the 10 UC film peak becomes comparable to those of integer-order peaks (Figure 6.2). Comparing the intensities, the $\frac{\bar{1}}{2}\frac{\bar{1}}{2}\frac{3}{2}$ peak is brighter than the one at $\frac{\bar{3}}{2}\frac{\bar{5}}{2}\frac{3}{2}$ for the 50 UC film, but for 10 UC, the $\frac{\bar{3}}{2}\frac{\bar{5}}{2}\frac{3}{2}$ peak is more intense. The extinction of the H=K peak [Figure 6.3 (c)] means that the octahedral rotation is primarily along the $c$ axis and definitely identifies the octahedra tilt pattern as $a^0a^0c^-$, which corresponds to tetragonal symmetry.

It is important to note that the Glazer [7] selection rule assumes rigid octahedra, which may not be the case for the 20 UC film where different symmetries can coexist and a gradual change of octahedral tilting is expected. Moreover, in addition to pure rotations, distortions of the oxygen octahedra may also affect the half-order peak intensities. These can be the cause of the broad and faint intensities near the $\frac{\bar{1}}{2}\frac{\bar{1}}{2}\frac{3}{2}$ position of the ultra-thin film [Figure 6.3 (c)], where one would expect perfect extinction according to the Glazer selection rule. A precise determination of the atomic coordinates associated with this tilt pattern is therefore not possible without taking these distortions into account. Nevertheless, the clear suppression of the H=K peak in ultra-thin films indicates that the rotations about the [110] axis are quenched, and the symmetry of the film structure is increased from monoclinic to tetragonal.

From the positions of each split diffraction peak, the lattice parameters of the film unit cell can be obtained. Table 6.1 shows the calculated lattice parameters and unit cell volumes of the 10 UC and 50 UC thick films. For the 20 UC film, the RSMs show evidence for both monoclinic (split peaks with broad in-plane widths) and ultra-thin tetragonal (one peak with narrow in-plane width and broad out-of-plane width) symmetry [Figure 6.1 (b) and (e)], indicating that these two phases coexist at this thickness. Since the monoclinic and tetragonal peak splitting patterns overlap each other, an accurate determination of the peak position was not possible for the 20 UC film. In the 50 UC film [Figure 6.1 (a) and (d)], evidence for the presence of a tetragonal phase can no longer be clearly observed, because the broad peaks originating from the $M_A$ monoclinic structure completely dominate the intensity in

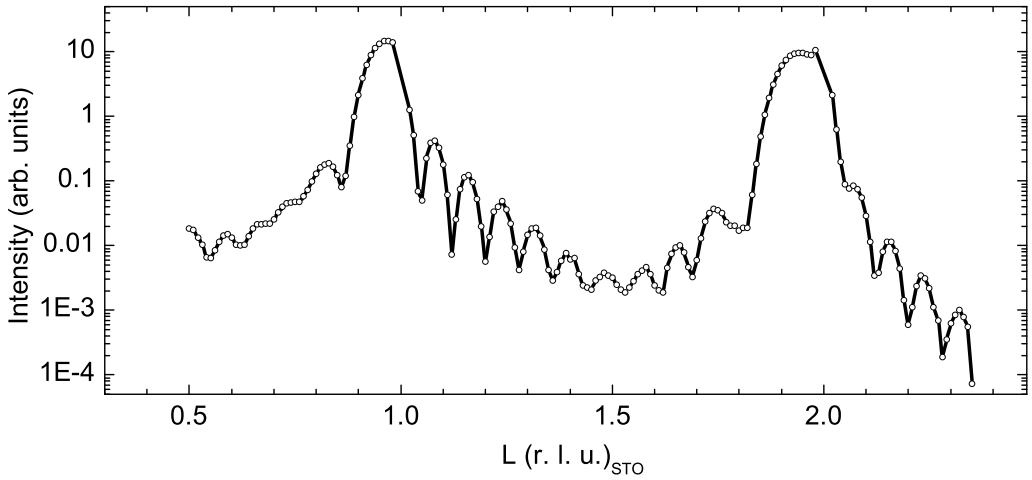


Figure 6.4: Measured specular diffraction 00L intensity for the ultra-thin (10 UC) film. The solid line is a guide to the eye.

the RSM. Thus, it remains unclear if a thin layer with tetragonal symmetry continues to exist at the interface or whether the entire film transitions to the monoclinic structure.

It has been reported that $BiFeO_3$ films grown on (001) $SrTiO_3$ can have a tetragonal structure with a giant c/a ratio, resulting from the higher strain induced by a $Bi_2O_3$ layer, which can be formed between the film and the substrate [8, 9]. Specular diffraction 00L scans have been performed for the ultra-thin film, to check for the presence of $Bi_2O_3$ layers. Pronounced peaks are expected near L = 1.45 and L = 2.15 if such layers exist [9]. As can be seen in Figure 6.4, there are no peaks at these L positions. This excludes the possibility of having unknown crystalline layers being responsible for higher symmetry of the film by introducing additional strain on the film. Therefore, the tetragonal phase observed in the ultra-thin $BiFeO_3$ originates purely from the epitaxy between the film and the substrate.

### 6.2.3 Discussion

In contrast to the previously reported $M_A$-$M_C$-T phase transition of thicker $BiFeO_3$ films as a function of strain or temperature [6, 10], we observed a direct transition from the monoclinic $M_A$ phase to a tetragonal phase as a function of film thickness. This tetragonal phase in ultra-thin films is subject to only moderate strains (-1.4%) from the substrate, and does not exhibit the giant c/a ratio present in the tetragonal $M_C$ and T phases induced by high compressive strain ($<$ -4%). Moreover, as can be seen in Table 6.1, no substantial difference exists between the unit cell volumes of the

50 UC film and the 10 UC film (Note that the volume of the $M_A$ unit cell is doubled with respect to the tetragonal unit cell). Considering the fact that the usual strain-driven monoclinic to tetragonal phase transition involves a significant change in unit cell volume [6, 11], this also supports that our observations are not a conventional strain effect.

These findings suggest that a mechanism other than strain is involved in the phase transition in the ultra-thin regime. Our results favor an alternate explanation where the cubic (001) $SrTiO_3$ substrate with 4-fold in-plane symmetry provides a strong constraint in the octahedral tilting pattern in the $BiFeO_3$ film through corner-connectivity. We note here that several experimental and theoretical studies on the perovskite/perovskite interface have reported that the corner-connectivity between the $BO_6$ octahedra of the substrate and the film at the interface allows the octahedral tilt pattern of the substrate to propagate a few unit cells into the film, thereby determining the symmetry of the film structure [12–14]. For the $BiFeO_3/SrTiO_3$ system, this boundary condition for the corner-connectivity between $SrTiO_3$ (no octahedral tilting) and $BiFeO_3$ may suppress the octahedral tilting about the [110] direction in $BiFeO_3$, resulting in the tetragonal structure for ultra-thin films. Moreover, the absence of the octahedral tilting about *in-plane* axes also indicates that the film has a structure highly coherent with the substrate, explaining the narrow in-plane widths of the 10 UC film Bragg peaks.

## 6.3 $BiFeO_3$ Thin Films Grown on $LaAlO_3$ Substrates

### 6.3.1 Measurements

X-ray diffraction experiments for $BiFeO_3$ films grown on $LaAlO_3$ films were performed at Sector 33-BM-C of the Advanced Photon Source. Similar to the measurements for $BiFeO_3$ grown on $SrTiO_3$, a PILATUS 100K pixel detector was used for measuring 3-dimensional reciprocal space volumes with a combination of rocking scans and L-directional scans.

$LaAlO_3$ substrates generally exhibit several structural domains within the x-ray coherence length, and two or more sharp peaks are observed during the rocking scan around a nominal substrate Bragg peak position. Due to this substrate twinning issue, the orientation matrix of the substrate cannot be accurately determined, which results in significant deviations between the actual HKL positions and the calculated HKL positions. Due to this deviations, typically the peaks appear at the positions slightly [on the order of $10^{-3}$ in r. l. u.] off from the exact integer positions in RSMs.

Moreover, the $BiFeO_3$ films are epitaxially grown on these tilted substrate domains, which may result in an unwanted splitting of the film Bragg peaks as well. Fortunately, these issues are not so critical in determining the unit-cell symmetry of a film because it can be done by qualitatively interpreting the Bragg peak splitting pattern. However, caution should be exercised in this case to distinguish the peak splitting which originates from the substrate imperfection and the one which emerges from the film symmetry. If the film has a monoclinic ($M_C$ or $M_A$) symmetry, the film Bragg peaks are supposed to be split mainly along the L direction, and the spacing (measured in substrate r. l. u.) between the split peaks should increase as a function of the magnitude of **q** vector projected onto the HK plain ($q_{||}$). Therefore, the RSMs of several peaks along high-symmetry directions with different $q_{||}$ values were measured to verify the monoclinic symmetry of the film.

Since the 5 nm $BiFeO_3$ film on a $LaAlO_3$ substrate exhibits an $M_A$ monoclinic structure at room temperature (RT) [15], two thinner films (4 nm, 2.4 nm) were measured to examine the presence of additional phase transition in the ultra-thin regime. In addition, to check if the room temperature $M_A$ phase results from a totally new mechanism or whether it is just a lower transition temperature version of the usual $M_C$-$M_A$-T system, the sample is cooled down to 30 K using a cryostat while measuring RSMs.

Note that all the RSMs for $BiFeO_3/LaAlO_3$ results are arbitrarily scaled to provide the best contrast, and all reciprocal space positions in the figures are given in units of the inverse substrate (pseudocubic $LaAlO_3$) lattice constants.

### 6.3.2 Results and Discussion

#### 6.3.2.1 Thickness-Induced Phase Transition

Figures 6.5 and 6.6 show HL slices and (HH)L slices through H03 (H=1, 2, 3, 4) and HH3 peaks (H=1, 2, 3), respectively. For the 4 nm $BiFeO_3$ film, the peak splitting is observed mainly along the L-direction, and there is a clear trend with an increasing separation between split peaks as a function of $q_{||}$, with 3-fold splitting for HH3 peaks and 2-fold splitting for H03 peaks. This indicates that the 4 nm film still exhibits the $M_A$ monoclinic structure. For the 2.4 nm film, however, a totally different behavior is observed. Apart from the peaks being elongated in L-direction, which is expected for thinner films, there is no clear 2-fold or 3-fold splitting observed in any RSMs, and also the shape of the peak is relatively consistent for all $q_{||}$ values. Similar to the moderately strained $BiFeO_3$ thin films grown on $SrTiO_3$ thin films,

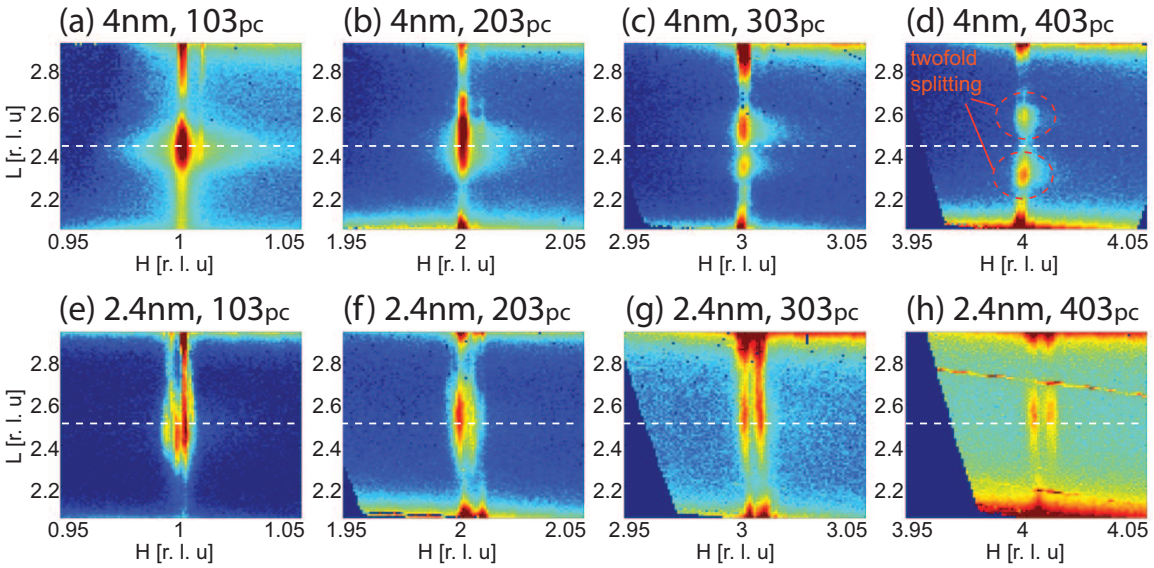


Figure 6.5: (a)-(d) HL map of the H03$_{pc}$ (H=1, 2, 3, 4; the subscript pc refers to pseudo-cubic) peaks of the 4 nm $BiFeO_3$ film. (e)-(h) HL map of the H03$_{pc}$ peaks for the 2.4 nm $BiFeO_3$ film. Note that the peak splitting in the lateral direction (H or K direction) is due to the imperfection of the substrate, not to the film symmetry. Dashed white lines are guides for the eye.

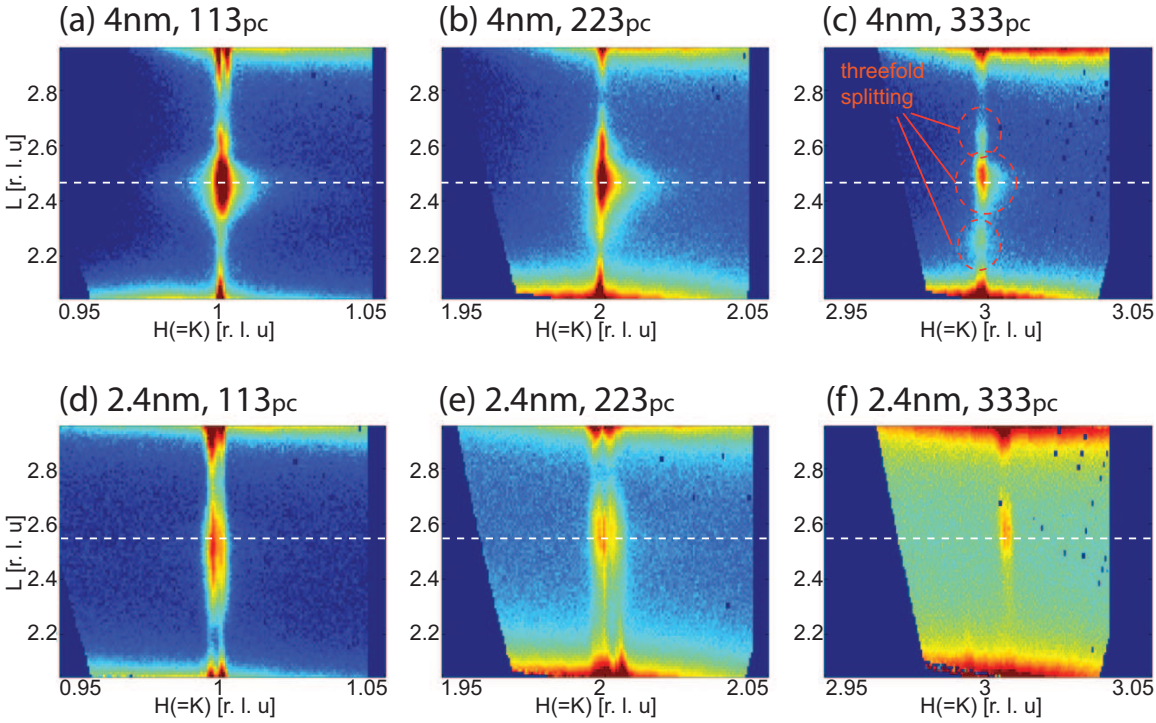


Figure 6.6: (a)-(c) (HH)L map of the HH3$_{pc}$ peak (H=1, 2, 3) for the 4 nm $BiFeO_3$ film. (d)-(f) HL map of the HH3$_{pc}$ peaks for the 2.4 nm $BiFeO_3$ film. Dashed white lines are guides for the eye.

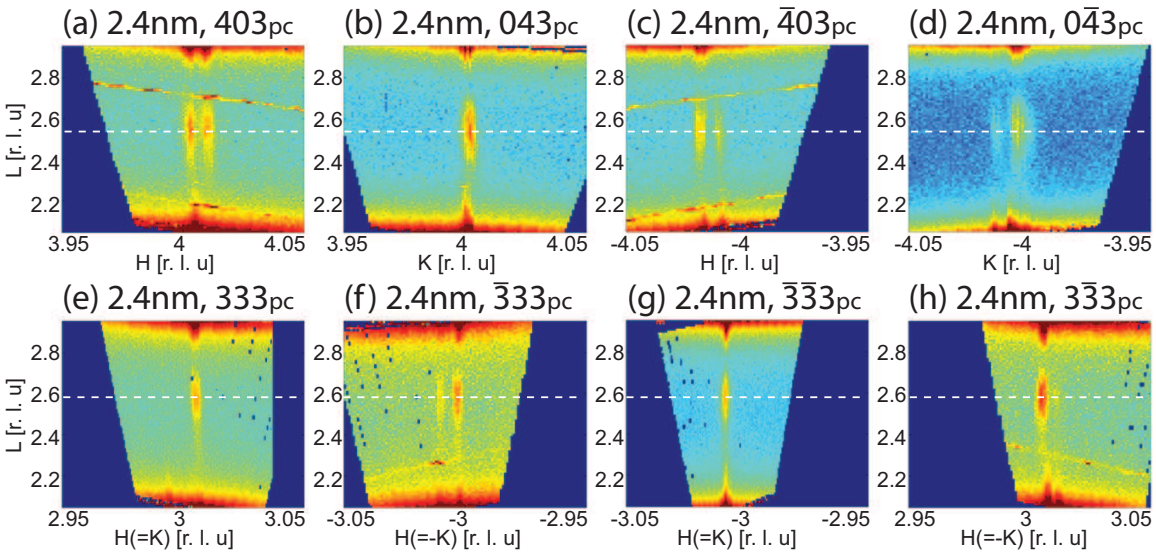


Figure 6.7: RSMs of four-fold symmetrically equivalent film Bragg peaks for the ultra-thin (2.4 nm) film. Both the 403 (top row) and 333 (bottom row) family of peaks are shown. (a) HL map around the 403 peak (b) KL map around the 043 peak (c) HL map around the $\bar{4}$03 peak (d) KL map around the 0$\bar{4}$3 peak (e) (HH)L map of the 333 peak (f) (H$\bar{\text{H}}$)L map of the $\bar{3}$33 peak (g) (HH)L map of the $\bar{3}\bar{3}$3 peak (h) (H$\bar{\text{H}}$)L map of the 3$\bar{3}$3 peak. Dashed white lines are guides for the eye.

this highly-strained $BiFeO_3$ films grown on $LaAlO_3$ also show the disappearance of the peak splitting in the ultra-thin regime.

Again, this can be explained either by a single-domain monoclinic structure or a tetragonal structure. In order to confirm the symmetry of the film, four-fold symmetrically equivalent peaks are plotted in Figure 6.7. The L positions of the symmetrically equivalent peaks are consistent for all four symmetry equivalents, and this determines the unit cell symmetry of the 2.4 nm film to be tetragonal.

Note that the L-position of the film Bragg peaks are very similar for all samples regardless of the film symmetry. As can be seen in Figure 6.5, the 103 peaks of the ultra-thin tetragonal film and the thicker monoclinic film both appear in the RSM at around L=2.5 in terms of substrate reciprocal lattice unit. This means that the ultra-thin tetragonal film also shows a giant c/a ratio, which can usually be observed for highly strained $BiFeO_3$ films.

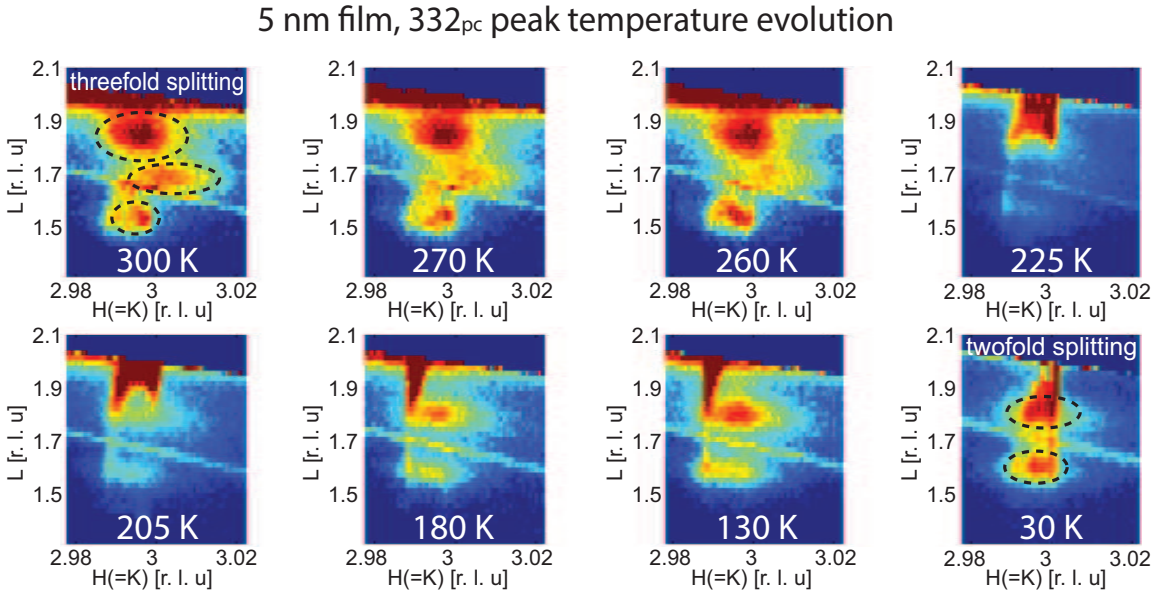


Figure 6.8: The evolution of the $332_{pc}$ peak splitting pattern for 5 nm of $BiFeO_3$ on $LaAlO_3$ [(HH)L maps], during the cooling from RT (300 K) down to 30 K. The sharp needle-like features between the split peaks are powder rings from the metal contact on the surface, and they are not related to the film structure.

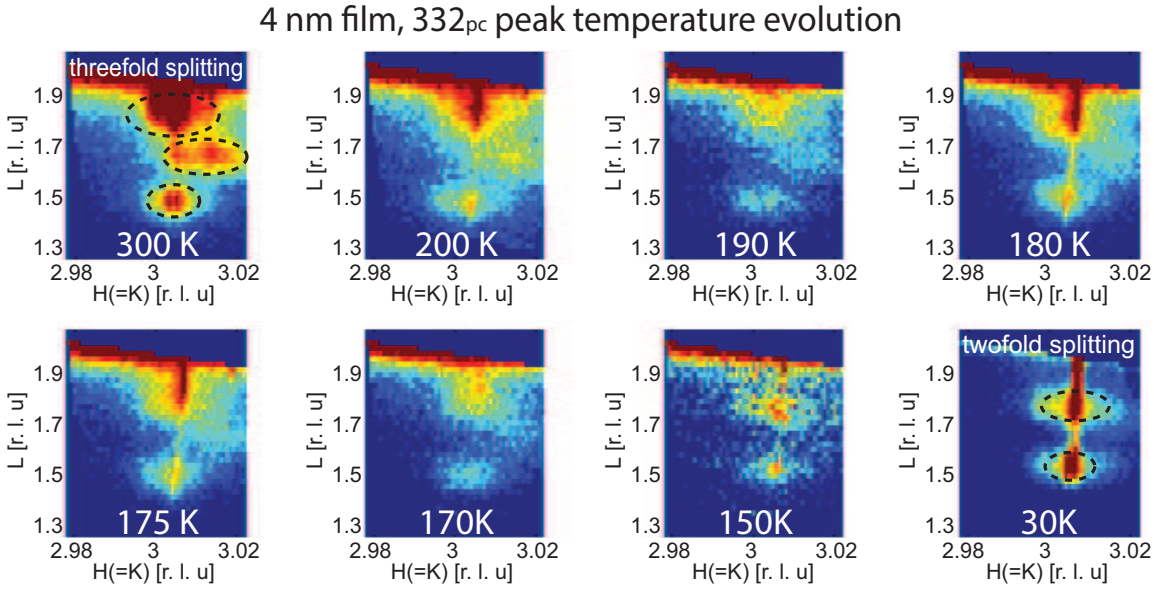


Figure 6.9: The evolution of the $332_{pc}$ peak splitting pattern for 4 nm of $BiFeO_3$ on $LaAlO_3$ [(HH)L maps], during the cooling from RT down to 30 K.

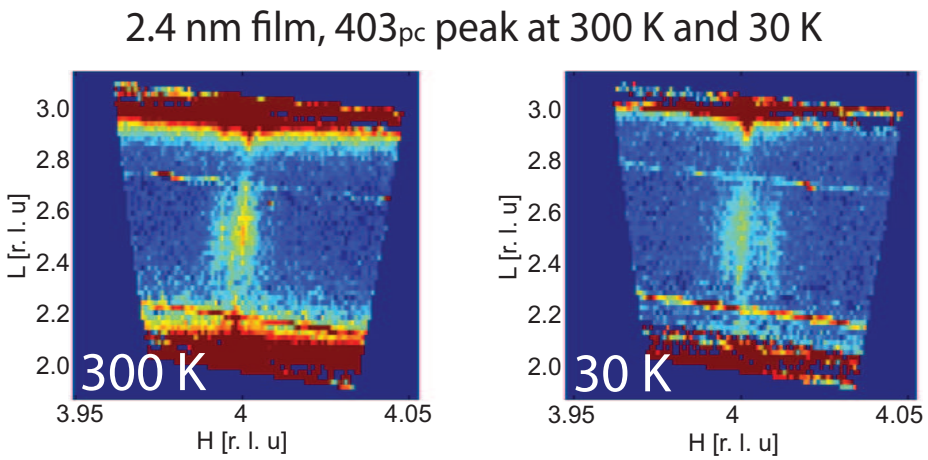


Figure 6.10: Comparison of the peak splitting pattern for $403_{pc}$ peak (HL map) of a ultra-thin (2.4 nm) $BiFeO_3$ on $LaAlO_3$ at RT and at 30 K.

#### 6.3.2.2 Temperature-Induced Phase Transition

Figures 6.8 and 6.9 show the evolution of the peak splitting pattern for the $332_{pc}$ peak from films with 5 nm and 4 nm thickness, while cooling the sample down to 30 K. Both the 5 nm and 4 nm films show a 3-fold peak splitting pattern for the 332 peak at room temperature, indicating an $M_A$ structure. When the sample is cooled down, both of the films are experiencing phase transitions and the peaks are 2-fold split (corresponding to $M_C$) at 30 K. Therefore, the room-temperature $M_A$ phase, which can be observed in $BiFeO_3/LaAlO_3$ systems below 7 nm film thickness, is essentially the same phase as that of the thicker films, apart from the fact that they have much lower transition temperatures. The 5 nm film shows a slightly higher $M_C$ to $M_A$ transition temperature (between 200 K and 250 K) compared to that of the 4 nm film (between 150 K and 175 K), which is also consistent with the result shown in Figure 3.8 which suggests lower transition temperatures for thinner samples.

Surprisingly, for the ultra-thin tetragonal film, no difference is observed between the peak splitting pattern at 30 K and the one at room temperature (see Figure 6.10). This is interesting because a structural phase transition from tetragonal to monoclinic symmetry is expected upon cooling, considering the typical $M_C$-$M_A$-T transition induced by temperature. This may indicate that this thickness-induced tetragonality originates from a mechanism totally different from the temperature-induced tetragonality which can be observed from thicker samples. Additional studies are needed to confirm this, because temperatures lower than 30 K were not accessible during these measurements and there is still a possibility of the transition temperatures being lower than 30 K.

# Bibliography


[1] Y. Yang, C. M. Schlepütz, C. Adamo, D. G. Schlom, and R. Clarke, "Untilting $BiFeO_3$: The influence of substrate boundary conditions in ultra-thin $BiFeO_3$ on $SrTiO_3$," *APL Materials* **1**, 052102 (2013).

[2] P. Kraft, A. Bergamaschi, C. Broennimann, R. Dinapoli, E. F. Eikenberry, B. Henrich, I. Johnson, A. Mozzanica, C. M. Schlepütz, P. R. Willmott, and B. Schmitt, "Performance of single-photon-counting PILATUS detector modules," *J.Synchrotron Rad.* **16**, 368 (2009).

[3] C. M. Schlepütz, R. Herger, P. R. Willmott, B. D. Patterson, O. Bunk, C. Brönnimann, B. Henrich, G. Hülsen, and E. F. Eikenberry, "Improved data acquisition in grazing-incidence X-ray scattering experiments using a pixel detector," *Acta Crystallogr. A* **61**, 418 (2005).

[4] C. M. Schlepütz, S. O. Mariager, S. A. Pauli, R. Feidenhans'l, and P. R. Willmott, "Angle calculations for a (2+3)-type diffractometer: focus on area detectors," *J. Appl. Crystallogr.* **44**, 73 (2011).

[5] Z. Chen, Z. Luo, C. Huang, Y. Qi, P. Yang, L. You, C. Hu, T. Wu, J. Wang, C. Gao, T. Sritharan, and L. Chen, "Low-Symmetry Monoclinic Phases and Polarization Rotation Path Mediated by Epitaxial Strain in Multiferroic $BiFeO_3$ Thin Films," *Adv. Funct. Mater.* **21**, 133 (2011).

[6] H. Christen, J. Nam, H. Kim, A. Hatt, and N. Spaldin, "Stress-induced R-$M_A$-$M_C$-T symmetry changes in $BiFeO_3$ films," *Phys. Rev. B* **83**, 144107 (2011).

[7] A. M. Glazer, "Simple ways of determining perovskite structures," *Acta Crystallogr. A* **31**, 756 (1975).

[8] H. Liu, P. Yang, K. Yao, and J. Wang, "Growth rate induced monoclinic to tetragonal phase transition in epitaxial $BiFeO_3$ (001) thin films," *Appl. Phys. Lett.* **98**, 102902 (2011).

[9] H. Liu, P. Yang, K. Yao, K. P. Ong, P. Wu, and J. Wang, "Origin of a Tetragonal $BiFeO_3$ Phase with a Giant c/a Ratio on $SrTiO_3$ Substrates," *Adv. Funct. Mater.* **22**, 937 (2012).

[10] W. Siemons, M. D. Biegalski, J. H. Nam, and H. M. Christen, "Temperature-Driven Structural Phase Transition in Tetragonal-Like $BiFeO_3$," *Appl. Phys. Express* **4**, 095801 (2011).

[11] H. Béa, B. Dupé, S. Fusil, R. Mattana, E. Jacquet, B. Warot-Fonrose, F. Wilhelm, A. Rogalev, S. Petit, V. Cros, A. Anane, F. Petroff, K. Bouzehouane, G. Geneste, B. Dkhil, S. Lisenkov, I. Ponomareva, L. Bellaiche, M. Bibes, and A. Barthélémy, "Evidence for Room-Temperature Multiferroicity in a Compound with a Giant Axial Ratio," *Phys. Rev. Lett.* **102**, 217603 (2009).

[12] A. Y. Borisevich, H. J. Chang, M. Huijben, M. P. Oxley, S. Okamoto, M. K. Niranjan, J. D. Burton, E. Y. Tsymbal, Y. H. Chu, P. Yu, R. Ramesh, S. V. Kalinin, and S. J. Pennycook, "Suppression of Octahedral Tilts and Associated Changes in Electronic Properties at Epitaxial Oxide Heterostructure Interfaces," *Phys. Rev. Lett.* **105**, 087204 (2010).

[13] S. H. Chang, Y. J. Chang, S. Y. Jang, D. W. Jeong, C. U. Jung, Y.-J. Kim, J.-S. Chung, and T. W. Noh, "Thickness-dependent structural phase transition of strained $SrRuO_3$ ultrathin films: The role of octahedral tilt," *Phys. Rev. B* **84**, 104101 (2011).

[14] J. M. Rondinelli and N. A. Spaldin, "Substrate coherency driven octahedral rotations in perovskite oxide films," *Phys. Rev. B* **82**, 113402 (2010).

[15] W. Siemons, C. Beekman, and H. M. Christen, Private communication.

# CHAPTER VII

# Conclusions and Outlook

In this dissertation, the surface and interface structures of ZnO Schottky contacts and the unit-cell symmetry of epitaxial $BiFeO_3$ thin films were investigated.

Surface x-ray diffraction has shown that the atomic structure of uncoated and metal-coated ZnO (0001) Zn-polar surfaces prepared under typical device fabrication conditions has a bulk-like termination with no significant atomic relaxations. Most interestingly, a stable (1×1) overlayer of oxygen atoms on top of the terminating zinc atoms was observed, consistent with XPS measurements but at odds with DFT calculations. At uncoated surfaces, this (1×1) oxygen overlayer is most likely associated with the presence of hydroxyl (OH) groups. Significantly, no structural changes occur and the (1×1) oxygen overlayer remains in place following the fabrication of both plain and oxidized metal Schottky contacts [1].

ZnO $(000\bar{1})$ O-polar samples show decreased layer spacings between the topmost oxygen and zinc layers compared to the bulk value, and exhibit Gaussian roughness profiles with about 1.5 unit cells FWHM. Except for $AgO_x$-coated samples, which show about 1/3 of a ML of oxygen vacancies at the ZnO surface, all samples are 1×1 terminated with full occupations. In general, we observe that the conducting over-layers have only a subtle effect on the ZnO surface atomic displacements. This finding, also mirrored in the reported results for the Zn-polar face [1], is somewhat surprising given the polar nature of ZnO [2].

The atomic structure of ZnO polar surfaces and Schottky interfaces are accurately determined from this study. Clearly, it would be very useful to have detailed theoretical simulations of the Schottky junction property based on this results. This would establish a relation between the transport behavior at the Schottky contact and the atomic structure of the interface, eventually allowing precise control of the electronic properties of this material via proper choice of the surface treatment.

The non-polar surfaces [a-plane: $(11\bar{2}0)$, m-plane: $(10\bar{1}0)$] of ZnO are also being considered as potential candidates for Schottky applications, and thorough structural studies on these surfaces would contribute to a deeper understanding of this material.

The structural symmetry of ultra-thin $BiFeO_3$ films on (001) $SrTiO_3$ substrates was determined from 3D-RSM measurements. The evolution of the film Bragg peak splitting and the half-order intensities associated with oxygen octahedra rotations definitively demonstrate that a structural phase transition exists from the monoclinic $M_A$ phase to a tetragonal symmetry as a function of film thickness. This monoclinic-to-tetragonal transition is accompanied by the evolution of the half-order diffraction peaks, which reflects untilting of the oxygen octahedra around the [110] axis, proving that the octahedral tilting is closely correlated with the transition. This structural change is thickness-dependent, and different from a strain-induced transition in the conventional sense [3].

A similar monoclinic-to-tetragonal phase transition was observed on ultra-thin highly-strained $BiFeO_3$ films grown on pseudocubic (001) $LaAlO_3$ substrates. It is also verified that the room temperature $M_A$ phase observed from moderately thin samples is still within the typical $M_C$-$M_A$-T phase diagram, and the $M_C$ structure can be recovered by cooling the sample below room temperature. Interestingly, an ultra-thin tetragonal $BiFeO_3$ film did not show any structural phase transition above 30 K.

Further investigations on ultra-thin $BiFeO_3$ films on different substrates are needed to better understand the interplay between structure, film thickness, and the misfit strain. Having established the structural symmetry, a complete determination of the atomic structure, including the oxygen octahedra tilt angles, can be obtained as a function of the strain and thickness by quantitative analysis of crystal truncation rod and half-order peak intensities.

## Bibliography

[1] C. M. Schlepütz, Y. Yang, N. S. Husseini, R. Heinhold, H.-S. Kim, M. W. Allen, S. M. Durbin, and R. Clarke, "The presence of a (1×1) oxygen overlayer on ZnO(0001) surfaces and at Schottky interfaces," *J. Phys.: Condens. Matter* **24**, 095007 (2012).

[2] Y. Yang, C. M. Schlepütz, F. Bellucci, M. W. Allen, S. M. Durbin, and R. Clarke, "Structural investigation of ZnO O-polar $(000\bar{1})$ surfaces and Schottky interfaces," *Surf. Sci.* **610**, 22 (2013).

[3] Y. Yang, C. M. Schlepütz, C. Adamo, D. G. Schlom, and R. Clarke, "Untilting $BiFeO_3$: The influence of substrate boundary conditions in ultra-thin $BiFeO_3$ on $SrTiO_3$," *APL Materials* **1**, 052102 (2013).

# APPENDICES

# APPENDIX A

# Typical Orientation Matrix Determination Procedure

The orientation matrix can be obtained in two different ways which are described in [1]:

(1) When the crystal lattice constants and the x-ray wavelength are accurately given, finding the directions of two linearly independent Bragg peaks of known HKL indices determines the orientation matrix.

(2) Finding the angular positions of three linearly independent Bragg peaks (or even more than three; in this case, at least three peaks should be linearly independent) can determine the orientation matrix without using the wavelength or the lattice constant information.

For easier sample alignment for surface diffraction experiments, it is preferable to define the unit cell of the sample crystal such that the (001) direction of the unit cell is along the sample surface normal. Also, in this study, all the sample substrates are prepared to be low miscut ($< 0.1^\circ$), which is the angular discrepancy between the crystallographic (001) direction and the optical surface normal. Therefore, when the diffractometer $z$ axis is aligned with the sample surface normal (laser alignment), the (001) axis of the crystal is also very close to the $z$ axis. The most significant unknown is the orientation of the (100) direction of the crystal relative to the $x$ axis of the diffractometer (azimuthal orientation). Since the lattice constant of the substrates, the x-ray wavelength, and the (001) direction of the sample are known with good accuracy, the calculated diffractometer angles of a given non-specular [not parallel to (001)] substrate Bragg peak will have a significant offset only in the azimuthal rotation, and all the other angles should be close to the actual value. Therefore,

while monitoring the diffraction intensity at the detector, the sample can be rotated around the azimuthal axis until the strong Bragg peak intensity is observed. Accurate angular positions for the Bragg peak can be found by fine-tuning the diffractometer angles until the maximum intensity is achieved. Once the (001) direction and one off-specular reflection is found, the orientation matrix can be determined using method (1) described above.

Since the lattice constants or x-ray wavelength may be different from the nominal values if the substrate is prepared in a different condition or the monochromator at the beamline has a calibration error, it is safer to use method (2) for determining the orientation matrix. Nevertheless, the matrix obtained with method (1) should still be quite close to the actual one, and the calculated angular positions of many other Bragg peaks based on the matrix will be very close to the actual peak positions. Therefore, fine-tuning of the diffractometer angles near the calculated peak positions of several Bragg peaks is the only necessary step, and an accurate orientation matrix can be determined by an unweighted chi-square fitting of the measured angular positions of Bragg peaks [1, 2].

## Bibliography


[1] W. R. Busing and H. A. Levy, "Angle calculations for 3- and 4-circle X-ray and neutron diffractometers," *Acta Crystallogr.* **22**, 457 (1967).

[2] R. L. Ralph and L. W. Finger, "A computer program for refinement of crystal orientation matrix and lattice constants from diffractometer data with lattice symmetry constraints," *J. Appl. Crystallogr.* **15**, 537 (1982).

# APPENDIX B

# Determination of Optimal Control Parameters for Genetic Algorithms

Two user-selectable control parameters are involved in differential evolution algorithms. They are the mutation constant $k_m$ and the recombination constant $k_r$ [1]. During the fitting process, each individual of the next generation will be constructed based on the parent individual, the one which has the lowest FOM and two other randomly selected individuals. These mutation and recombination parameters determine how much randomness will be added into the parent individual to form the next generation. This randomness allows the genetic algorithm to search a large volume in the parameter space; this reduces the probability of being trapped in local minima. If not enough randomness is involved, the fit can easily be trapped in a local minimum, and if too much randomness is involved, the fitting will take too much time to converge to a solution. Therefore, appropriate $k_m$ and $k_r$ values are required to successfully utilize the genetic algorithm. Ideal $k_m$ and $k_r$ values depend on the system being modeled and the FOM used for fitting. Hence, before starting to use genetic algorithms for a system with a given FOM, proper $k_m$ and $k_r$ values should be established.

Since randomness is involved in every evolution to the next generation, the genetic algorithm is not deterministic. Taking advantage of the indeterministic nature of the algorithm, the reliability of a particular $k_m$ and $k_r$ combination can be checked by running the same fit several times and comparing the convergence ratio of obtaining the same solution. To determine the ideal combination of $k_m$ and $k_r$, both the convergence ratio to the lowest FOM (reliability of fitting) and the number of generations required for converging to the best solution (speed of fitting) should be considered.

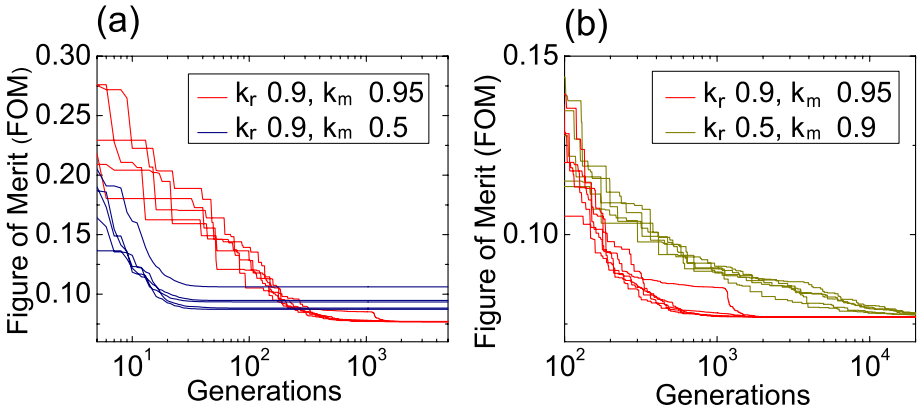


Figure B.1: Comparison between the FOM evolution as a function of generation for three different combinations of $k_m$ and $k_r$. A logarithmic FOM [Equation (4.3)] was used in all cases. (a) With ($k_r$=0.9, $k_m$=0.95), 5/5 fits converged to the lowest solution within approximately 1,500 generations, but with ($k_r$=0.9, $k_m$=0.5), all fittings seem to be stuck in local minima within 50 generations and none of the them converged to the lowest FOM solution. (b) With ($k_r$=0.5, $k_m$=0.9), 5/5 fits seem to be converging to the lowest solution, but have not completely converged even after 20,000 generations.

Figure B.1 shows the different convergence behavior for three combinations of $k_m$ and $k_r$ for fitting a ZnO CTR dataset with five independent trials for each set. Figure B.1 (a) compares a combination with ($k_r$=0.9, $k_m$=0.95) to another one with ($k_r$=0.9, $k_m$=0.5). For ($k_r$=0.9, $k_m$=0.95), shown by the red curves, all five independent fits converge to a single solution after about 1500 generations. For ($k_r$=0.9, $k_m$=0.5), drawn in blue curves, all five trials converge to some solution after about 50 generations. All of them, however, are stuck at local minima and not able to approach the lowest solution found with ($k_r$=0.9, $k_m$=0.95). Using ($k_r$=0.9, $k_m$=0.5) therefore is definitely not a good choice of parameters, because it does not provide enough randomness to avoid trapping in local minima. The yellow curve in Figure B.1 (b) shows the fitting behavior for ($k_r$=0.5, $k_m$=0.9). In this case, all five trials seems to converge toward the lowest solution found with ($k_r$=0.9, $k_m$=0.95). However, the evolution is too slow and has not yet fully converged even after 10,000 generations. This means that too much randomness is involved with this combination to achieve an efficient convergence behavior. Various combinations of $k_r$ and $k_m$ values were tried for this test, and combinations with ($k_r$=0.7, $k_m$=0.8) and ($k_r$=0.9, $k_m$=0.95) are found to be the best in terms of speed and reliability for the ZnO CTR fitting. It generally takes about 24 hours for ten independent ZnO CTR fits to converge with

those parameter combinations, and usually almost all of them converge to the same solution with the lowest FOM of any achieved solution.

## Bibliography

[1] M. Björck and G. Andersson, "GenX: an extensible X-ray reflectivity refinement program utilizing differential evolution," *J. Appl. Crystallogr.* **40**, 1174 (2007).

# APPENDIX C

## Error Bar Estimation in Genetic Algorithms

In the model fitting process, several parameters are fitted simultaneously. To determine the error bar of each fitted parameter, the correlation between the fit parameters should be considered. Some fitting algorithms, such as the Levenberg-Marquardt algorithm, provide the correlated error bar estimation. Those fits, however, work only for a least-square FOM. Since our data extend over six orders of magnitudes ($10^{-2}$-$10^{4}$) in intensity, the datapoints in the strong signal region would have significantly more weight than those datapoints with weak signals. To put similar weights on datapoints with strong and weak signals, the FOM should be based on a logarithmic function of the diffraction amplitude [1]. In the process of genetic algorithm fitting, numerous random combinations of the fitting parameters form the individuals of each generation, and each individual carries the information about the FOM for its own parameter combination. Thus, thousands of points in parameter space are sampled during the course of a fit, and information on the parameter landscape can be extracted by surveying the history of the fit. All individual parameter sets created during the fit process contain the correlation information between parameters because each individual has different random values for all parameters. Figure C.1 (a) and (b) show the individual map and simulation of FOM as functions of atomic displacement and the occupation of the oxygen atom in the topmost double-layer of the ZnO Zn-polar (0001) surface sample (sample 4 in Table 3.1) respectively. The horizontal red line indicates a 5% increase in the FOM with respect to the best solution, which is the common value used in the literature for the error bar estimation of fitted parameters [2]. As can be seen in Figure C.1 (b), taking into account the correlations between parameters produces larger error bars than the calculation without considering the correlations.

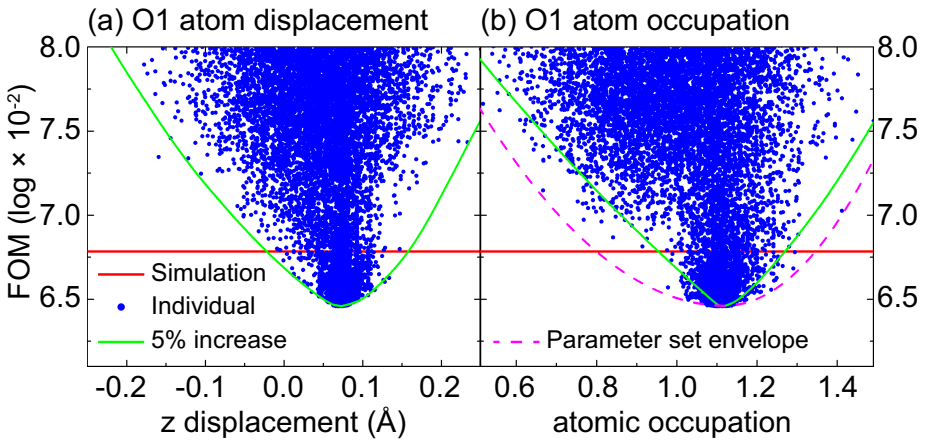


Figure C.1: Error bar estimation diagram. Blue dots represent the FOM value for each individual parameter set used during the entire fitting process, and the green line shows the calculated FOM by changing only one parameter with all other parameters fixed at their best values. (a) Error bar estimation of the atomic displacement of O1 (oxygen atom in topmost double-layer). The green curve and the envelope around the set of blue dots agree well with each other, which means that this parameter is not significantly correlated with other parameters. (b) Error bar estimation of the atomic occupation of O1. Obviously, the envelope around the blue dots (pink dashed line) covers a larger range of layer occupation within the 5% increase in the FOM, which means that this parameter is more significantly correlated with other parameters.

# Bibliography

[1] M. Wormington, C. Panaccione, K. M. Matney, and D. K. Bowen, "Characterization of structures from X-ray scattering data using genetic algorithms," *Phil. Trans. R. Soc. Lond. A* **357**, 2827 (1999).

[2] D. P. Kumah, J. W. Reiner, Y. Segal, A. M. Kolpak, Z. Zhang, D. Su, Y. Zhu, M. S. Sawicki, C. C. Broadbridge, C. H. Ahn, and F. J. Walker, "The atomic structure and polarization of strained $SrTiO_3$/Si," *Appl. Phys. Lett.* **97**, 251902 (2010).

# APPENDIX D

## Peak Splitting Patterns and Crystal Symmetries

During the growth of epitaxial thin films, the substrate lattices apply strong constraints on the orientation of in-plane axes of the film. Out-of-plain axes of the film, however, are not constrained by the epitaxy, and this can result in several structural domains with different out-of-plane axis orientations. The unit-cell symmetry of these films cannot be determined by conventional single-crystal diffraction or powder diffraction techniques because the film crystals are neither a uniformly oriented single-crystal nor a randomly oriented poly-crystal.

In a real measurement, the diffraction patterns of each structural domain overlap with each other, typically resulting in Bragg peak splitting. By examining this peak splitting, the unit-cell symmetries of the films can be determined. In the following discussion, the relation between the peak splitting pattern and the unit-cell symmetry of the film will be introduced for the case of films grown on cubic or tetragonal substrates ($\mathbf{a}$, $\mathbf{b}$, and $\mathbf{c}$ are orthogonal to each other, and $\mathbf{a} = \mathbf{b}$).

If the substrates have a cubic or tetragonal structure, thin films grown epitaxially on these substrates are confined to have orthogonal in-plane lattice vectors with the same length. This allows only three crystal symmetries for the film: cubic, tetragonal, and monoclinic. Figure D.1 shows the possible crystal structures and corresponding diffraction patterns for single-domain cases. Figure D.1 (a) describes the case of films having cubic or tetragonal symmetry. In real space, the $\mathbf{c}$ lattice vector is perpendicular to the $\mathbf{a}$ and $\mathbf{b}$ vectors, which results in H and K axes perpendicular to the L axis in reciprocal space [see Equation (2.23)]. The film can also have an $\mathrm{M}_A$ monoclinic structure for which the $\mathbf{c}$ lattice vector is parallel to the $[uuv]_{pc}$ $(u < v)$ direction [1]. Here, the subscript pc denotes *pseudocubic*. In this case, as can be seen in Figure D.1 (b), the HK-plane of the reciprocal lattice rotates around the $[\mathrm{H}\overline{\mathrm{H}}0]_{pc}$

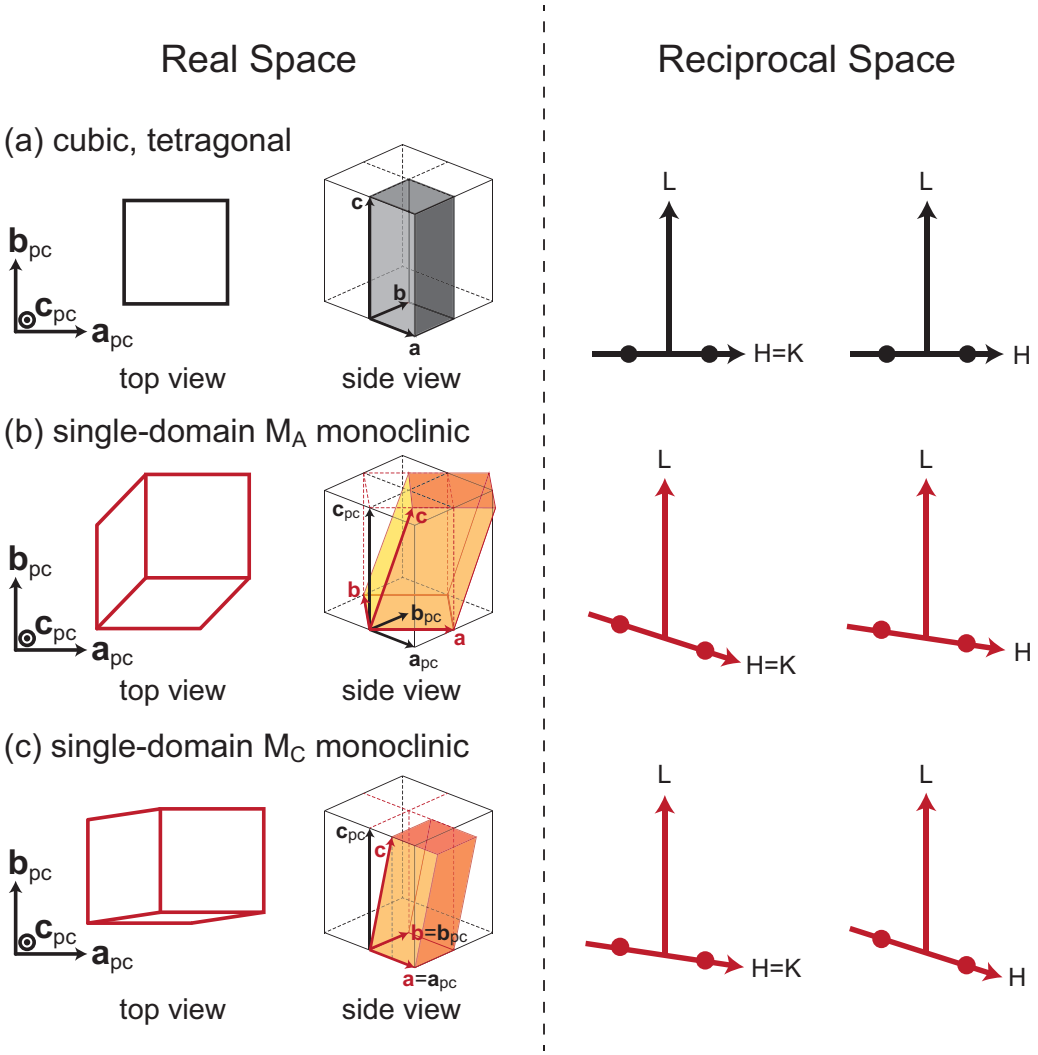


Figure D.1: Relation between the diffraction pattern and unit-cell symmetry of single-domain films. (a) cubic or tetragonal structure (b) $M_A$ monoclinic structure (c) $M_C$ monoclinic structure.

axis, and the diffraction pattern becomes tilted with respect to that of the tetragonal structure. As described in the figure, the $HHL_{pc}$ peaks are tilted most significantly, and the $H0L_{pc}$ and $0KL_{pc}$ peaks are also tilted, but to a lesser degree. Lastly, the film can exhibit an $M_C$ monoclinic structure with the **c** lattice vector parallel to the $[u0v]_{pc}$ or $[0uv]_{pc}$ direction. Figure D.1 (c) shows the diffraction pattern in this case, and the $H0L_{pc}$ and $0KL_{pc}$ peaks are fully tilted while the $HHL_{pc}$ peaks are only partially tilted.

Based on this information, the unit-cell symmetry of single-domain films can be determined from the diffraction pattern. If all the peaks at four-fold symmetrically equivalent positions of in-plane rotation (for example, $H0L_{pc}$, $0HL_{pc}$, $\overline{H}0L_{pc}$, and $0\overline{H}L_{pc}$ peaks) are at the same L position in the orthogonal reference frame, the film

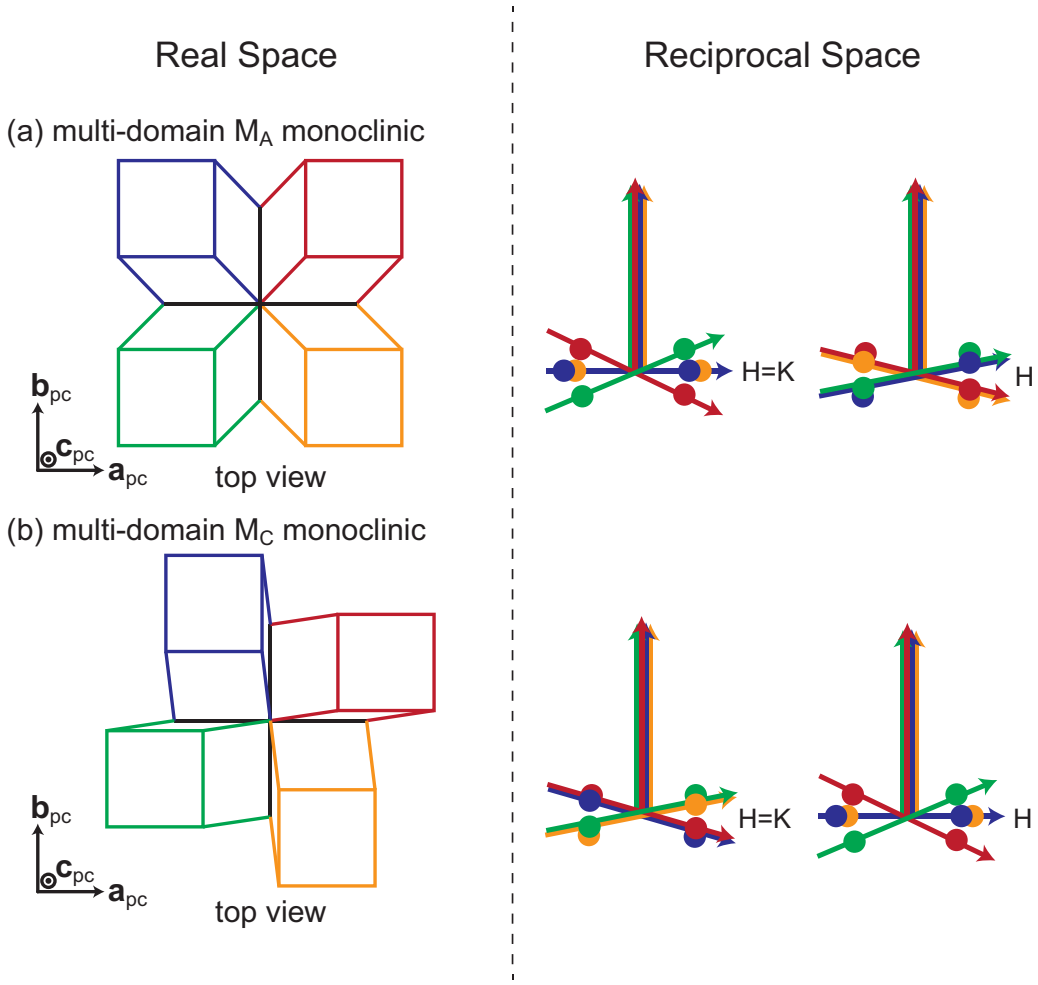


Figure D.2: Relation between the diffraction pattern and unit-cell symmetry of multi-domain films. (a) In case of $M_A$ monoclinic structure (b) In case of $M_C$ monoclinic structure.

possesses cubic or tetragonal symmetry. If the L positions of peaks are different from each other, the film has $M_A$ or $M_C$ monoclinic symmetry. The $M_A$ and $M_C$ structure can be distinguished by examining the difference between the L positions of peaks that are rotated by 180° with respect to each other. For films with $M_A$ symmetry, the L difference between $\{HHL\}_{pc}$ peaks is larger than that of $\{H0L\}_{pc}$ peaks, and for $M_C$ symmetry, the difference between $\{H0L\}_{pc}$ peaks is larger than that of $\{HHL\}_{pc}$ peaks.

Now, let us consider films with multiple structural domains. Films with tetragonal symmetry cannot have multiple domains because there is only one orientation possible due to the epitaxial constraint (**a** and **b** lattice vectors must be along the in-plane).

For $M_A$ monoclinic films [Figure D.2 (a)], four different orientations of the mon-

oclinic domains are possible: the **c** lattice vector is parallel to either of the $[uuv]_{pc}$, $[u\overline{u}v]_{pc}$, $[\overline{u}\overline{u}v]_{pc}$, and $[\overline{u}uv]_{pc}$ directions ($v > u > 0$). As discussed in the single-domain case, the $HHL_{pc}$ (H>0) peak from the domains with **c** parallel to $[uuv]_{pc}$ (red color) is displaced downward with respect to the peak positions of the orthogonal reciprocal lattice (cubic, tetragonal). The diffraction pattern of the domains with **c** parallel to $[\overline{u}\overline{u}v]_{pc}$ (green color) is tilted the opposite way, and the $HHL_{pc}$ (H>0) peaks from these domains are displaced upward. Domains with **c** parallel to $[u\overline{u}v]_{pc}$ (yellow) or $[\overline{u}uv]_{pc}$ (blue) are not tilted with respect to the $[uuv]_{pc}$ direction, and therefore the peaks from these domains stay at the peak positions for orthogonal reciprocal lattices. Hence, as can be seen in the reciprocal space part of Figure D.2 (a), $HHL_{pc}$ peaks become threefold split. $\overline{H}\overline{H}L_{pc}$ peaks are also threefold split, but in this case, the peaks from the red domain displace upward and those from the green domain displace downward. On the other hand, the $H0L_{pc}$ (H>0) peaks are twofold split, because the peaks from red and yellow domains are displaced slightly downward and overlap each other, and those from blue and green domains are displaced slightly upward and overlap each other. Thus, for multi-domain $M_A$ monoclinic films, all $HHL_{pc}$ and $\overline{H}HL_{pc}$ peaks are threefold split, and all $H0L_{pc}$ and $0KL_{pc}$ peaks are twofold split.

Exactly the opposite peak splitting behavior can be observed from multi-domain $M_C$ films. In this case, as can be seen in Figure D.2 (b), all $HHL_{pc}$ and $\overline{H}HL_{pc}$ peaks are twofold split, and all $H0L_{pc}$ and $0KL_{pc}$ peaks are threefold split.

Therefore, the unit-cell symmetry of the multi-domain films can be determined by analyzing the peak splitting pattern.

## Bibliography

[1] D. Vanderbilt and M. H. Cohen, "Monoclinic and triclinic phases in higher-order Devonshire theory," *Phys. Rev. B* **63**, 094108 (2001).

# APPENDIX E

# Preventing Overshoot in Weak Signal Regions of CTRs

The CTR intensity decreases exponentially as one moves away from the Bragg peak. If the crystal surface has a significant roughness profile, the intensity decreases faster and it becomes almost impossible to measure the CTR intensity in the midzone region far from the Bragg peaks.

Figure E.1 shows the measured (21L) rod from an uncoated ZnO O-polar $(000\overline{1})$ surface. Since the Bragg peaks at odd L values are missing due to a selection rule, the signal becomes very weak in those regions, and, as a result, there are missing datapoints in the dataset, which can be seen in the figure near L=1 and L=3. These missing datapoints can be problematic when fitting. In Figure E.1 (a), the fitting result (red line) fits very well in the region with measured datapoints. However, the simulated rod shows significant humps of intensity in the region with the missing datapoints. This is quite problematic because if the simulated humps were real, they should be measurable during the experiment. The missing datapoints in the rod, however, are due to the CTR intensity weaker than lowest measurable intensity ($\sim 10^{-2}$ in this dataset). The simulated intensity values in the missing data region should hence be lower than the lowest measured intensity in the dataset. In order to address this problem, we introduced a new FOM function, 'loglim', for the fitting. In Figure E.1 (b), green datapoints are filling the gap between the last measured datapoints (blue datapoints). These green points are from a linear interpolation between the lowest measured intensity points right before and after the gap, and they act as limit points for the simulated intensity. The loglim FOM is basically identical to the 'log' FOM [Equation (4.3)] in the way of calculation, but if the simulated

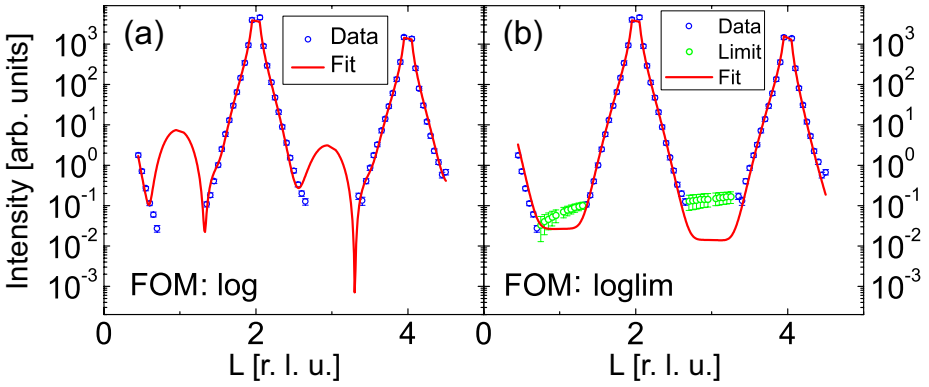


Figure E.1: Overshoot problem in CTR fitting. (a) Fitting with standard 'log' FOM results in intensity overshoot in the missing datapoint region. (b) Fitting with 'loglim' FOM successfully prevented the overshooting problem.

intensity is greater than the interpolated intensity in the gap, the difference is added to the FOM as an additional penalty:

$$P_i = \begin{cases} \log_{10} E_i^{\mathrm{sim}} - \log_{10} E_i^{\mathrm{int}}, & \text{if } E_i^{\mathrm{sim}} > E_i^{\mathrm{int}}, \\ 0, & \text{otherwise.} \end{cases}$$

$$\mathrm{loglim} = \frac{1}{N-1}\Big( \sum_i \big| \log_{10} E_i^{\mathrm{exp}} - \log_{10} E_i^{\mathrm{sim}} \big| + \sum_j P_j \Big).$$

Here, $E_i^{\mathrm{int}}$ denotes the interpolated intensities in the gap region between the lowest measured intensity points [green datapoints in Figure E.1 (b)]. By employing the loglim FOM function, the parameter space is modified such that those parameter sets where the simulated intensities violate the limit points have larger FOMs and cannot be the lowest solution. Figure E.1 (b) shows the fitting result using this new FOM function, and, as can be seen in the figure, the lowest FOM with no limit violations in the gap region is successfully found.